ADVERTIMENT. La consulta d'aquesta tesi queda condicionada a l'acceptació de les següents condicions d'ús: La difusió d'aquesta tesi per mitjà del servei TDX (www.tesisenxarxa.net) ha estat autoritzada pels titulars dels drets de propietat intel·lectual únicament per a usos privats emmarcats en activitats d'investigació i docència. No s'autoritza la seva reproducció amb finalitats de lucre ni la seva difusió i posada a disposició des d'un lloc aliè al servei TDX. No s'autoritza la presentació del seu contingut en una finestra o marc aliè a TDX (framing). Aquesta reserva de drets afecta tant al resum de presentació de la tesi com als seus continguts. En la utilització o cita de parts de la tesi és obligat indicar el nom de la persona autora.

ADVERTENCIA. La consulta de esta tesis queda condicionada a la aceptación de las siguientes condiciones de uso: La difusión de esta tesis por medio del servicio TDR (www.tesisenred.net) ha sido autorizada por los titulares de los derechos de propiedad intelectual únicamente para usos privados enmarcados en actividades de investigación y docencia. No se autoriza su reproducción con finalidades de lucro ni su difusión y puesta a disposición desde un sitio ajeno al servicio TDR. No se autoriza la presentación de su contenido en una ventana o marco ajeno a TDR (framing). Esta reserva de derechos afecta tanto al resumen de presentación de la tesis como a sus contenidos. En la utilización o cita de partes de la tesis es obligado indicar el nombre de la persona autora.

WARNING. On having consulted this thesis you're accepting the following use conditions: Spreading this thesis by the TDX (www.tesisenxarxa.net) service has been authorized by the titular of the intellectual property rights only for private uses placed in investigation and teaching activities. Reproduction with lucrative aims is not authorized neither its spreading and availability from a site foreign to the TDX service. Introducing its content in a window or frame foreign to the TDX service is not authorized (framing). This rights affect to the presentation summary of the thesis as well as to its contents. In the using or citation of parts of the thesis it's obliged to indicate the name of the author

Universitat Politècnica de Catalunya
Departament de Teoria del Senyal i Comunicacions
AntennaLab

Radiation Pattern Reconfigurable Microfabricated Planar Millimeter-wave Antennas

Tesi presentada per obtenir el títol de

Doctor per la Universitat Politècnica de Catalunya

Jordi Balcells i Ventura

Advisor: Lluís Jofre Roca

Barcelona, March 29, 2011

ACTA DE QUALIFICACIÓ DE LA TESI DOCTORAL

Reunit el tribunal integrat pels sota signants per jutjar la tesi doctoral:

Títol de la tesi: Radiation Pattern Reconfigurable Microfabricated Planar Millimeter-wave Antennas ....

Autor de la tesi: Jordi Balcells Ventura ....

Acorda atorgar la qualificació de:

☐ No apte
☐ Aprovat
☐ Notable
☐ Excel·lent
☐ Excel·lent Cum Laude

Barcelona, …………… de/d'…...............……………. de ....….

El President

....
(nom i cognoms)

El Secretari

....
(nom i cognoms)

El vocal

....
(nom i cognoms)

El vocal

....
(nom i cognoms)

El vocal

....
(nom i cognoms)

Abstract

The migration of telecommunication services and radar systems to Millimeter-wave (MMW) frequencies (30 to 300GHz) leads to the necessity of researching for alternative fabrication technologies and materials rather than the used for microwave frequencies. Part of this thesis work is focused in three MMW band applications such as Satellite Communication Systems (SCS) at Ka-band,Wireless Personal Area Network (WPAN) at V-band and Automotive Radar at W-band. In these applications, where the antenna is part of a mobile device, it is targeted the use of planar antennas because their low profile and low fabrication cost, together with reconfiguration capability and low losses.

This thesis presents an analysis of materials, transmission lines geometries and switches in the MMW frequency band. The fabrication tolerances have also been studied, analyzing the variations in the final antenna parameters. The tolerances, together with the materials and antenna dimensions lead to the use of microfabrication processes. Finally, two different pattern reconfigurable antenna designs operating at Ka-, V- and W-bands are presented as a demonstration.

Keywords: Millimeter-wave frequencies, microfabrication, reconfigurable antenna, circular polarization, beamsteering, fabrication tolerances, CPW Patch antenna, Qdime antenna, RF-MEMS switch.

Aknowledgments

Aquest treball s'ha dut a terme en part amb el suport de la *Comisión Interministerial de Ciencia y Tecnología* (CICYT) amb els projectes TEC2007-66698-C04-01/TCM i CONSOLIDER CSD2008-00068, per la beca FIR de l'*Agència de Gestió d'Ajuts Universitaris i de Recerca* (AGAUR) i pel projecte *Tri-band planar antennas for VSAT Satellite Applications* de l'empresa INDRA.

M'agradaria agrair a el Prof. Lluís Jofre la seva confiança, demostrada des que va comptar amb mi pel projecte Blocksat fins al dia d'avui, incloent-me en diferents projectes d'antenes així com del K2M. Gràcies per obrir la porta del teu despatx el dia en que et vaig venir a veure per primera vegada i gràcies per haver continuat guiant-me cap a nous objectius. Sense tot això, el meu futur professional seria d'un altre color. També voldria donar les gràcies a el Prof. Adolfo Comerón, qui va començar com el meu supervisor en el projecte Blocksat i ha acabat sent un bon amic. Sempre recordaré els nostres cafès de treball. Gràcies per tenir sempre un minut per escoltar-me i donar-me bons consells. També m'agradaria mencionar el suport del Prof. Broquetas en els temes referents a la beca i l'ajuda del Prof. Romeu que sempre m'ha donat nous punts de vista en les dificultats i que sempre ha tingut un moment per ajudar-me en el que fes falta. M'agradaria també fer un reconeixement al conjunt de professionals del departament, sobretot a en Rubén per la seva ajuda tècnica.

Tot seguit, voldria aprofitar per donar les gràcies als meus pares, en Manel i la Maite. Ells sempre han tingut un '*endavant que tu pots*' en tots els moments de la meva vida. Des de sempre m'han encoratjat a superar-me i a aconseguir els meus objectius. Hi ha tantes coses a agrair-vos que no sabria ni per on començar. Ho agruparé tot en un inmens *Gràcies*. Als meus germans, la Laia i l'Arnau, també els vull agrair la seva paciència i col·laboració durant aquest temps. Sou part del meu equilibri. Una menció especial als membres de la meva família i sobretot als meus avis amb qui sempre he tingut un lligam molt fort.

Si hi ha una persona que es mereix un gran reconeixement a la seva tasca en aquesta tesis es la Sanja, el meu amor. Ella ha aguantat tot l'estrès i ha sacrificat un munt de coses perquè jo aconseguís acabar. Sento totes les vegades que he dit '*això ja ho farem quan acabi la tesis*' ja que algunes segur que s'han quedat en l'oblit i algunes altres prometo que les realitzarem, com aprendre Serbi. Has estat el meu salvavides quan ha sigut necessari i has estat sempre al meu costat, animant-me a continuar en moments de fallida. Sóc molt afortunat de tenir tan bona companyia de viatge. Hvala puno!

La realització del treball aquí presentat no només dóna com a fruit aquest document, si no que m'ha donat la oportunitat de conèixer i treballar amb molta gent diversa. Entre ells, he tingut la sort de poder compartir un munt d'hores de despatx, laboratori, congressos, viatges i footing amb el meu gran amic Dani Rodrigo. Ell és una persona brillant que sempre ha tingut temps per ajudar-me i obrir-me els ulls a coses que se m'havien passat per alt. Crec que hem aconseguit realitzar un bon tàndem i n'estic orgullós. Espero retrobar-nos en el futur. Amb la Raquel Serrano he compartit un munt de vivencies durant aquest temps que ens han convertit en bons amics. Començant per les epopeies a l'hora de gestionar les beques fins a treballar plegats a Urbiotica. Gracias a ti no solo he aprendido que Teruel existe, si no que allí hay, almenos una, gente genial. M'agradaria poder seguir explicant les coses que m'ha aportat cada una de les persones amb les que m'he creuat durant aquest temps, però seria un no acabar. Viatges, dinars, partits de bàsquet i futbol, festes i sobretot hores al despatx i en el campus. Això si, m'agradaria mencionar-los a tots i agrair-los cada un dels passos que hem caminat junts i que caminarem. Gràcies a la gent de Blocksat, Nani i Hector. Gràcies als ja doctors Sandra, Gerard, Luca, Roberto, Hugo, Mariví, Pablo, Maria, Txema i Javi. Gràcies als que un dia sereu doctors, Pere, Santi, Gemma, Bea, Marta, Benji, Jordi A., Enrique, Marc Imbert, Juan Carlos, Oscar, Sergi, Maria, Adrián, Irena, Edgar i Edu. Gràcies a la gent d'Urbiotica, en Toni, la Irene, en Marc, en David, en Jordi M. i la Maribel.

I would like to use this place to acknowledge the support given by Prof. Cetiner, Dr. Unlu, Yasin Damgaci and Hema Swaroop from Utah State University. Without their help, the work here presented would not be possible. I am glad we came to CNF during the summer and getting to know all of you guys. Hope we will keep close. Thank you my friends.

Finalment, m'agradaria agrair el suport a tothom a qui d'alguna manera aquesta tesis ha tocat, ja sigui de forma directa o indirecta. En especial a tots els meus amics, que en ocasions m'han pres per una mica llunàtic, però amb "carinyo".

En conclusió, gràcies a tots i totes. Això només és el començament d'un nou camí. Espero retrobar-vos'hi de nou.

List of Symbols

AF Array Factor.

$A_{\mathbf{eff}}$ Antenna Effective Area.

B Antenna Bandwidth.

D_0 Error-free Antenna Directivity.

D_e Equivalent Circular Diameter.

D_r Receiver Antenna Directivity.

D_t Transmitter Antenna Directivity.

D_{lin} Linear Array Directivity.

D_{pla} Planar Array Directivity.

D Antenna Directivity.

E_b/N_0 Energy per bit to Noise power spectral density ratio.

E_{x0} Radiated Field x component.

E_{y0} Radiated Field y component.

F Noise Factor.

G_0 Error-free Antenna Gain.

G Antenna Gain.

N_{arr} Array Number of Elements.

N_m Monte Carlo Method Iterations Number.

P_N Noise Power.

P_r Received Power.

P_t Transmitted Power.

Q_t Quality Factor.

Q_{fil} Filling Factor.

R_c Series Resistance of the CPW Center Strip.

R_g Series Resistance of the CPW Ground Plane.

R_s Conductor Surface Resistance.

R_{ch} Channel Data Rate.

R Range.

S_{low} Qdime Lower Slot Length.

S_{pat} Qdime Arch Perimeter.

S_{upp} Qdime Upper Slot Length.

T_0 Standard Noise Temperature (290 K).

Ts Noise Temperature.

Y_{ant} Antenna Admittance.

Y_{cpw} CPW Admittance.

Y_{slt} Slot Admittance.

Z_0 Line Characteristic Impedance.

Z_L Loaded Impedance.

Z_g Source Impedance.

Z_{cpw} CPW Impedance.

$\Delta\phi_{plf}$ Antenna System Polarizations Angle Difference.

$\Delta\phi_{pol}$ Orthogonal-Fields Angle-Difference.

$\Delta\theta_{-3dB}$ Half-Power BandWidth.

Ω_e Solid Angle.

α_{con} Conductor or Ohmic Losses.

α_{die} Dielectric Losses.

α_{tot} Power Attenuation.

α Array Progressive Phase.

β Amplitude Phase.

η Intrinsic Impedance in vacuum.

λ_0 Wavelenght in vacuum.

λ_{eff} Effective Wavelenght.

λ_{low} Qdime Lower Wavelenght.

λ_s Wavelenght in the slot.

λ_{upp} Qdime Upper Wavelenght.

μ_0 Permeability in the vacum ($4\pi \times 10^{-7}$ Henry/meter).

ψ Array Electrical Phase.

ρ Conductor Resistivity.

σ_δ Amplitude Standard Deviation.

σ_ϕ Phase Standard Deviation.

σ_θ Beam Pointing Standard Deviation.

σ_{AR} Axial Ratio Standard Deviation.

σ_{rcs} Radar Cross Section.

σ Standard Deviation.

θ_{max} Maximum Radiation Direction.

ε_{eff} Dielectric Effective Permittivity.

ε_r Dielectric Relative Permittivity.

φ_{geo} Angle respect the axis in a geostationary satellit orbit direction.

$\vec{E}_0$ Single Element Radiation Pattern.

a_n n^{th} Element Current Feed.

a_{equ} Electrical Equivalent Radius.

c_0 Speed of Light in vacuum.

d_{elem} Array Elements Distance.

d_{feed} Qdime Feed Distance.

d_{slt} Slot Distance.

$e_{\beta n}$ Amplitude Phase Error.

f_{low} Qdime Lower Resonant Frequency.

f_{upp} Qdime Upper Resonant Frequency.

f Frequency.

g_{ap} CPW ground gap.

h_{die} Dielectric Thickness.

h_{low} Qdime Lower Substrate Thickness.

h_{rad} Qdime Radomo Substrate Thickness.

h_{upp} Qdime Upper Substrate Thickness.

k_0 Wave number in vacumm.

k_B Boltzmann Constant ($1.381 \cdot 10^{-23}$ J/K).

k_{die} Wave number in dielectric.

l_{MEM} RF-MEMS switch cantilever length.

l_{cpw} CPW Length.

l_{cut} Patch Perturbation Length.

l_{gap} Patch-Parasit Triangles Distance.

l_{low} Qdime Lower Patch Shorting Wall Distance.

l_{pat} Patch Length.

l_{sli} Qdime Etched Slit Length.

l_{slt} Slot Length.

l_{upp} Qdime Upper Patch Shorting Wall Distance.

r Distance between Transmitter and Receiver.

$tan\delta$ Loss Tangent.

w Angular Frequency.

$\mathbf{t}_{str}$ Strip Thickness.

$\mathbf{w}_{bri}$ Air-bridge width.

$\mathbf{w}_{low}$ Qdime Lower Short Wall Width.

$\mathbf{w}_{MEM}$ RF-MEMS switch cantilever width.

$\mathbf{w}_{slt}$ Slot Width.

$\mathbf{w}_{str}$ Strip Width.

$\mathbf{w}_{upp}$ Qdime Upper Short Wall Width.

Acronyms

ACC	Adaptive Cruise Control
ADS	Advanced Design System
AF	Array Factor
AR	Axial Ratio
AP	Access Point
AUT	Antenna Under Test
BCB	Benzocyclobuten polymer
BER	Bit Error Rate
CP	Circular Polarization
CPW	CoPlanar Waveguide
DC	Direct Current
EHF	Extremely High Frequency
GCPW	Grounded-CoPlanar Waveguide
HLP	Horizontal Linear Polarization
HF	Hydrofluoric Acid
HW	Hard-Wire
HPBW	Half-Power Beamwidth
ITU	International Telecommunication Union
LHCP	Left-Handed Circular Polarization
LOS	Line-of-sight
LP	Linear Polarization

LRR	Long Range Radar
LTCC	Low Temperature Co-fired Ceramic
MCS	Modulation and Coding Sets
MMW	Millimeter-wave
NLOS	Non-line-of-sight
PLF	Polarization Loss Factor
PTFE	Polytetrafluoroethylene or Teflon
RF	Radio Frequency
RF-MEMS	Radio-Frequency Microelectromechanical Systems
RHCP	Right-Handed Circular Polarization
SCS	Satellite Communication Systems
SEM	Scanning Electron Microscope
SLL	Sidelobe Level
SNR	Signal-to-Noise Ratio
SRR	Short Range Radar
TE	Transverse electric
TEM	Transverse electromagnetic
TM	Transverse magnetic
VLP	Vertical Linear Polarization
VSAT	Very Small Aperture Terminal
WPAN	Wireless Personal Area Network

List of Figures

List of Tables

Contents

Als meus pares, Manel i Maite,
als meus germans, Laia i Arnau,
i a la Sanja, mojoj voljenoj Sanji.

Ara és demà.
No escalfa el foc d'ahir ni el foc d'avui,
i haurem de fer foc nou.
Del gran silenci ençà, tot el que es mou
es mou amb voluntat d'esdevenir.
I esdevindrà.
Miquel Martí i Pol, 1977

Chapter 1

Introduction

Telecommunication services and radar systems are migrating to Millimeter-wave (MMW) frequencies, where wider bandwidths are available. Such migration requires the use of different technologies with the capability to operate at the MMW frequency band (30 to 300GHz), and more specifically at Ka- (26.5 to 40GHz), V- (50 to 75GHz) and W-band (75 to 110GHz). For many applications and more concretely those where the antenna is part of a mobile device, it is targeted the use of planar antennas for their low profile and low fabrication cost. A wide variety of requirements is translated into a reconfiguration capability and low losses within each application frequency bandwidth. To deal with the mentioned challenges, the MMW antenna dimensions, together with the materials, fabrication tolerances and reconfigurability capability lead to microfabrication processes.

The aim of this thesis is the analysis of the mentioned concepts, materials, transmission lines geometries and switches in the MMW frequencies context and their final application in antenna designs compatible with microfabrication. Finally, specific designs operating at Ka-, V- and W-band will be presented as a demonstration.

In Chapter 2, Millimeter-wave (MMW) printed planar antennas are reviewed. The current state-of-the-art of planar antenna architectures is being summarized, emphasizing the inconveniences derived from the fabrication tolerances at MMW frequencies. This chapter also includes a summary of the different antenna reconfigurabilities. Finally, the three applications under study in this thesis are introduced: Satellite Communication Systems (SCS), Wireless Personal Area Network (WPAN) and Automotive Radar.

In Chapter 3, some MMW circuit technologies are analyzed. The four most used materials at MMW frequencies (Polytetrafluoroethylene or Teflon (PTFE), Quartz, Benzocyclobuten polymer (BCB) and Low Temperature Co-fired Ceramic (LTCC)) have been presented and compared in terms of permittivity (ε_r) and loss tangent ($tan\delta$). An study of the main transmission lines attenuation (microstrip, stripline and CPW) at high frequencies is included. Finally, an overview of the RF-MEMS switches is presented in comparison with PIN diodes and FETS switches.

Chapter 4 presents two different polarization-reconfigurable base-elements designs: CPW Patch antenna and 4-Qdime antenna. The first consists of a single reconfigurable element with integrated RF-MEMS switches, designed to operate at Ka- and V-band. The second antenna presented in this thesis has a composed architecture where the polarization reconfigurability is obtained by switching the phase feeding for each of the four linear polarized elements in the feed network with RF-MEMS. The 4-Qdime antenna has been designed to operate at V- and W-band. Finally, both antenna designs are compared.

Chapter 5 focuses in polarization and beam pointing reconfigurable antenna array designs, using as base element the polarization-reconfigurable antennas presented in the previous chapter. Using phased array techniques, beamsteering is computed and implemented with 1-bit discrete phase-shifter. This chapter includes comparison of both antenna arrays.

Chapter 6 includes a fabrication tolerances study of antenna arrays for different number of elements. The gain loss, beam pointing error, Half-Power Beamwidth (HPBW) error and sidelobe level error are being estimated as a function of the amplitude and phase errors presented at each elements array. A study of the axial ratio error due to amplitude and phase errors of the radiated field orthogonal components is then presented. The fabrication tolerances obtained have been applied to the previous designed antennas, concluding the necessity to use microfabrication to manufacture them. The second part of this chapter summarizes the different microfabrication processes.

In Chapter 7, the microfabrication process for the designed antennas is presented in detail. Polarization- and pointing- reconfigurable CPW Patch antennas operating at Ka- and V- band have been fabricated in a clean-room facility. The isolation and time measurement characterization measurements for two different RF-MEMS switches is presented. The reflection coefficient and the axial ratio of the antenna configured in Linear Polarization (LP) and Circular Polarization (CP) at Ka- and V-band have been measured using different set-ups and its parameters are discussed.

Finally, Chapter 8 concludes the study and gives some suggestions for further research.

Chapter 2

Millimeter-wave Planar Antenna. Architecture and Applications

Planar antennas are characterized by their flat appearance and low profile. The use of planar antennas has increased in many professional and commercial applications, where characteristics such as reduced dimensions, conformability, light weight, low-cost and easy fabrication are targeted [2]. Their planar nature makes them ideal for large arrays and simplifies the interaction with additional microwave circuit components such as printed lines [3]. Antennas capable of radiation pattern reconfigurability are very attractive for wireless communication applications in order to overcome multipath fading problems or pointing and roll maladjustments, and therefore enhance the system performance. The Millimeter-wave (MMW) band, also called Extremely High Frequency (EHF) band, runs in the range of frequencies from 30 to 300 GHz, which is translated to a wavelength in vacuum (λ_0) from 10 to 1 millimeter.

This chapter explains briefly the architecture of printed planar antennas, paying special attention to the fabrication tolerances at MMW frequencies. Different types of antenna reconfigurability are also summarized. Finally, three applications at MMW frequencies such as Satellite Communication Systems (SCS), Wireless Personal Area Network (WPAN) and Automotive Radar are introduced.

2.1 Architecture

A planar antenna consists of a radiating element on a dielectric substrate, with printed and slot antennas as the most common types used. Depending on the feed network technique, which may or may not be at the same level as the radiating element, the antenna will have a single- or multi-layer structure. A single layer structure is characterized for having the radiating element and the feed network printed on the same substrate, as shown in the example in Fig. 2.1(a).This solution results to be the simplest fabrication process, but the dielectric substrate has to be chosen as a compromise between the radiating element and the feed network requirements. In the multi layer architecture the radiating element is placed on a certain dielectric substrate while the feed network is placed on a second substrate below. In this case, there is a dielectric substrate adequate for the radiation requirements and there is another dielectric substrate adequate for the feed network and its requirements. Fig. 2.1(b) shows an example where the antenna is fed by aperture-coupling through a slot in the ground plane.

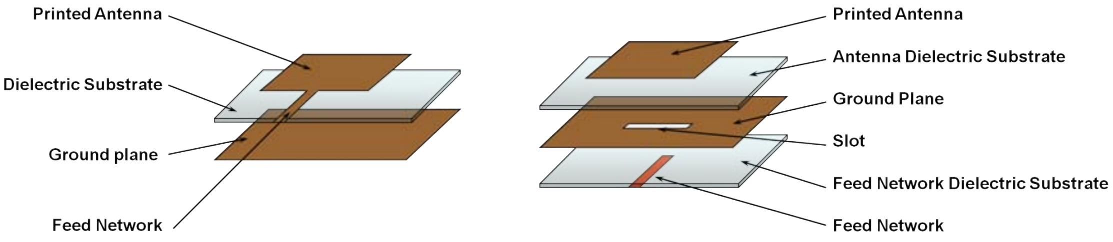

(a) Single Layer (b) Multi Layer

Figure 2.1: Planar Antenna Architectures

The design process of a planar antenna may be divided in three main parts: radiating element, array geometry and feed network. The radiating element design is related to some final antenna electrical characteristics such as the radiation pattern, frequency bandwidth and field polarization. More directive and higher gain antenna are obtained when using array antennas. They are characterized by the inter elements distance, and the amplitude and phase of each radiating element feeding current. The array parameters are also related to the radiation pointing direction or tilt. Beside the single element character, the antenna polarization, is also affected by the array characteristics in those cases where the technique to rotate sequentially the radiating element is applied in order to improve the circular polarization [4]. Finally, the feed network technology is related to the gain, efficiency and bandwidth, that are determined by each application [5,6]. Typical technologies used in planar antennas for the feed network are waveguide and printed transmission lines.

Microstrip patches and slot antennas dimensions are normally $\lambda_0/2$ and in some cases $\lambda_0/4$. Fig. 2.2(a) shows that the antenna dimensions at Millimeter-wave band lower than $5mm$. These reduced dimensions lead to take into consideration the fabrication tolerances at such high frequencies. The acceptable tolerances of an antenna may vary from $\lambda_0/50$ to $\lambda_0/200$, and among them the tolerances of $\lambda_0/100$ are the most commonly used. Fig. 2.2(b) illustrates how the fabrication tolerances at MMW frequencies are below $100\mu m$, and in some cases lower than $10\mu m$. These low tolerances imply the search for alternative fabrication processes to substitute the commonly used for microwaves antennas. Techniques such as *Microfabrication* may guarantee the required tolerances together with the possibility to integrate the antenna with other elements of the communication system, such as Radio-Frequency Microelectromechanical Systems (RF-MEMS) devices.

2.2 Antenna Reconfigurability

The attractiveness of using reconfigurable antennas lies in their ability to adapt autonomously to environmental changes or operational requirements. The reconfiguration is achieved by changing the antenna structure and therefore redistributing the currents, resulting in changes in the antenna

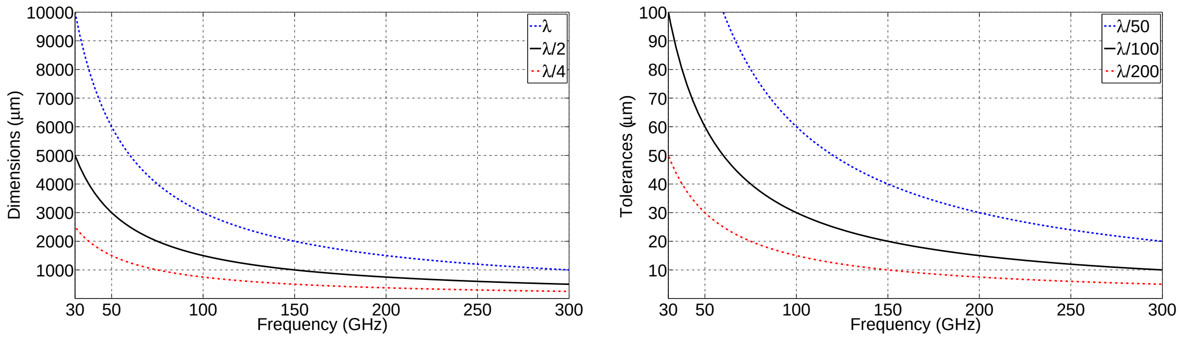

(a) Antenna dimensions

(b) Fabrication tolerances

Figure 2.2: MMW antennas typical dimensions and fabrication tolerances

impedance and/or radiation properties [7]. The most common antenna parameters reconfiguration [8–10] are:

- **Resonant Frequency**. A change in the antenna resonant frequency allows a single device to work in numerous wireless systems operating over a wide frequency range and demanding different operating electrical characteristics (Fig. 2.3(a)).
- **Radiation Pattern**. The radiation pattern may be changed in direction, gain or beamwidth depending of the system requirements (Fig. 2.3(b)).
- **Polarization**. An antenna with polarization reconfigurability may switch from linear to circular polarization reducing polarization mismatch in scenarios where the antenna orientation is not fixed.

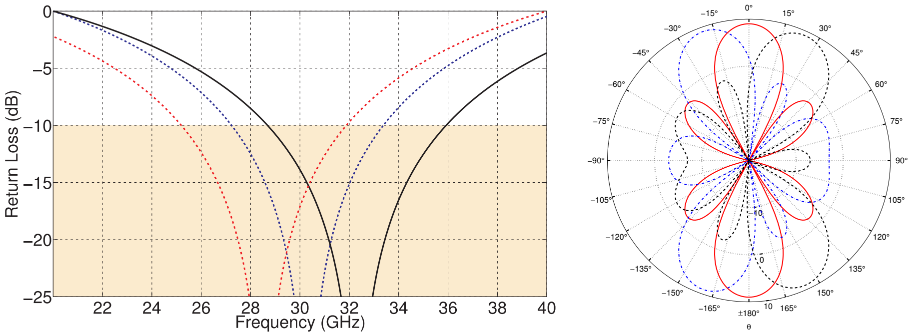

(a) Resonant Frequency

(b) Radiation Pattern

Figure 2.3: Antenna Reconfigurable Parameters

The reconfigurability may be done by using different techniques [11] such as capacitive loading [12], material tuning [13], mechanical structural changes [14] or the use of switches (RF-MEMS, PIN Diodes and FET) [15]. The different types of reconfigurability presented in this thesis are done by the use of RF switches, more concretely by Radio-Frequency Microelectromechanical Systems (RF-MEMS) switches [16]. The recent development of RF-MEMS switches makes them attractive to be used at MMW frequencies because of their small dimensions ($\backsim 100\mu m$), low parasitic capacitance and insertion loss, high isolation and fast switching speed ($\backsim 1\mu s$) [17]. To achieve the appropriate autonomous reconfigurability, the antenna system may include an optimization genetic algorithm capable of selecting the optimal switch status configuration at any instant [18].

In antenna arrays, the capability to change the direction where the antenna is pointing, focusing the energy toward a specific direction is called beamsteering. This beamsteering may be accomplished in different ways [19]: analog, digital, optical or with reflectarrays. Beamsteering is not considered by some authors as a reconfigurability capability of the antenna because the currents on the radiating elements are not redistributed. In this thesis, for those cases where the phase-shifter is integrated into the feed network (for example in a printed transmission line) becoming part of the antenna array itself, the array antenna will be considerate reconfigurable in radiation pattern.

2.3 Applications

Many applications such as radio astronomy, remote sensing, wireless communication systems, millimeter-wave scanner and high resolution radar use MMW frequencies. The work presented in this thesis is focused in wireless communication systems such as *Satellite Communication Systems (SCS)* at Ka-band (26.5 to 40 GHz) and *Wireless Personal Area Network (WPAN) Systems* at V-band (50 to 75 GHz), that are very attractive due to their high transmission rates (see Figure 2.4). Another Millimeter-wave application that has been considered is the *Long Range Automotive Radar* at W-band (75 to 110 GHz).

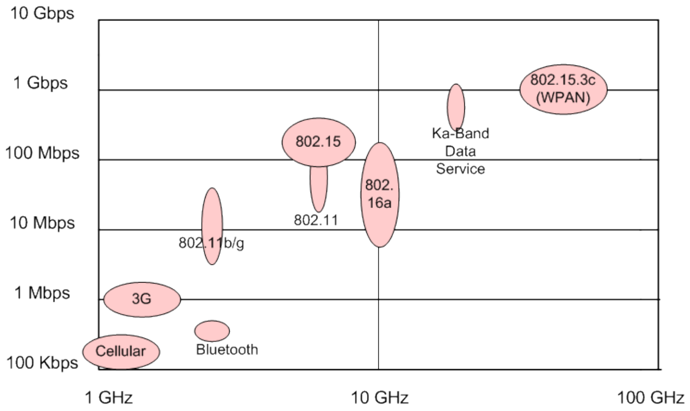

Figure 2.4: Wireless Communication Systems frequency and data rates

2.3.1 Satellite Communication Systems (SCS) at Ka-band

Satellite Communication Systems provide broadband services as a complement to the terrestrial networks, offering its inherent global coverage capacity and a quick deployment. These characteristics offer solutions in different fields, such as:

- Internet access to low terrestrial coverage zones

- Unidirectional television broadcast
- Intercontinental long distance telephony
- Mobile communications for ships, vehicles or airplanes
- Bidirectional communication services with high transmission rate and high security for emergencies groups such as fire departments, police, etc.

Historically, Satellite Communication Systems (SCS) have used the parabolic reflector as radiating element because of its high gain, efficiency and simplicity to generate linear and circular polarization. With the appearance of Very Small Aperture Terminal (VSAT) systems at the beginning of the 80's, the physical dimensions of the antennas were reduced even when they kept being bulky and difficult to carry. In order to provide SCS higher mobility, it is necessary to substitute the actual antennas by planar radiating structures which can be easily integrated to any mobile platform, from a vehicle or train to the fuselage of an airplane [20]. The increasing demand of transmission capacity in VSAT communication systems is one of the main reasons for the migration to higher frequencies such as Ka-band (30/20GHz) [21]. Problems of using planar antennas at these frequencies come from the actual technologies performances and the difficulty to obtain a radiating element with the proper bandwidth and polarization.

Satellite Communication Systems require high gain antennas in order to have a good SNR level in long distance links. Such a high gain is related to narrower beam and low sidelobes radiation pattern which are translated to an improvement of the angular utilization. Also, an improvement of the spectral utilization is achieved through frequency reuse. Circular Polarization (CP) is used to avoid roll maladjustments when the two antennas are pointed to each other; while systems with Linear Polarization (LP) require an accurate mechanical orientation of the antenna. The capability of polarization reconfigurability allows the antenna to be used in all communication systems. Beam steering properties provide the reconfiguration required to point the system antennas without the necessity of moving mechanical parts [22].

The International Telecommunication Union (ITU) makes recommendations in its ITU-R S.580-6 [23] for the radiation pattern of antennas of earth stations operating with geostationary satellites. The antenna has to fulfill the gain (G) requirement,

$$G \leq 29 - 25 \log \varphi_{geo} \qquad dBi \tag{2.1}$$

where φ_{geo} is the angle with respect to the axis pointing in the geostationary satellite orbit direction.

The coverage zone includes from 1° (or $100\lambda_0/D_e$, taking the larger of both) to 20° in the equatorial plane direction; and between -3° and 3° in the orthogonal direction (Figure 2.5). λ_0 stands for the operating wavelength and D_e for the antenna equivalent circular diameter. D_e is computed from the antenna aperture area (A_{eff}) as

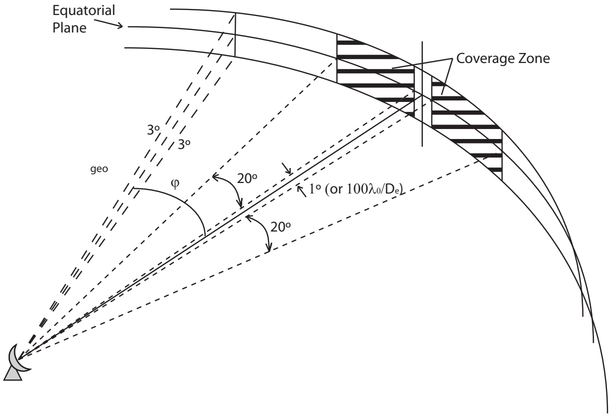

Figure 2.5: ITU-R S.580-6 recommended coverage zone

$$D_e = \sqrt{4A_{\text{eff}}/\pi} \tag{2.2}$$

As an example, for an antenna operating at 30 GHz with a desired gain of 41 dB, the coverage zone is delimited by $1.80^{\text{o}} \leq \varphi_{geo} \leq 20^{\text{o}}$ where the permitted gain is delimited by the radiation pattern shown in 2.6.

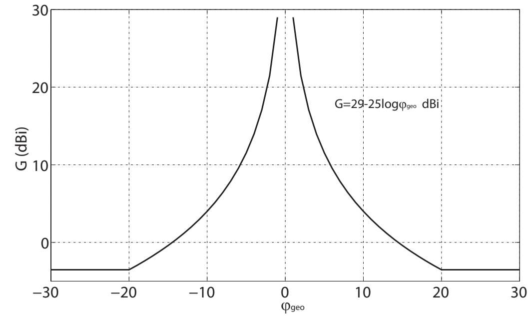

Figure 2.6: Delimiting radiation pattern for a 30GHz antenna with 41dB Gain

2.3.2 Wireless Personal Area Network Systems at V-band

Numerous applications are appearing for 60 GHz radio systems, classified mainly in video streaming, file transfer, and wireless Gigabit Ethernet. Parameters such as in-/outside use, distance between receiver and transmitter, Line-of-sight (LOS)/Non-line-of-sight (NLOS), position, or mobility are considered for each application. [24, 25]

IEEE 802.15.3c international standard [26, 27] provides regulations for Wireless Personal Area Network (WPAN) systems operating around 60 GHz. These systems are characterized by:

- Short-range data networks ($< 10m$)
- 7 GHz bandwidth ($\backsim 11.5\%$)
- Data rate between 2 Gbps and 3 Gbps.

- Frequency Band between 57 GHz and 66 GHz, depending on the region (Figure 2.7)

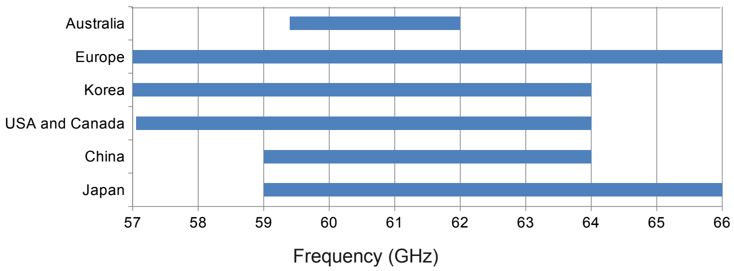

Figure 2.7: WPAN assigned spectra for different regions [1]

Because the high path loss at V-band frequencies, WPANs should employ high-gain antennas to improve the Signal-to-Noise Ratio (SNR). In addition, the use of directive antennas reduces multipath contributions by limiting the angles from which radiation is emitted and captured. The small wavelength of the signals at the 60 GHz band makes the communication more appropriate through Line-of-sight (LOS) path and first order reflections. In order to establish a reliable communication link, steerable beam antennas should be used. The polarization of the antenna also influences the link. The unknown orientation of the terminals makes antennas with polarization diversity attractive since they allow the link to operate independently to the antenna orientation, improving the performance of the system. In antenna arrays, polarization diversity may be achieved by using individual elements with polarization reconfigurability. All these characteristics lead to consider phased array antennas with polarization reconfigurable radiating element as the most appropriate radiating devices.

For the last several years, patch antennas [28], quarter-wave patch antennas [29], Yagi-Uda antennas [30], loop antennas or slot antennas [31], have been proposed as possible WPANs antennas. CoPlanar Waveguide (CPW) is the most common feed technology used at this band because its wide bandwidth and reduced losses.

As an example, a 60GHz operating frequency scenario where the devices are separated by a maximum distance (r) of 10 meters and the maximum power transmitted (P_t is 10 mW has been considered (Fig. 2.8). The Bit Error Rate (BER) has been set to 10^{-6}, the system data rate (R_{ch}) to 1Gbps, the frequency bandwidth (B) to 2GHz and the noise factor (F) to 7 dB.

The channel Signal-to-Noise Ratio (SNR) relates the received power (P_r) with the energy per bit to noise power spectral density ratio (E_b/N_0) as

$$SNR = \frac{P_r}{P_N} = \frac{E_b}{N_o}\frac{R_{ch}}{B} \tag{2.3}$$

where

$$\begin{aligned} P_r &= P_t\left(\tfrac{\lambda_0}{4\pi r}\right)^2 D_t D_r \\ P_N &= k_B T s B = k_B T_0\left(F-1\right)B \end{aligned} \tag{2.4}$$

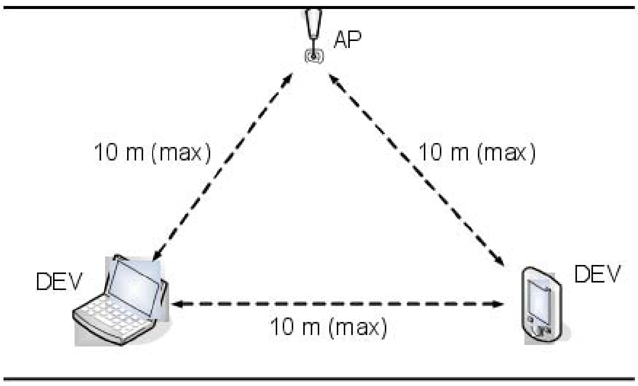

Figure 2.8: WPAN scenario under study

The BER depends on the E_b/N_0 and on the Modulation and Coding Sets (MCS) used. Fig. 2.9 shows the BER for the most used MCS: BPSK, QPSK, 8-PSK, 16-PSK and 16-QAM.

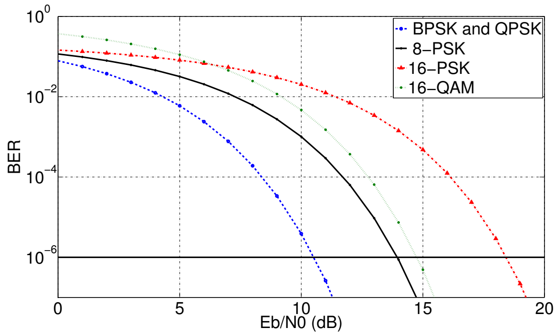

MCS	BER
BPSK QPSK	$\frac{1}{2}erfc\left(\sqrt{\frac{E_b}{N_0}}\right)$
8-PSK 16-PSK	$\frac{1}{k}erfc\left(\sqrt{\frac{kE_b}{N_0}}sin\left(\frac{\pi}{M}\right)\right)$
16-QAM	$\frac{3}{2k}erfc\left(\sqrt{\frac{kE_b}{10N_0}}\right)$

Figure 2.9: BER against E_b/N_0 for different MCS

Then, the required channel gain (D_tD_r) can be computed for the five MCS, as summarized in Table 2.1.

MCS	E_b/N_0 (dB)	SNR (dB)	D_tD_r (dB)
BPSK	10.5 dB	7.5 dB	10.6 dB
QPSK	10.5 dB	7.5 dB	10.6 dB
8-PSK	14.0 dB	11.0 dB	14.0 dB
16-PSK	15.0 dB	7.5 dB	15.0 dB
16-QAM	18.5 dB	12.0 dB	18.5 dB

Table 2.1: Channel gain (D_tD_r) for each of the MCS to obtain a BER of 10^{-6}

In order to estimate the antenna dimensions, the antenna directivity (D) is related to the effective area (A_{eff}) and the wavelength (λ_0) as

$$D = A_{\text{eff}}\frac{4\pi}{\lambda_0^2} \tag{2.5}$$

For array antennas, the estimated antenna directivity is computed differently if the array is linear or planar [32]. Directivity approximations for an N_{arr} omnidirectional linear and planar arrays are:

$$D_{lin} = 2\frac{d_{elem}}{\lambda_0} N_{arr} \qquad\qquad D_{pla} = 4\pi \frac{{d_{elem}}^2}{\lambda_0^2} (\sqrt{N_{arr}} - 1)^2 \tag{2.6}$$

Table 2.2 illustrates the required antenna effective area (A_{eff}) for the different channel gains. Two different cases have been studied. The first case consist of two devices with the same antenna directivity pointing to each other ($D_r = D_t$). The second case consist of having an AP with an omnidirectional antenna such as a Half-wavelength Dipole as a receiver ($D_r = 2.1dB$). The effective area is given as a function of λ_0. The table also illustrates the minimum array number of elements that would be required to obtain the desired antenna directivity in case that the radiating elements would be omnidirectional. The number of elements have been calculated for a linear and square planar array with an element distance of $\lambda_0/2$.

				Array Elements (d_{elem}=$\lambda_0/2$)	
	$D_t D_r$	D_t	A_{eff}	Linear	Planar
$D_r = D_t$	10.6 dB	5.3 dB	$0.27\lambda_0^2$	4×1	2×2
	14.0 dB	7.0 dB	$0.40\lambda_0^2$	5×1	3×3
	15.0 dB	7.5 dB	$0.45\lambda_0^2$	6×1	3×3
	18.5 dB	9.3 dB	$0.67\lambda_0^2$	9×1	3×3
$D_r = 2.1dB$	10.6 dB	8.5 dB	$0.55\lambda_0^2$	7×1	3×3
	14.0 dB	11.9 dB	$1.25\lambda_0^2$	16×1	4×4
	15.0 dB	12.9 dB	$1.57\lambda_0^2$	20×1	4×4
	18.5 dB	16.4 dB	$3.52\lambda_0^2$	44×1	5×5

Table 2.2: Effective area and linear and planar array dimensions for different channel gains and receiving antenna characteristics

2.3.3 Automotive Radar at W-band

Because the high number of injured people at road accidents worldwide, automotive active safety systems have been implemented as a further step for passive safety systems (air-bags, seat belts, etc.) with the objective of avoiding collisions between motor vehicles. Technologies in vehicular surround sensing such as automotive radar, lidar, ultrasonics and video cameras compete among them but also may be complementary. The advantage for automotive radar is its weather independence and a direct acquisition of distance and velocity without the necessity of post processing. There is also an stylistic advantage which relays in the possibility to be mounted behind a plastic bumper or radome making it invisible to human eyes.

The main task of an automotive radar is to detect objects (vehicles and obstacles) and measure

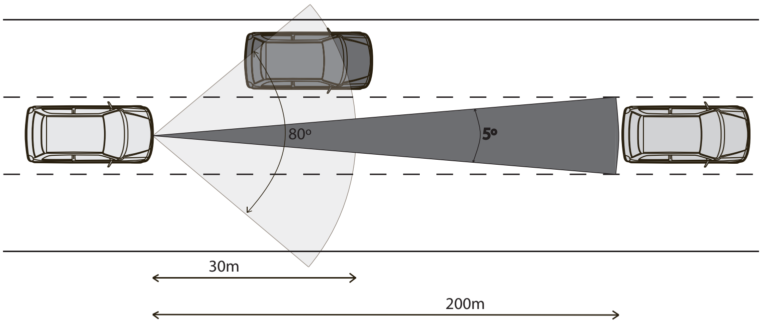

Figure 2.10: Automotive Radar: Long Range Radar and Short Range Radar

their position and velocity relative to the radar-equipped vehicle. To do this, the system transmits electromagnetic waves that are reflected by the objects in front of the vehicle. By analyzing the amplitude and phase of the echo signal received, the desired data is obtained. The relative speed of objects respect the host vehicle is obtained by Doppler Effect (shift in frequency between the transmitted and reflected signals) and the distance to the object is determined by the time lag.

$$P_{r_{min}} = \frac{P_t A_{\text{eff}}^2 \sigma_{rcs}}{(4\pi)^2 R_{max}^4 \lambda_0^2} \Longrightarrow R_{max} = \sqrt[4]{\frac{P_t A_{\text{eff}}^2 \sigma_{rcs}}{(4\pi)^2 P_{r_{min}} \lambda_0^2}} \tag{2.7}$$

Considering the radar equation 2.7, it can be seen that the maximum range R_{max} is proportional to the square root of A_{eff} and λ_0. σ_{rcs} denotes the target cross section of the target, P_t the transmitted power and $P_{r_{min}}$ the minimum received power necessary for detection. If a long range of the radar is desired, the antenna system will must have a high directivity and low sidelobes to avoid interferences.

Two types of automotive radar are found: Long Range Radar (LRR) and Short Range Radar (SRR). The combination of both of them give valuable data for the advance driver assistance systems (Fig. 2.10).

Type	Long Range Radar	Short Range Radar
Frequency	76.5 GHz	79GHz
Bandwidth	1 GHz	4 GHz
Maximum field of view	± 5º	± 80º
Range	200 m	30 m
Range Accuracy	± 10 cm	± 5 cm
Bearing Accuracy	± 1º	± 5º
Antenna Gain	20 dBi	13dBi
Antenna sidelobes level	20 dB	20dB

Table 2.3: Automotive Radar Requirements

- Long Range Radar (LRR) operating at 76-77 GHz. Main part of the Adaptive Cruise Control

(ACC) system which is used to control the vehicle distance and speed by monitoring the scenario several meters away in front and by predicting in advance the possible events, prevent the vehicle from a hazard situation in advance. Other applications may provide emergency braking assistance in critical situations

- Short Range Radar (SRR) operating at 24 GHz are migrating to 79 GHz. They monitor the imminent collisions and prepare the vehicle to minimize the effects of the accident by applying brakes with the appropriate force, activating the seat belt tensioners, adapting the seat orientation or closing the sunroof.

Table 2.3 summarizes the system requirements for the Long Range Radar and Short Range Radar. Long Range Radar has a visibility range of 200 meters and is typically activated at speeds of 30 Km/h to 180 Km/h or 200 Km/h. Long Range Radar system requires a narrow beamwidth, high gain antenna and beamsteering capability with a high bearing accuracy. Short Range Radar sensors do not measure the relative angle of the reflected objects having a broad lateral coverage (around 80^o) to monitor the immediate area of 30 meters in front of the vehicle.

Chapter 3

Millimeter-wave Circuit Technologies

Planar antennas are typically manufactured by waveguide or printed circuits technologies. Waveguide antennas are characterized for being heavy and bulky compared to printed antennas, which are more manipulable, compact, adaptable and conformable. Focusing into the fabrication process, printed antennas are normally more simple in structure and easier to fabricate by lithography techniques, becoming less expensive. Lithography techniques also provide good fabrication tolerances, in the order of tenths of micrometers, strongly required for MMW antennas.

The use of printed lines as feed networks instead of waveguides, provides the possibility to integrate the antenna with active and passive microwave components such as couplers, filters, power dividers, switches, etc. The possibility to have monolithic devices fabricated together with the radiating elements using printed circuit technology greatly reduces the final cost and increases the amount of possibilities, having the same cost for one or for one thousand components. One of the most attractive possibilities relays on the reconfigurability capacity when using RF-switches. Problems appearing by the use of printed feed networks are focused in the low efficiency of the feeding network [5]. In large antenna arrays, as the one needed to obtain a high directivity gain, feed line losses at millimeter-wave frequencies can be significative depending on the printed line type being used [33].

Printed circuit technologies also allow an easy use of multilayer structures. This type of structures give the possibility to have the feed network in a different level than the radiating elements or to have different radiating elements, one above the other. Those techniques are being used to increase efficiency, frequency bandwidth, or reconfigurability capability. Another advantage of using multilayer structures is the capability to change the antenna characteristics just by changing a single layer. For example, an antenna with linear polarization could be changed to circular polarization just by changing the radiating elements layer. This solution could be useful when no active devices are present in the antenna and different polarizations are desired.

The work presented in this chapter is focused on the study of different MMW technologies. Different dielectric substrates (BCB, LTCC, PTFE and Quartz) typically used in MMW applications are being evaluated. Concerning transmission lines at MMW, the attenuation for microstrip line, stripline and CPW have been studied. Focusing on the reconfigurability capability, a comparison of RF-MEMS with PIN diodes and FETs switches is presented.

3.1 Dielectric Substrates

Printed antennas and transmission lines can be defined as metallic shapes and traces etched from a metallic sheet (typically copper or gold) deposited onto an electrical insulator called dielectric substrate. This dielectric material is characterized by its dielectric constant (ε_r) and loss tangent ($tan\delta$) which are related to the material electromagnetic response. They are defined as:

- dielectric constant or relative permittivity (ε_r): quantifies the extent to which the dielectric concentrates electrostatic lines of flux.
- loss tangent ($tan\delta$): quantifies the dielectric's inherent dissipation of electromagnetic energy.

The effective dielectric constant (ε_{eff}) of an RF structure can be interpreted as the dielectric constant of a homogeneous medium, replacing the dielectric and air regions. The dielectric relative permittivity (ε_r) contributes with a different grade to the ε_{eff} depending on which type of structure is being used. In general, an increase of ε_r is translated into an increase of ε_{eff} which means a decrease in the effective wavelength (λ_{eff}) in the structure. This reduction of λ_{eff} results normally into a reduction of the printed device dimensions, because their proportionality.

Focusing in antennas, reducing dimensions is translated into increasing the quality factor (Q_t) and therefore reducing the antenna bandwidth (Equation 3.1) due to their inversely proportionality. The quality factor (Q_t) of an antenna is defined as the quotient between the power stored in the reactive field and the radiated power. The quality factor is representative of the antenna losses, being influenced by radiation, ohmic, dielectric and surface wave losses [34]. Then, $tan\delta$ of the dielectric contributes to the energy loss or attenuation in the transmission lines and also into the antenna Q_t and consequently to the bandwidth and efficiency.

$$Q_t = \frac{f_0}{\Delta f} \tag{3.1}$$

The choice of one or other dielectric substrate depends on the final requirements and fabrication tolerances. Parameters such as efficiency, bandwidth, gain, feed network attenuation or elements dimensions have to be considered. In [35] it is demonstrated that for an optimum printed antenna performance, the substrate thickness should not be thicker than about quarter wavelength in the substrate and that to achieve a good efficiency, the substrate relative permittivity should be less than $\varepsilon_r \lesssim 4.5$. For that reason, materials such as GaAs or Silicon which are typically used in electronics, are not used in antenna fabrication [33]. To guarantee a good performance as dielectric substrate, the material should have the relative permittivity and dielectric loss stable within the operating frequency range but also the thermal stability of these parameters is relevant.

At millimeter-wave frequencies not all the materials are characterized by their manufacturers in all the frequencies bands and some of the parameters will need to be extrapolated or tested. Table

Type	Dielectric Constant (ε_r)	Dissipation Factor ($\tan\delta$)
PTFE-type	2.195	0.0009 (@ 50 GHz)
Quartz	3.9	0.0007 (@ 60 GHz)
BCB (Benzocyclobutene)	2.52	0.002 (@ 100 GHz)
Low loss Epoxy	3.6	0.008 (@ 10 GHz)
GaAs	13.1	0.0016 (@10 GHz)
Silicon	12	0.015 (@10 GHz)
Alumina	9.6	0.001 (@ 10 GHz)
LTCC	6.0	0.002 (@ 95 GHz)
Polymide	3.5	0.008 (@ 10 GHz)

Table 3.1: Millimeter-wave dielectric substrates permittivity (ε_r) and tangent loss (tan δ)

3.1 summarizes the more significant materials and characteristics that are currently being used for millimeter-wave applications. Substrates like BCB, LTCC, Teflon (PTFE) based materials or Quartz are the most commonly used at millimeter-wave frequencies depending on the application requirements [28, 36–40].

Benzocyclobuten polymer (BCB) [41] is an organic material with stable permittivity value and low losses over the millimeter-wave frequency range. The dielectric constant is ϵ_r=2.65 with a few percent variations and the loss tangent is of values between 0.0008 and 0.002 within the frequency interval from 10 GHz to 100 GHz.

Low Temperature Co-fired Ceramic (LTCC) [42] is a multi-layer technology where a ceramic substrate is co-fired with low resistance metal conductors, such as Ag, Au or Cu, at low firing temperatures (less than 1000°C). LTCC also features the ability to embed passive elements, such as resistors, capacitors and inductors into the ceramic package minimizing the size of the completed module. The permittivity and loss tangent depend on the receipt of each manufacturer. As an example of an LTCC, the A6 substrate from the vendor FERRO has been studied. Its permittivity is between 5.7 and 6.1 in a frequency range from 10 GHz to 100 GHz. The dielectric losses remain relatively low over the frequency range being between 0.0007 and 0.002.

Teflon (PTFE) resin based materials [43] are characterized for having a very low loss tangent at high frequencies, excellent resistance to processing chemicals, low moisture absorption and a high temperature resistance. Different materials with different dielectric constants from the vendor Rogers have been studied. This materials are RT/Duroid 5880, RO 4003C, RT/Duroid 6010 and RO 3006.

Quartz dielectric substrate [44] is characterized for its low and flat dielectric loss at millimeter-wave frequencies, being between 0.0001 and 0.0007 in a frequency range from 10 GHz to 60

GHz. The Quartz permittivity remains very stable along the frequency range with an approximate value of 3.9. Characteristics such as high stability against a variety of solvents, high temperature stability over a wide temperature range, high flatness and thickness uniformity make Quartz a good substrate candidate in complex fabrication processes.

In Fig. 3.1(a) the relative permittivity is shown along frequency for the BCB, A6 LTCC and Quartz. Fig. 3.1(b) shows the dielectric constant for the four different PTFE based materials from Rogers under study in a frequency range between 10 and 50 GHz. It can be seen a very good stability along frequency for the PTFE and Quartz materials. Fig. 3.1(c) and Fig. 3.1(d) compare the dielectric losses at a high frequencies range. Because their low loss tangent, Rogers RT/Duroid 5880 or quartz substrates seem to be adequate for those applications where feed network losses are important.

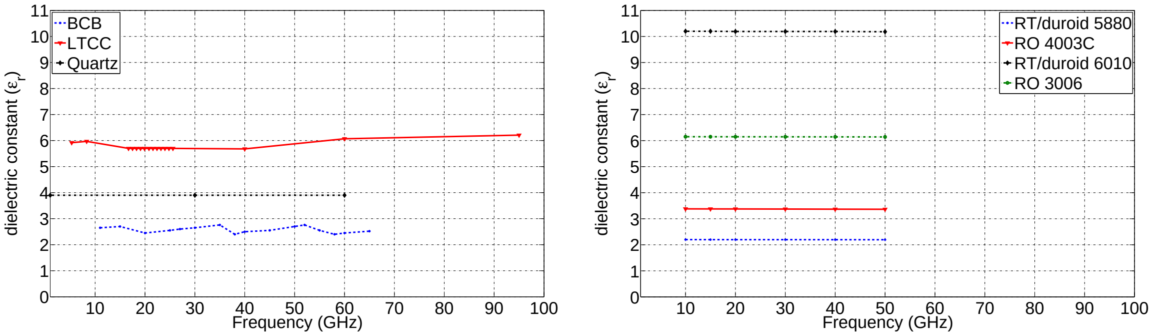

(a) BCB, A6 LTCC and Quartz (b) Rogers PTFE based materials

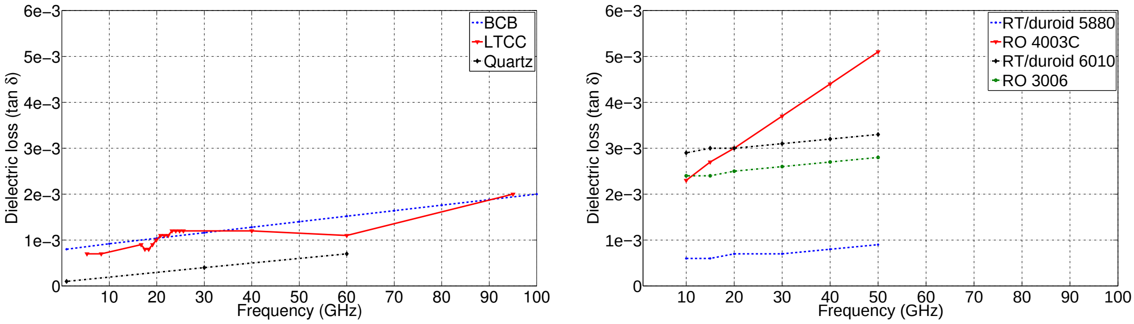

(c) BCB, A6 LTCC and Quartz (d) Rogers PTFE based materials

Figure 3.1: Millimeter-wave dielectric substrates permittivity and tangent loss

3.2 Printed Line Technologies

A transmission line may be defined as the medium that forms a path from one location to another for directing a transmission of energy. This energy may be transmitted as electromagnetic waves, or acoustic waves. This thesis will focus in transmission lines with electromagnetic waves. The electromagnetic waves propagated along a transmission line may be classified as three different types depending of the field components.

- Transverse electromagnetic (TEM): no electric nor magnetic field in the direction of propagation.
- Transverse electric (TE): no electric field in the direction of propagation.
- Transverse magnetic (TM): no magnetic field in the direction of propagation.

Geometries of transmission line include parallel-line, coaxial cable and waveguide. Planar transmission systems can be conceived as a progressive evolution of the coaxial and parallel-line transmission systems [45]. The use of lithography techniques as a manufacturing process of planar transmission lines results into the so-called printed lines.

Characteristic impedance (Z_0) of a transmission line is defined as the ratio between a single pair of voltage and current waves propagating along the line in the absence of reflections. Z_0 is computed in ohms and the most typical values used are 50 and 75 ohms. When transmitting energy to a load through a transmission line, it is desirable that as much energy as possible is absorbed by the load and as little as possible is reflected back to the source. As it is well known, this can be ensured by matching the load impedance (Z_L) to the transmission line characteristic impedance (Z_0). Equivalently, ensuring that the source impedance (Z_g) is matched to the line characteristic impedance, the power transferred from the source to the transmission line will be maximized (Fig. 3.2)

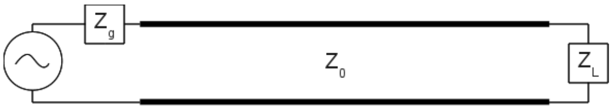

Figure 3.2: Transmission line for a matched load and generator

Depending on the medium characteristics, some of the power fed to the transmission line is being attenuated. The attenuation for each type of transmission line, as described in [46], can be caused by either dielectric losses (α_d) or conductor losses (α_c), being the total attenuation (α) computed as in equation 3.2. Conductor or ohmic losses are proportional to the square root of the frequency and it is a consequence of the conductor conductivity. Dielectric losses are proportional to the frequency and they are mainly caused by the insulating material inside the transmission line that absorbs energy from the alternating electric field and converts it to heat. Although both attenuations increase with frequency, at low frequencies the attenuation due to conductor losses dominates, while at high frequencies the tendency is reversed and the attenuation due to dielectric losses is the dominant. The total loss of power in a transmission line is normally computed as Nepers per meter (Np/m) even though very often is presented as decibels per meter (dB/m).

$$\alpha_{tot} = \alpha_{die} + \alpha_{con} \qquad Np/m \tag{3.2}$$

Another observed mechanism of losing energy is the attenuation due to radiation. It is not really attenuation in the sense of the word that the energy goes up in heat, but it is more of a leakage loss. There is not a simple way to estimate the radiation loss using transmission models, being necessary the use of 3D electromagnetic simulator tools, such as Ansoft HFFS, Momentum or CST. A study of the attenuation in the three millimeter-wave most used printed transmission lines (Microstrip, Stripline and CoPlanar Waveguide) has been done. The radiation loss has not been taken into account because its dependence on the complete feed network geometry. The results are presented by length unit.

3.2.1 Microstrip Line

The geometry of a microstrip line (Fig. 3.3) consists of a conductor strip with thickness (t_{str}) and width (w_{str}), printed on a grounded dielectric substrate of thickness (h_{die}), and with a relative permittivity (ε_r) and loss tangent ($tan\delta$).

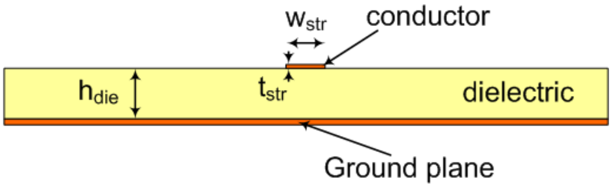

Figure 3.3: Microstrip line geometry

Microstrip line is characterized for its easy fabrication process and its easy integration with active and passive components, that may be mounted on top of the board. Some disadvantages of this type of lines are the low level of isolation which may affect the circuit response. Another disadvantage is its frequency dispersive character, in other words, that different frequencies travel at slightly different speeds which reduces the frequency bandwidth.

Considering microstrip as a quasi-TEM line, the attenuation due to dielectric losses (α_{die}) is approximated [46] by:

$$\alpha_{die} = \frac{k_0 \varepsilon_r (\varepsilon_{eff} - 1)\, tan\delta}{2\sqrt{\varepsilon_{eff}}(\varepsilon_r - 1)} \qquad Np/m \tag{3.3}$$

where $\varepsilon_{eff} = \frac{\varepsilon_r+1}{2} + \frac{\varepsilon_r-1}{2}\frac{1}{\sqrt{1+12\frac{h_{die}}{w_{str}}}}$ is the effective permittivity and $k_0 = \frac{2\pi f}{c_0}$ is the wave number in vacuum.

An approximation of the attenuation due to conductor losses (α_{con}) is given in [47] as:

$$\alpha_{con} = \frac{R_s}{Z_0 \mathrm{w}_{str}} \qquad Np/m \tag{3.4}$$

where Z_0 is the line characteristic impedance and R_s is the surface resistance of the conductor.

Fig. 3.4 shows the total attenuation, together with the ohmic and dielectric losses, for four different dielectric permittivities, related to PTFE, BCB, Quartz and LTCC. Focusing on the attenuation due to different permittivities, the substrate thickness (h_{die}) and loss tangent ($tan\delta$) have been kept equal for each case, while the strip width has been reassigned for each frequency in order to have a desired characteristic impedance of 50Ω. Both, ohmic and dielectric, losses increase with frequency, thus the total attenuation also increases with it. It can be observed the highest contribution of the conductor losses when at low frequencies and a more equitable contribution of both losses at high frequencies. The increase of permittivity is translated into an increase of the dielectric losses and consequently an increase of the total attenuation.

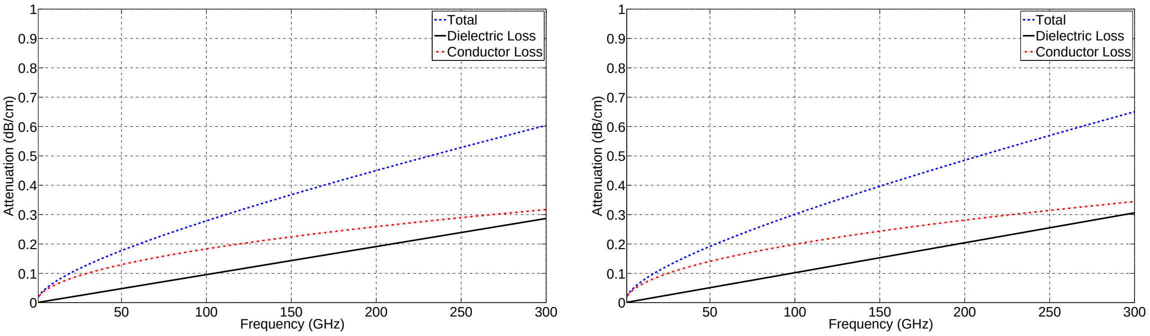

(a) $\varepsilon_r = 2.2$ (b) $\varepsilon_r = 2.5$

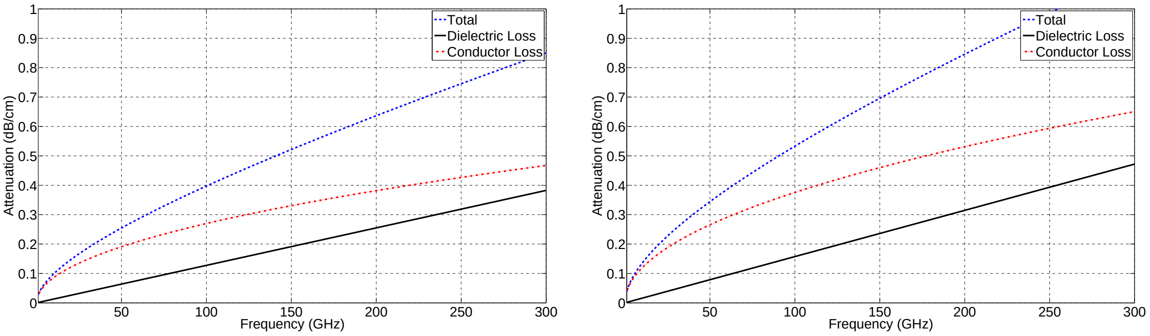

(c) $\varepsilon_r = 3.9$ (d) $\varepsilon_r = 6.0$

Figure 3.4: Microstrip attenuation (dB/cm) for different relative permittivity (ε_r), with $\tan\delta$=0.0009 and $h_{die} = 254\mu m$

Fig. 3.5 illustrates the attenuation for four different values of substrate's loss tangent. The cases under study correspond to PTFE, BCB, Quartz and LTCC. Focusing on the study of the attenuation due to the different values of $tan\delta$, the permittivity (ε_r) and the thickness (h_{die}) have been fixed. The attenuation not only increases with frequency but also increases with $tan\delta$. The attenuation component which is more effected by increasing the loss tangent is the dielectric losses as expected from the analytical formula (equation 3.3), By the other hand, the conductor losses are not effected by the loss tangent variations, remaining constant for the different values.

In Fig. 3.6, the attenuation for different dielectric thickness is represented. The two thickness values used are the typical dielectric thickness of the teflon based materials from Rogers. A thicker dielectric results in a wider strip, and therefore ohmic losses are reduced. A problem with a thick substrate is the trapping of surface waves, which will radiate in a parasitic form resulting into the so-called attenuation due to radiation.

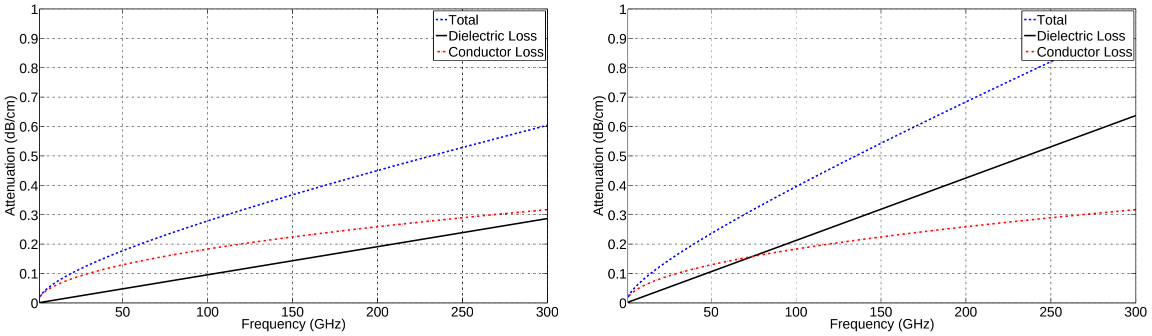

(a) $\tan\delta = 0.0009$

(b) $\tan\delta = 0.002$

Figure 3.5: Microstrip attenuation (dB/cm) for different loss tangent ($\tan\delta$), with ε_r=2.2 and $h_{die} = 254\mu m$

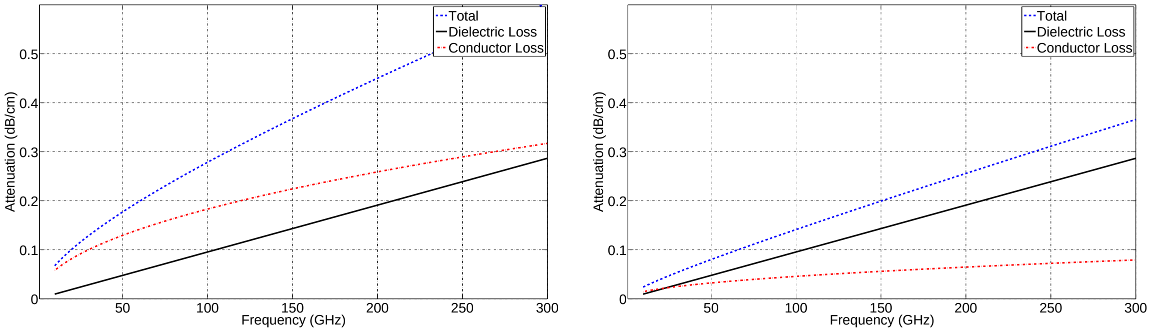

(a) h_{die} = 0.254 mm

(b) h_{die} = 1.016 mm

Figure 3.6: Microstrip attenuation (dB/cm) for different dielectric thickness (h_{die}), with ε_r=2.2 and $\tan\delta$=0.0009

3.2.2 Stripline

Stripline (Fig. 3.7) consists of a conducting strip with thickness (t_{str}) and width (w_{str}), centered between two wide ground planes separated by a distance (h_{die}). The region between the ground planes is filled with a dielectric substrate with a permittivity (ε_r) and loss tangent ($tan\delta$).

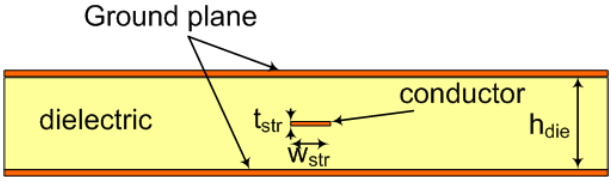

Figure 3.7: Stripline geometry

Stripline is characterized for operating in TEM mode, which means that is non-dispersive. This is translated in wider bandwidths than the ones obtained with microstrip line. This type of printed line is also characterized for having a high isolation level with elements outside the ground planes limits. Main disadvantages of striplines lay in the fabrication process, with a higher cost and complexity than microstrip and a higher difficulty of combination with lumped-elements and active components.

Since stripline is a TEM-type line, the attenuation due to dielectric losses is computed like any other TEM line [48]:

$$\alpha_{die} = \frac{k_{die} tan\delta}{2} \qquad Np/m \tag{3.5}$$

where $k_{die} = \frac{2\pi f\sqrt{\varepsilon_r}}{c_0}$ is the wave number in the dielectric.

The attenuation due to conductor losses is given in [46] by equation 3.6.

$$\alpha_{con} = \begin{cases} \dfrac{2.7\times10^{-3}R_s\varepsilon_r Z_0}{30\pi(h_{die}-t_{str})}A & for\ \ \sqrt{\varepsilon_r}Z_0 < 120 \\ \dfrac{0.16R_s}{Z_0 h_{die}}B & for\ \ \sqrt{\varepsilon_r}Z_0 > 120 \end{cases} \qquad Np/m \tag{3.6}$$

with

$$\begin{aligned} A &= 1+\frac{2\mathrm{w}_{str}}{h_{die}-t_{str}}+\frac{1}{\pi}\frac{h_{die}+t_{str}}{h_{die}-t_{str}}\ln\left(\frac{2h_{die}-t_{str}}{t_{str}}\right) \\ B &= 1+\frac{h_{die}}{(0.5\mathrm{w}_{str}+0.7t_{str})}\left(0.5+\frac{0.414t_{str}}{\mathrm{w}_{str}}+\frac{1}{2\pi}\ln\left(\frac{4\pi\mathrm{w}_{str}}{t_{str}}\right)\right) \end{aligned}$$

where Z_0 is the line characteristic impedance, ε_r is the dielectric relative permittivity and R_s is the surface resistance of the conductor.

Fig. 3.8 shows the ohmic and dielectric losses, and the total attenuation, for the dielectric constants of PTFE, BCB, Quartz and LTCC. In order to analyze the attenuation behavior due to the dielectric permittivity, the thickness (h_{die}) and loss tangent ($tan\delta$) have been fixed constant and the strip width (w_{str}) has been reassigned in each case to have a 50Ω characteristic impedance line. Similar to microstrip lines, the total attenuation increases with the frequency. It can be seen that at low frequencies, the conductor losses have a higher contribution to the total attenuation while at high frequencies the dielectric losses have higher contribution. Also it can be concluded that an increase of permittivity is translated into an increase in ohmic and dielectric losses, and consequently into an increase of the total attenuation.

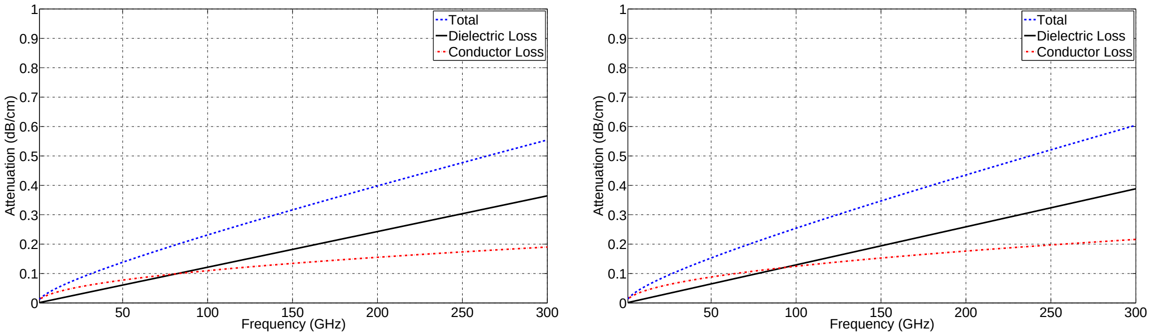

(a) $\varepsilon_r = 2.2$ (b) $\varepsilon_r = 2.5$

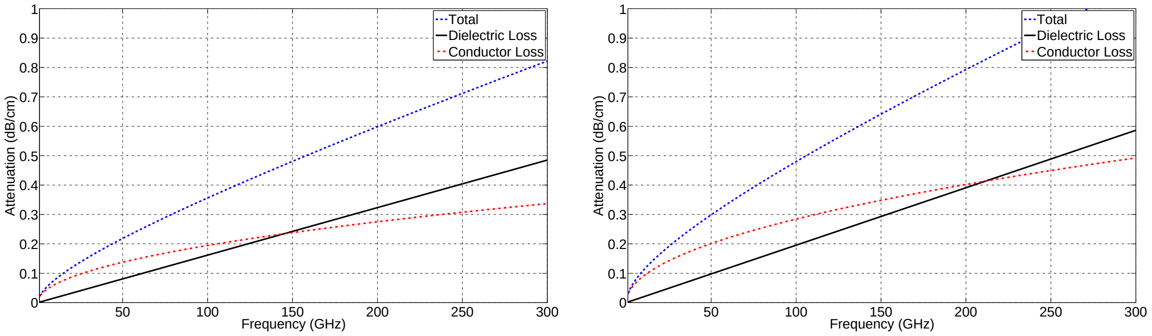

(c) $\varepsilon_r = 3.9$ (d) $\varepsilon_r = 6.0$

Figure 3.8: Stripline attenuation (dB/cm) for different relative permittivity (ε_r), with tan δ=0.0009 and $h_{die} = 508\mu m$

The attenuation related to different values of $tan\delta$ is presented in Fig. 3.9. The values chosen are the loss tangent of PTFE and LTCC, being them a representative samples of the different $tan\delta$ used at MMW frequencies. In this case, the permittivity (ε_r), the thickness (h_{die}) and the strip width (w_{str}) have been fixed constant. It can be seen that increasing $tan\delta$ is translated into an increase of the dielectric losses, while the ohmic losses remain basically invariant to loss tangent variations. .

Fig. 3.10 represents the attenuation as a function of the substrate thickness. The two thickness values correspond to stacking together two typical commercial dielectric sheets, being in this case $0.508mm = 2 \times 0.254mm$ and $2.032mm = 2 \times 1.016mm$ Similar to microstrip lines, a thicker dielectric results into a wider strip and into a reduction of ohmic losses.

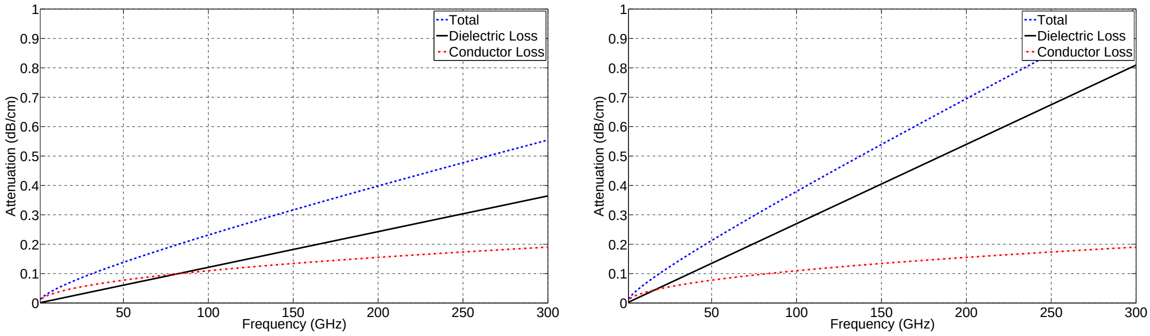

(a) $\tan\delta = 0.0009$ (b) $\tan\delta = 0.002$

Figure 3.9: Stripline attenuation (dB/cm) for different loss tangent ($\tan\delta$), with ε_r=2.2 and $h_{die} = 508\mu m$

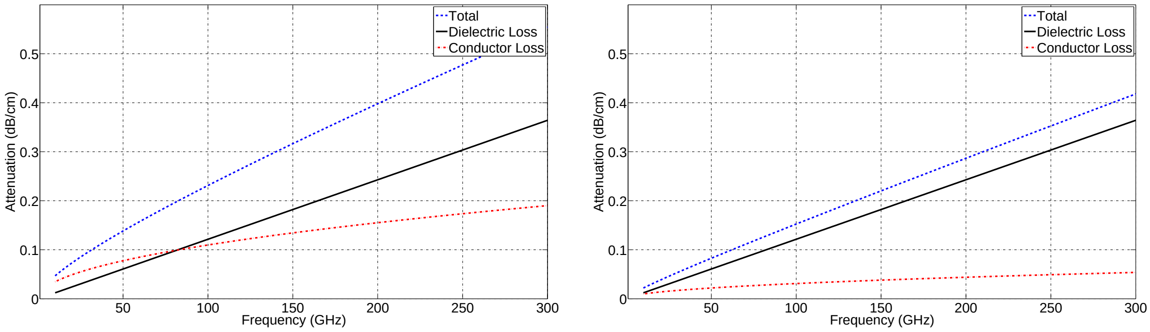

(a) thickness = 0.508 mm (b) thickness = 2.032 mm

Figure 3.10: Stripline attenuation (dB/cm) for different dielectric thickness (h_{die}), with ε_r=2.2 and $\tan\delta$=0.0009

3.2.3 CoPlanar Waveguide (CPW)

A CoPlanar Waveguide (Fig. 3.11) on a dielectric substrate with thickness (h_{die}), consists of a center strip with thickness (t_{str}) and width (w_{str}), separated by a narrow gap (g_{ap}) from two ground planes on either side.

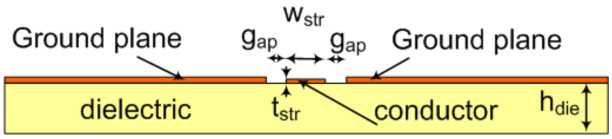

Figure 3.11: CoPlanar Waveguide (CPW) geometry

CPW supports a quasi-TEM mode of propagation. Some of the advantages of using this technology lay into its fabrication simplicity, easy devices surface mounting, low losses and high isolation with other elements in the same plane. Furthermore, the characteristic impedance is determined by the ratio $\frac{w_{str}}{g_{ap}}$ which means that size reduction is not a problem, except for fabrication constraints. Disadvantages respect to other technologies are the low effective dielectric constant ε_{eff} which increases the circuit size; and the spurious transmission odd modes that may be excited if the ground planes are not connected in discontinuities such as tee junctions.

The attenuation due to dielectric losses can be approximated [49] as:

$$\alpha_{die} = \frac{\pi f}{c_0} \frac{\varepsilon_r}{\sqrt{\varepsilon_{eff}}} tan\delta Q_{fil} \qquad Np/m \tag{3.7}$$

The effective dielectric constant (ε_{eff}) and the filling factor (Q_{fil}) for CPW are defined as:

$$\begin{aligned} \varepsilon_{eff} &= 1 + Q_{fil}(\varepsilon_r - 1) \\ Q_{fil} &= \frac{1}{2} \frac{K(k_1)}{K(k_1')} \frac{K(k_0')}{K(k_0)} \end{aligned} \tag{3.8}$$

Terms $K(k_1)$ and $K(k_0)$ are the complete elliptic integrals of the first kind with module k_1 and k_0, while terms k_1' and k_0' are the complementary module, given by

$$\begin{aligned} k_1 &= \frac{\sinh(\pi \mathrm{w}_{str}/4h_{die})}{\sinh[\pi(\mathrm{w}_{str} + 2g_{ap})/4h_{die}]} \qquad & k_1' &= \sqrt{1 - k_1^2} \\ k_0 &= \frac{\mathrm{w}_{str}}{\mathrm{w}_{str} + 2g_{ap}} & k_0' &= \sqrt{1 - k_0^2} \end{aligned} \tag{3.9}$$

The attenuation due to conductor losses is given by equation 3.10.

$$\alpha_{con} = \frac{R_c + R_g}{2Z_0} \qquad Np/m \tag{3.10}$$

with

$$\begin{aligned} R_c &= \frac{R_s}{4\mathrm{w}_{str}(1 - k_0^2)K^2(k_0)} \left[\pi + \ln\left(\frac{4\pi \mathrm{w}_{str}}{t_{str}}\right) - k_0 \ln\left(\frac{1 + k_0}{1 - k_0}\right)\right] \\ R_g &= \frac{k_0 R_s}{4\mathrm{w}_{str}(1 - k_0^2)K^2(k_0)} \left[\pi + \ln\left(\frac{4\pi(\mathrm{w}_{str} + 2g_{ap})}{t_{str}}\right) - \frac{1}{k_0} \ln\left(\frac{1 + k_0}{1 - k_0}\right)\right] \\ R_s &= \sqrt{\frac{w\mu_0\rho}{2}} \end{aligned} \tag{3.11}$$

The dielectric constant effect on the total attenuation has been analyzed using the ε_r of four MMW materials like PTFE, BCB, Quartz and LTCC. The dielectric thickness (h_{die}), the loss tangent ($tan\delta$) and the strip width (w_{str}) are set constant, while the gap between the conductor strip and the ground planes (g_{ap}) varies for each permittivity in order to maintain the characteristic impedance of 50Ω. Fig. 3.12 illustrates the attenuation together with its ohmic and dielectric losses for the four different substrates. Similar to the other types of transmission lines, the attenuation increases with the frequency. In CPW lines, although the total attenuation remains similar for each different permittivity, the contribution between ohmic and dielectric losses change. While for lower permittivity ohmic losses dominate, dielectric losses dominate for higher permittivity.

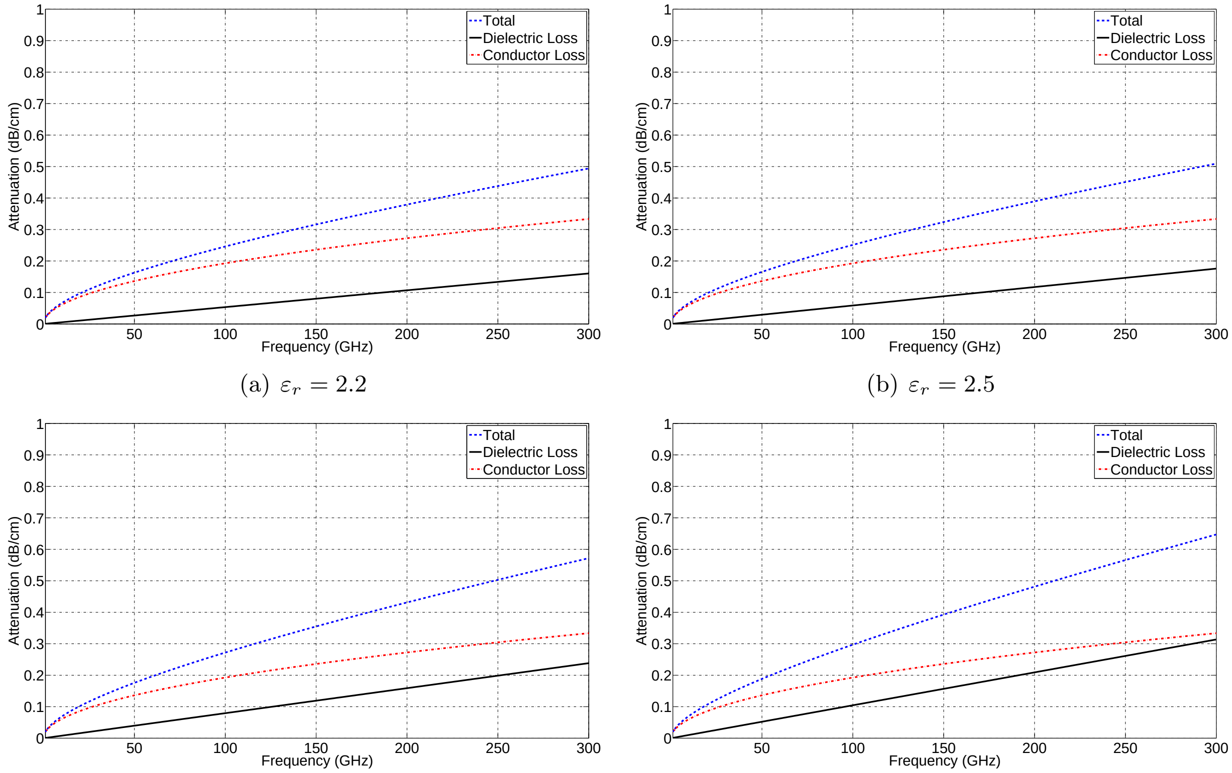

(a) $\varepsilon_r = 2.2$

(b) $\varepsilon_r = 2.5$

(c) $\varepsilon_r = 3.9$

(d) $\varepsilon_r = 6.0$

Figure 3.12: CoPlanar Waveguide (CPW) attenuation (dB/cm) for different relative permittivity (ε_r), with $\tan\delta$=0.0009 and $h_{die} = 254\mu m$

Fig. 3.13 represents the attenuation for different values of the loss tangent ($tan\delta$). Two different values have been chosen, representing the MMW materials with a low $tan\delta$ and materials with high $tan\delta$. In this case, the permittivity (ε_r), the thickness (h_{die}), the strip width (w_{str}) and the gap width (g_{ap}) are constant. It can be seen that an increase of $tan\delta$ is translated into an increase of the dielectric losses and therefore an increase of the total attenuation.

Fig.3.14 represents the attenuation as a function of the substrate thickness. Due to the physical structure of the CPW lines, the transmitted fields are confined mainly in the gaps between the strip line and the ground plane, and the dielectric thickness has a low influence in the total attenuation.

Finally, Fig. 3.15 shows the attenuation for different strip line widths. In order to maintain the line characteristic impedance of 50Ω determined by a ration between w_{str} and g_{ap}, the gap width has to be reassigned for each strip width. It can be seen that for wider conductor string the attenuation decreases.

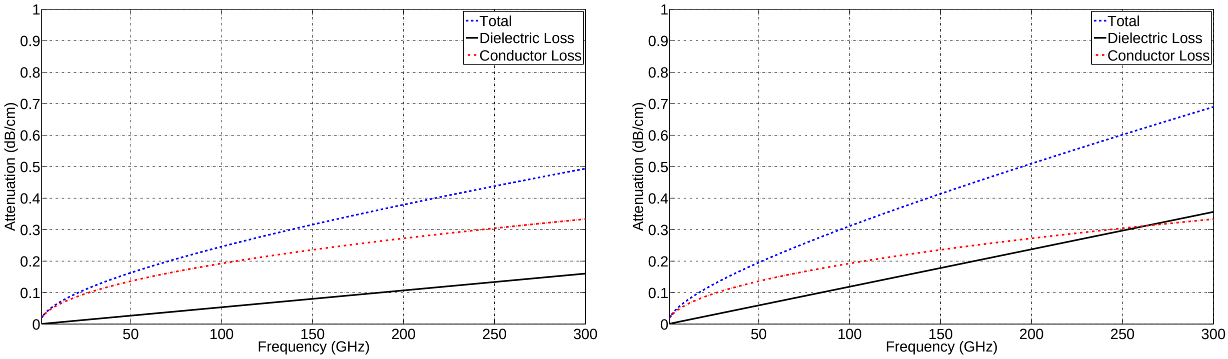

(a) $\tan\delta = 0.0009$ (b) $\tan\delta = 0.002$

Figure 3.13: CoPlanar Waveguide (CPW) attenuation (dB/cm) for different loss tangent ($\tan\delta$), with ε_r=2.2 and $h_{die} = 254\mu m$

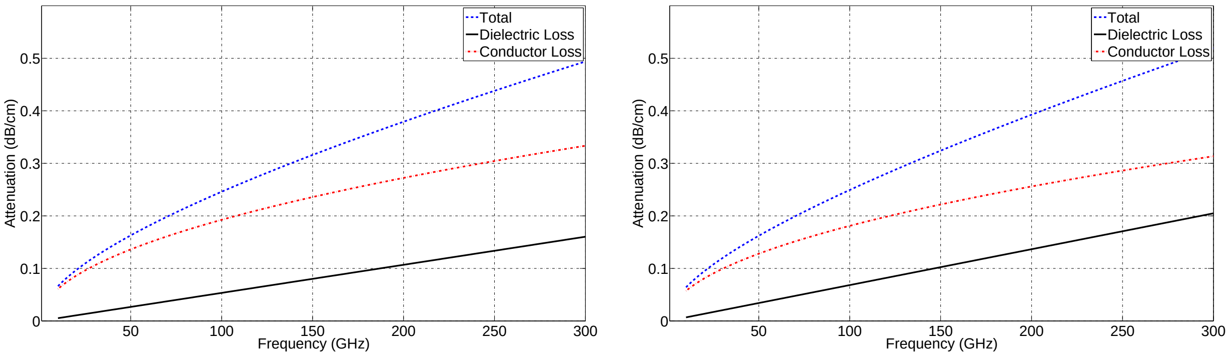

(a) thickness = 0.254 mm (b) thickness = 1.016 mm

Figure 3.14: CoPlanar Waveguide (CPW) attenuation (dB/cm) for different dielectric thickness (h_{die}), with ε_r=2.2 and $\tan\delta$=0.0009

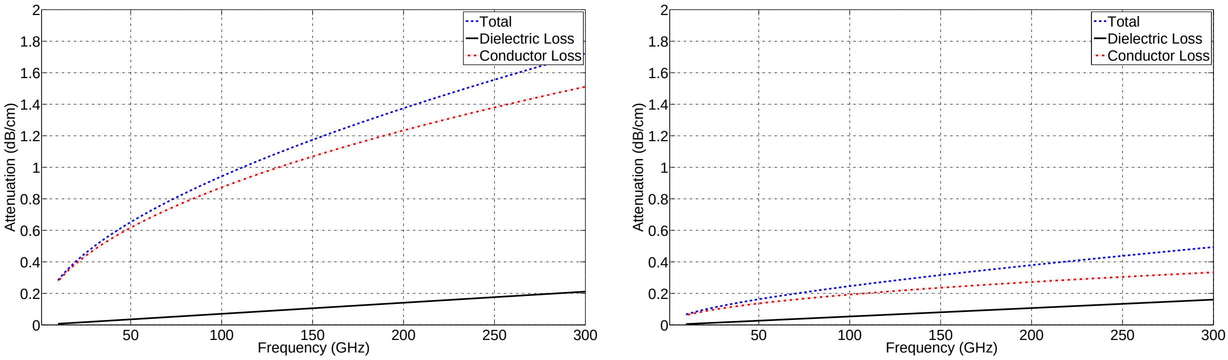

(a) strip width = 0.1 mm (b) strip width = 1.0 mm

Figure 3.15: CoPlanar Waveguide (CPW) attenuation (dB/cm) for different w$_{str}$, with ε_r=2.2, $\tan\delta$=0.0009 and $h_{die} = 254\mu m$

3.2.4 MMW Transmission Line Comparison

Three types of printed transmission lines (microstrip, stripline and CPW) have been studied. By varying structural parameters such as the dielectric thickness (h_{die}) or the strip width (w$_{str}$), or varying substrate parameters such as the permittivity (ε_r) or loss tangent ($tan\delta$), the attenuation together with its components (ohmic and dielectric losses) have been analyzed.

Fig. 3.16 presents a more specific study of each type of line, done by using four materials very used in MMW applications, such as Rogers RT/Duroid 5880, BCB, Quartz and FERRO A6 LTCC. The permittivity (ε_r) and loss tangent ($tan\delta$) of these materials are presented in Table 3.1. Those values have been considered to present a high stability along frequency. This consideration could change the attenuation results depending on the unknown materials stability at the highest frequencies. The dielectric thickness used in the microstrip and CPW cases is equal, while in the stripline case, the thickness is double than the other cases. Also, the distance between the strip and the ground planes in the stripline case will be the same than the one in the microstrip case.

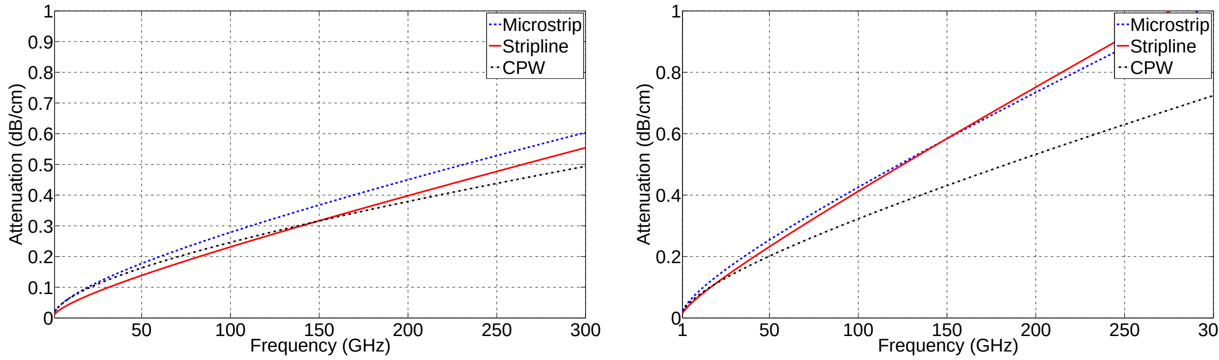

(a) Rogers RT/Duroid 5880 ($\varepsilon_r = 2.2$ and $tan\delta = 0.0009$)

(b) BCB ($\varepsilon_r = 2.5$ and $tan\delta = 0.0092$)

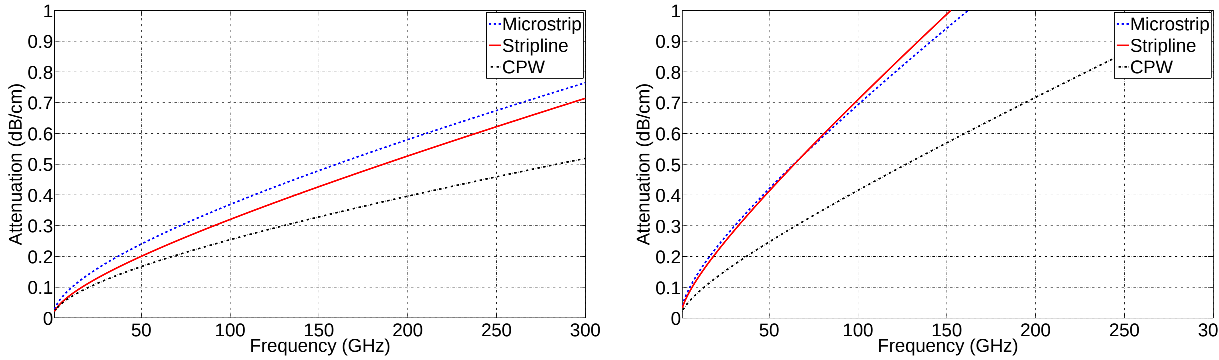

(c) Quartz ($\varepsilon_r = 3.9$ and $tan\delta = 0.0007$)

(d) LTCC ($\varepsilon_r = 6.0$ and $tan\delta = 0.002$)

Figure 3.16: MMW materials attenuation comparison

In the teflon based material (Fig. 3.16(a)) it can be seen a similar attenuation for the different types of line. The minimum losses at low frequencies corresponds to the use of Stripline while at high frequencies corresponds to CPW. When using BCB (Fig. 3.16(b)), the attenuation for each line type is considerably higher than in other materials because its higher $tan\delta$. Quartz (Fig. 3.16(c)) has similar losses using microstrip line than stripline while the attenuation is reduced when using CPW. The losses in LTCC are elevated with microstrip and stripline but considerably lower with CPW. In general, the dielectric losses become dominant in microstrip and stripline when the frequency increases due to the fact that the fields are confined in the dielectric. In the other hand, the CPW concentrates the fields between the dielectric and the air, reducing drastically the influence of the dielectric on the final attenuation. In absolute attenuation terms, Quartz and RT/Duroid 5880 are the materials with lower losses for all the line types.

3.3 RF-MEMS Switches

A switch is characterized for being a device which connects or breaks an electric circuit. In DC regime, a switch operates simply as either a through or a break in the conduction path. When a switch operates in Radio Frequency (RF), additional electrical properties of the switch like resistance, capacitance and inductance will be included in the analysis of the system.

Mechanical switches such as RF-MEMS and solid state switches such as PIN diodes and FET are the most common used in RF. The selection of one type or the other rely fundamentally on the required switching speed and, necessary isolation and loss levels. Other critical parameters to be considered are impedance characteristics, activation voltage, number of cycles, consumption and dimensions.

RF-MEMS switches are characterized by using a mechanical movement to achieve a short-circuit or an open-circuit in the RF system. Two different types can be found: metal-contact switches (Fig. 3.17(a)) and capacitive switches (Fig. 3.17(b)). The metal-contact switches use physical contact with low resistance to achieve low insertion loss when actuated and can operate from DC to 60 GHz. Capacitive switches are characterized by the capacitance ratio between the up-state (open-circuit) and down-state (short-circuit) positions . Capacitive switches actuate from 6 to 120 GHz [16]. The mechanical movement may be actuated by using electrostatic, magnetostatic, piezoelectric or thermal design. The electrostatic type switches are the only ones that have been demonstrated to work in a frequency range of 0.1 - 100 GHz with high reliability at low RF power for metal-contact type and at medium power for capacitive contact type.

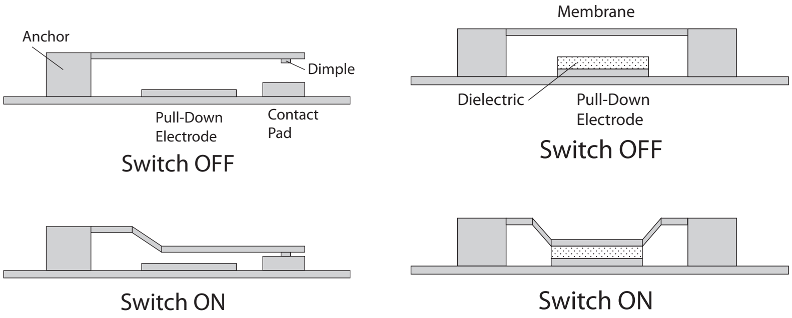

(a) Metal-contact switch (b) Capacitive switch

Figure 3.17: RF-MEMS switch Types

Like any two-terminal RF device, the RF-MEMS switches can be placed either in series or in parallel configuration. Typically, metal-contact switches are placed in series while capacitive switches are used in parallel configuration. This is due to the higher facility to achieve a good isolation with a limited impedance ratio in a parallel-circuit that in a series circuit.

When comparing the three different RF-switches, the main advantages and disadvantages of using RF-MEMS in front of using PIN diode or FET switches are:

Advantages

- Very High Isolation: The air gap between the Source and the Drain of a RF-MEMS switch results in a very low capacitance (2-4 fF) when the switch is turned off which is translated onto an excellent isolation.
- Very Low Insertion Loss: RF-MEMS switches have a very low insertion loss up to 100 GHz when the switch is in ON-state.
- Linearity: The extremely linearity of the RF-MEMS results in a very low intermodulation product in switching operations. Their performance is around 40 dB better than PIN diodes or FET switches.
- Manufacturing Cost: RF-MEMS are fabricated under surface microfabrication techniques such as photolithography and can be fabricated on substrates like Quartz, LTCC, silicon or GaAs.

Disadvantages

- Low Speed: The RF-MEMS switching time is in the order of microseconds (μs) while FET switches and PIN diodes have a switch time of nanoseconds (ns), which is more adequate to the requirements of most communications and radar systems.
- High Actuation Voltage: The necessity of an actuation voltage of 20-120 V makes the necessity to have voltage up-converter devices while solid state switches require a lower voltage of 3-5 V.
- Power Handling: The power handled by most RF-MEMS is low next to the power handled by other switches.
- Reliability: One of the most disadvantage of RF-MEMS switches is their reliability which is limited by the effect of the contact forces in metal-contact switches, and by the dielectric charging in capacitive switches.
- Packaging: RF-MEMS switches need to be package in inert atmospheres (Nitrogen, Argon, etc.) and in very low humidity to have an hermetic seal, which make a relatively high

cost process. The packaging elevated cost contrasts with the low manufacturing cost. The possibility of integrating the RF-MEMS switches with the RF circuit when manufacturing and then packaging the whole final system is an alternative solution which may reduce the final system cost.

Parameter	RF-MEMS	PIN Diode	FET
Voltage [V]	20-120	3-5	3-5
Current [A]	0	3-20	0
Power Consumption [mW]	0.05-0.1	5-100	0.05-0.1
Switching Time	1-200 μs	1-100ns	1-100ns
Cup (Series) [pf]	1-6	40-80	70-140
Rs (Series) [Ω]	0.5-2	2-4	4-6
Capacitance Ratio	40-500	10	-
Cutoff Freq. [THz]	20-80	1-4	0.5-2
Isolation (1-10 GHz)	Very high	High	Medium
Isolation (10-40 GHz)	Very high	Medium	Low
Isolation (60-100 GHz)	High	Medium	-
Loss (1-100 GHz)	0.05-0.2	0.3-1.2	0.4-2.5
Power Handling [W]	<0.5	<10	<10

Table 3.2: Performance comparison of FET, PIN and RF-MEMS switches

Table 3.2 summarizes the main parameters which are normally compared between RF-MEMS, PIN diode and FET switches in order to decide which RF-switch should be used for each application. Because their RF performance along the millimeter-wave frequencies together with the low power consumption and dimension, RF-MEMS switch seem to be the most appropriate switch to be used for reconfigurability in MMW applications.

Chapter 4

Polarization-Reconfigurable Base-Element Antenna

The polarization diversity of an antenna is a very attractive characteristic in applications where the orientation of the antennas is unknown and has a high effect in the communication link performance. While in lower frequencies, the multipath communication links are often used without taking into account the importance of a good polarization matching between antennas, at Millimeter-wave frequencies the links are intended to be Line-of-sight (LOS) path or first order reflections, with very directive antennas, and polarization matching becomes crucial.

In this chapter, two different polarization reconfigurable antenna architectures are presented: *CPW Patch* antenna and *4-Qdime* antenna. The polarization reconfigurable CPW Patch antenna consists of a single reconfigurable element and has been designed to operate at Ka-band (26.5 to 40GHz) and V-band (50 to 75GHz), and its reconfigurability is obtained by RF-MEMS switches that reconfigure the antenna currents distribution. The narrow frequency bandwidth related to 3dB Axial Ratio (AR) obtained with the CPW Patch antenna has lead to the necessity to find a wider bandwidth reconfigurable composed architecture, such as the 4-Qdime antenna. This structure consists of 4 linear polarized Qdime antennas, capable to switch between polarizations by exciting each of the four elements with the appropriate amplitude and phase. Two 4-Qdime antenna prototypes have been designed to operate at V-band and W-band (75 to 110GHz) respectively.

4.1 Antenna Polarization

As described in [34], the *polarization of a radiated wave* is defined as "the property of an electromagnetic wave describing the time varying direction and relative magnitude of the electric field vector, specifically, the figure traced as a function of time by the extremity of the vector at a fixed location in space and the sense in which is traced, as observed along the direction of propagation." In other words, polarization is an indication of the electric field vector's orientation in a fixed space point along time. The *antenna polarization* is the polarization of the radiated wave evaluated usually in the far field.

The polarization may be classified as:

- **Linear**: the radiated field has only one component or the two orthogonal components are in phase which is translated into a constant direction of the field vector. (Fig. 4.1(a))

- **Circular**: the two orthogonal components have exactly the same amplitude and have a phase difference of ±90$^{\text{o}}$, resulting in a field vector which traces a circle in a plane. (Fig. 4.1(b))

- **Elliptical**: any other different than linear or circular. This case is the most general. (Fig. 4.1(c))

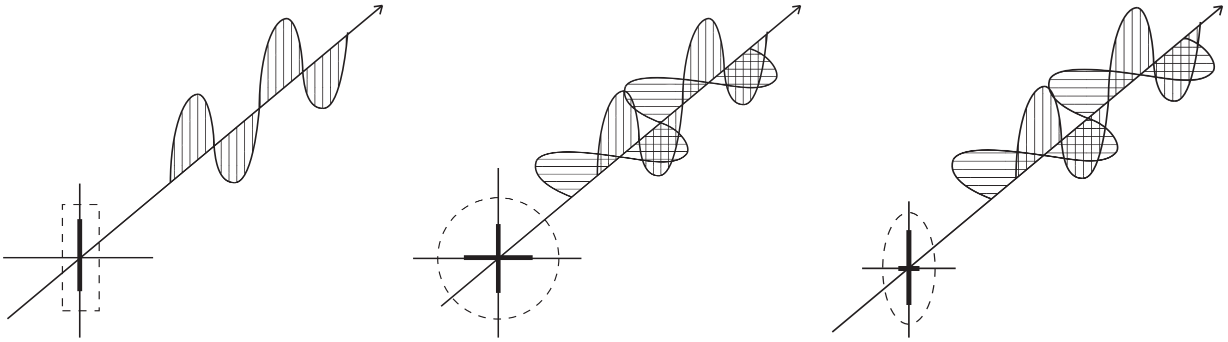

(a) Linear (b) Circular (c) Elliptical

Figure 4.1: Types of Polarization

The quality of the circular polarization is evaluated by the Axial Ratio (AR), which is defined as the ratio between the two principal axes (major and minor) of the *polarization ellipse* (Fig. 4.2) traced by the electrical field vectors amplitude (E_{x0} and E_{y0}) and phase difference ($\Delta\phi_{pol}$). The Axial Ratio is computed as:

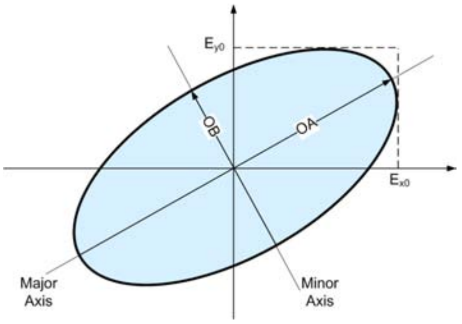

Figure 4.2: Polarization ellipse

$$AR = \frac{OA}{OB} \qquad 1 \leq AR \leq \infty \tag{4.1}$$

where

$$OA = [\tfrac{1}{2}\{E_{x0}^2 + E_{y0}^2 + [E_{x0}^4 + E_{y0}^4 + 2E_{x0}^2 E_{y0}^2 \cos 2\Delta\phi_{pol}]^{\frac{1}{2}}\}]^{\frac{1}{2}}$$

$$OB = [\tfrac{1}{2}\{E_{x0}^2 + E_{y0}^2 - [E_{x0}^4 + E_{y0}^4 + 2E_{x0}^2 E_{y0}^2 \cos 2\Delta\phi_{pol}]^{\frac{1}{2}}\}]^{\frac{1}{2}} \tag{4.2}$$

$$\Delta\phi_{pol} = \phi_{E_{x0}} - \phi_{E_{y0}}$$

Depending on the sense in which the electric field traces the polarization figure, in circular and elliptical, the polarization is designated as Right-Handed when the sense is clockwise and Left-Handed when the sense is counterclockwise. Pure circular polarization waves have an AR equal to 1 (0 dB) while pure linear polarization waves have an AR equal to ∞. For most of the applications, a polarization ellipse axes ratio better than 1:2 ($AR \leq 3dB$) is considered acceptable for an antenna with circular polarization. Antennas with an $AR \geq 20dB$ are considered to be linearly polarized. All other cases are considered to be antennas with elliptical polarization.

The antenna polarization concept is important in a communication system to assure the good performance of the link. The power loss due to polarization mismatch is described by the Polarization Loss Factor (PLF) which depends on the angle difference between the antennas radiated E-fields.

$$PLF = cos^2(\Delta\phi_{plf}) \tag{4.3}$$

Two antennas with orthogonal polarizations will have a $PLF = 0$ and will not communicate while two antennas with the same polarization will have $PLF = 1$ and the energy between the received wave and the antenna will be completely transferred. The Polarization Loss Factor between any pure linearly polarized antenna and any pure circularly polarized antenna is PLF=0.5 which means that only half of the power is transferred (-3dB), being this acceptable in some applications.

4.2 CPW Patch Antenna

The CPW Patch antenna presented in this thesis (Fig. 4.3) consists of a square coplanar patch fabricated on gold and printed on a very thin ($500\mu m$) synthetic quartz glass substrate. The quartz properties at Millimeter-wave frequencies are $\epsilon_r = 3.9$ and $tan\delta = 7 \cdot 10^{-4}$ [44]. The structure has been modeled and optimized with the finite element method simulator Ansoft HFSS to operate at Ka-band and V-band. The use of CPW technology leads to a bidirectional antenna with wider bandwidth than other technologies such as microstrip or Grounded-CoPlanar Waveguide (GCPW). A square CPW patch radiates in Linear Polarization (LP), while Circular Polarization (CP) is achieved by providing the necessary perturbation on the patch to obtain the two required orthogonal resonant modes [50]. The use of RF-MEMS switches allows to reconfigure the currents distribution and therefore the radiated fields. The polarization of the reconfigurable coplanar patch antenna presented can be configured in Vertical Linear Polarization (VLP), Right-Handed Circular

Polarization (RHCP) and Left-Handed Circular Polarization (LHCP). Due to non-symmetry in $\phi = 90$ plane, to obtain the antenna configured in Horizontal Linear Polarization (HLP) would be needed to change the CPW feeding mode from even to odd.

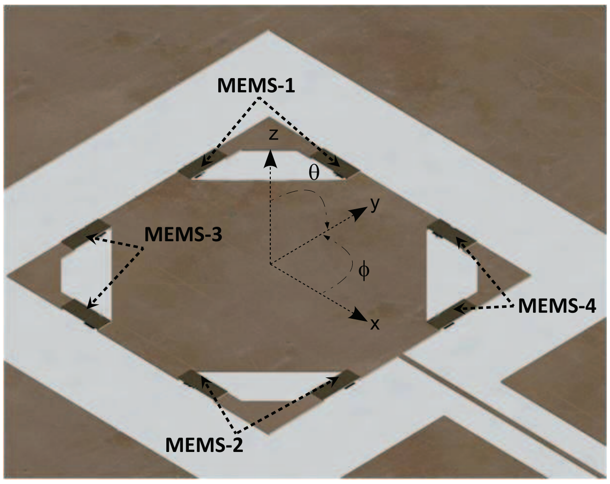

Figure 4.3: RF-MEMS-Integrated Polarization Reconfigurable CPW Patch Antenna

The antenna feeding is done with CoPlanar Waveguide (CPW) in order to reduce transmission line losses. Because high impedance nature of CPW structures, the antenna is preceded by a lambda quarter transformer, resulting an input impedance of 50Ω. In order to avoid the excitation of the CPW line odd-modes, air-bridges are used along the transmission line. Given the application and the operating frequency, the CPW line has been designed taking into account the manufacturing limitations and tolerances, together with the dimensions of the feeding coaxial connector or a standard $150\mu m$ pitch ground-signal-ground (GSG) probe.

4.2.1 Linear Polarization CPW Patch Antenna

The basic structure of the antenna consists of a square patch surrounded by ground plane as illustrated in Fig. 4.4(a) . This antenna is named after microstrip patch antenna because the existing similarity between the field distribution along the surrounding slot (Fig. 4.4(b)) with the field distribution in the microstrip patch edges [51]: uniform distribution in the horizontal slots (along y-axis) and sinusoidal distribution in the vertical slots (along x-axis). This field distribution assures a linear polarized radiated field with a x-oriented vertical component (VLP) because the fields in the horizontal slots are added while the fields in the vertical slots cancel each other.

The length of the patch side (l_{pat}) together with the slot width (w_{slt}) have resulted to lead the square-slot inner perimeter to be equal to one guided wavelength (λ_s), resulting $l_{pat} + \mathrm{w}_{slt} \approx \lambda_s/4$. From [52], the wavelength in the slot is computed as:

- For $0.002 \leq \mathrm{w}_{slt}/h_{die} < 0.2$

$$\frac{\lambda_s}{\lambda_0} = 0.923 - 0.448 \log \varepsilon_r + 0.2\frac{\mathrm{w}_{slt}}{h_{die}} - \left(0.29\frac{\mathrm{w}_{slt}}{h_{die}} + 0.047\right) \log\left(\frac{h_{die}}{\lambda_0}10^2\right) \tag{4.4}$$

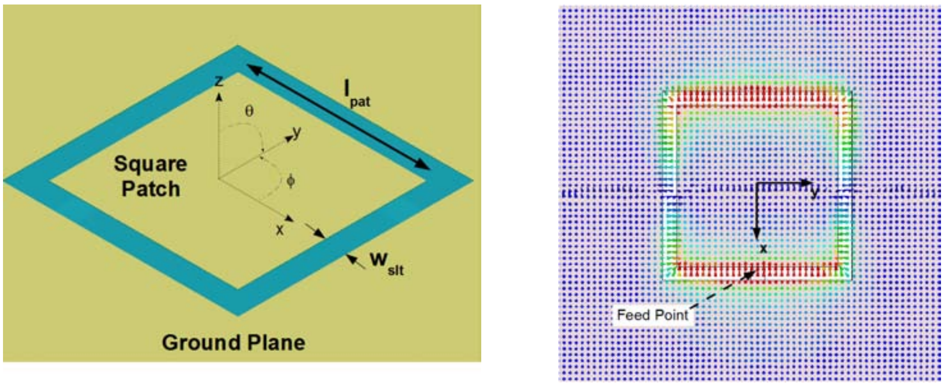

(a) Architecture (b) Electric Field Distribution

Figure 4.4: Square CPW Patch Antenna

- For $0.2 \leq \mathrm{w}_{slt}/h_{die} < 1.0$

$$\frac{\lambda_s}{\lambda_0} = 0.987 - 0.483 \log \varepsilon_r + \frac{\mathrm{w}_{slt}}{h_{die}}(0.111 - 0.0022\varepsilon_r) - \left(0.121 + 0.094\frac{\mathrm{w}_{slt}}{h_{die}} - 0.0032\varepsilon_r\right) \log\left(\frac{h_{die}}{\lambda_0}10^2\right) \tag{4.5}$$

4.2.1.1 Analytic Model

An initial analysis of the square CPW patch structure has been done under the assumption of non-dielectric existence. The dielectric effect is then introduced by scaling the antenna dimensions by the inverse of the effective permittivity square root ($\sqrt{\varepsilon_{eff}}$). Inspired on the folded dipole [34], the square CPW patch can be analyzed by assuming that its voltage is decomposed into two distinct modes (Fig. 4.5): Transmission line mode and Radiation mode .

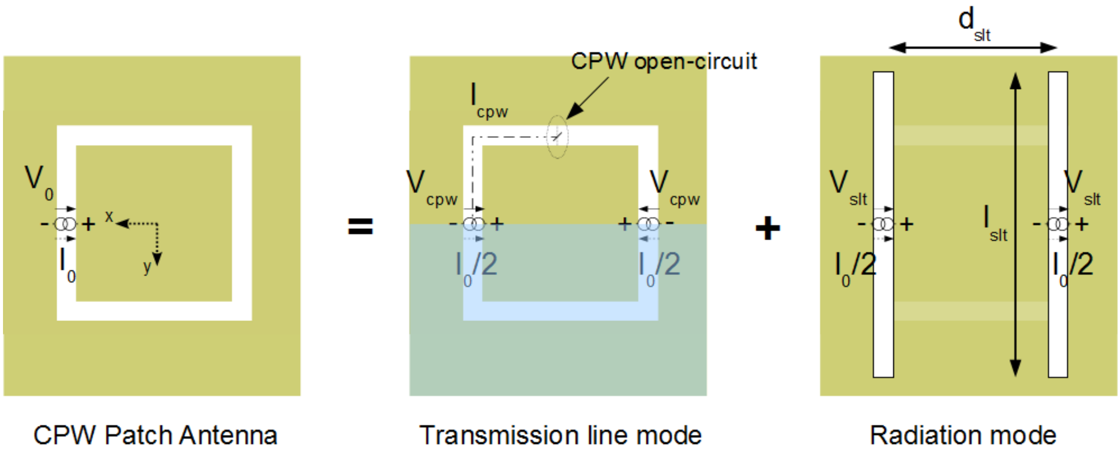

Figure 4.5: Square CPW Patch Antenna Analytical Model

To derive an equation for the input admittance (Y_{ant}), each mode admittance can be defined from its voltage and current as:

$$V_0 = V_{cpw} + V_{slt} \quad \begin{cases} V_{cpw} = \dfrac{I_0/2}{Y_{cpw}} & \rightarrow \quad Y_{cpw} = \frac{I_0/2}{V_{cpw}} \\ \\ V_{slt} = \dfrac{I_0/2}{Y_{slt}} & \rightarrow \quad Y_{slt} = \frac{I_0/2}{V_{slt}} \end{cases} \tag{4.6}$$

The antenna input admittance is finally computed as:

$$Y_{ant} = \frac{I_0}{V_0} = \frac{I_0}{V_{cpw} + V_{slt}} = \frac{1}{\frac{V_{cpw}}{I_0} + \frac{V_{slt}}{I_0}} = \frac{1}{\frac{1}{2Y_{cpw}} + \frac{1}{2Y_{slt}}} \quad \rightarrow \quad Y_{ant} = \frac{2Y_{cpw}Y_{slt}}{Y_{cpw} + Y_{slt}} \tag{4.7}$$

Transmission line mode: The transmission line mode consists of a CoPlanar Waveguide (CPW) ended in an open-circuit as presented in Fig. 4.6. The CPW is characterized by $\mathrm{w}_{str} = l_{pat}$, g_{ap}=w_{slt} and a total length $l_{cpw} = \lambda_s/4$.

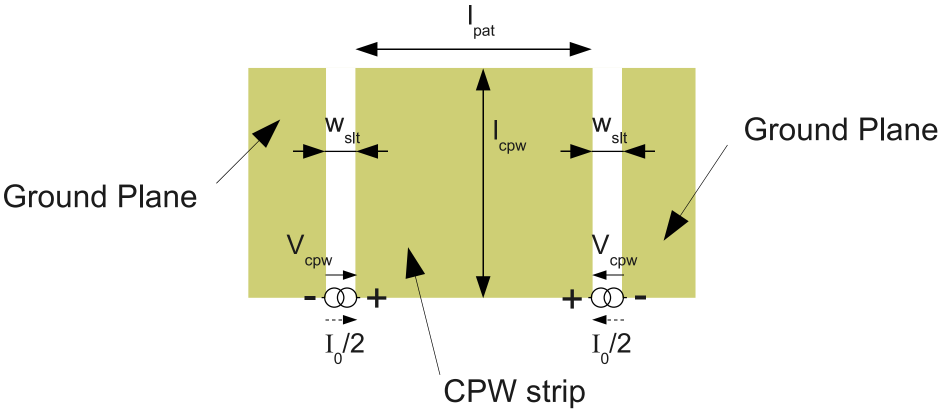

Figure 4.6: Transmission line mode: CoPlanar Waveguide (CPW) ended in an open-circuit

The CPW input admittance (Y_{cpw}) is computed as the inverse of the transmission line input impedance (Z_{cpw}) [46]:

$$Z_{cpw} = Z_0 \frac{Z_L + jZ_0 \tan(\frac{2\pi}{\lambda_s} l_{cpw})}{Z_0 + jZ_L \tan(\frac{2\pi}{\lambda_s} l_{cpw})} \tag{4.8}$$

The CPW characteristic impedance (Z_0) is computed [49] as:

$$Z_0 = \frac{30\pi}{\sqrt{\varepsilon_{eff}}} \frac{K(k_0')}{K(k_0)} \tag{4.9}$$

where ε_{eff} is the effective dielectric constant computed as in equation (3.8) and $K(k_0)$ is the complete elliptic integral of the first kind with module k_0 computed as in equation (3.9).

Radiation mode: The radiation mode consists of two parallel slots with l_{slt}=$\lambda_s/2$, separated by a distance d_{slt}=$\lambda_s/4$ as shown in the slot model at Fig. 4.7. The system can be fepresented by a two-port network where, considering $V_1 = V_2$, it is easy to derive the slot admittance as the sum of the auto-admittance (Y_{11}) and the mutual-admittance (Y_{12}).

$$\left.\begin{aligned} I_1 &= Y_{11}V_1 + Y_{12}V_2 \\ I_2 &= Y_{21}V_1 + Y_{22}V_2 \end{aligned}\right\} \xrightarrow{V_1=V_2} Y_{slt} = \frac{I_1}{V_1} = Y_{11} + Y_{12} \tag{4.10}$$

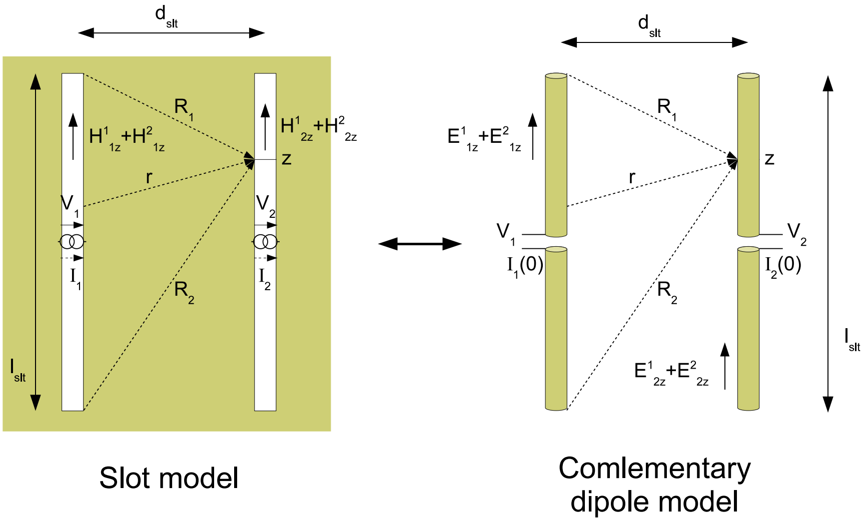

Slot model

Comlementary dipole model

Figure 4.7: Radiation mode: Generated fields on the slots and its complementary dipole model

From Babinet's Principle, in [34] it is demonstrated that a very thin half-wavelength dipole is the complementary structure of the slot. Thus, the admittance of the slot is derived from the complementary dipole impedance as $Y_{slt} = Z_{dip}\frac{4}{\eta^2}$, where $\eta = 120\pi$. Then, the two-slot geometry can be translated into a two dipole situation which has already been solved in [32,34,53]. The configuration is *side-by-side* and it is solved with the induced EMF method. The electrical equivalent radii considered is a_{equ}=0.25w$_{slt}$. The EMF method assumes that the currents $I_1(y)$ and $I_2(y)$ in both antennas are ideal. E^1_{1y} stands for the field in y-axis generated by the antenna 1 onto itself and E^2_{1y} stands for the field in y-axis generated by the antenna 2 onto the antenna 1. The auto- and mutual-impedance are computed as:

$$\begin{aligned} Z_{11} &= \tfrac{-1}{I_1^2(0)} \textstyle\int_1 E^1_{1y} I_1(y) dy \\ Z_{12} &= \tfrac{-1}{I_1(0)I_2(0)} \textstyle\int_1 E^2_{1y} I_2(y) dy \end{aligned} \tag{4.11}$$

As both dipoles are identical, the input currents are equal, being $I_1(0) = I_2(0) = I_m \sin(k_0 l_{slt})$ and $k_0 = \frac{2\pi}{\lambda_0}$. Using the complementarity property, the auto- and mutual-admittance of the slots are computed as:

$$Y_{11} = \frac{j}{\pi\eta\sin(k_0 l_{slt})}\int_{-l_{slt}}^{l_{slt}} \sin(k_0(l_{slt}-|y|))\left(\frac{e^{-jk_0R_1^1}}{R_1^1}+\frac{e^{-jk_0R_2^1}}{R_2^1}-2\cos(k_0 l_{slt})\frac{e^{-jk_0r_1}}{r_1}\right)dy$$

$$Y_{12} = \frac{j}{\pi\eta\sin(k_0 l_{slt})}\int_{-l_{slt}}^{l_{slt}} \sin(k_0(l_{slt}-|y|))\left(\frac{e^{-jk_0R_1^2}}{R_1^2}+\frac{e^{-jk_0R_2^2}}{R_2^2}-2\cos(k_0 l_{slt})\frac{e^{-jk_0r_2}}{r_2}\right)dy \tag{4.12}$$

where

$$\begin{aligned} R_1^1 &= \sqrt{(l_{slt}-y)^2+a_{equ}^2} & R_1^2 &= \sqrt{(l_{slt}-y)^2+(a_{equ}+d_{slt})^2} \\ R_2^1 &= \sqrt{(l_{slt}+y)^2+a_{equ}^2} & R_2^2 &= \sqrt{(l_{slt}+y)^2+(a_{equ}+d_{slt})^2} \\ r_1 &= \sqrt{a_{equ}^2+y^2} & r_2 &= \sqrt{(a_{equ}+d_{slt})^2+y^2} \end{aligned} \tag{4.13}$$

4.2.1.2 Model Validation

The model has been validated comparing the impedance obtained from the model with the impedance obtained from the finite element method. This comparison has been done for a design operating at Ka-band and a designs at V-band. Based on an analogy to microstrip patches designs, w$_{slt}$ has been set to 0.05 λ_s which would represent the dielectric thickness in a microstrip design or what it is the same, the distance between the patch and the ground plane. The Babinet's Principle has been used considering the dipole and the slot surrounded by an uniform dielectric. For that reason, the model considers the CPW rectangular patch antenna in air.

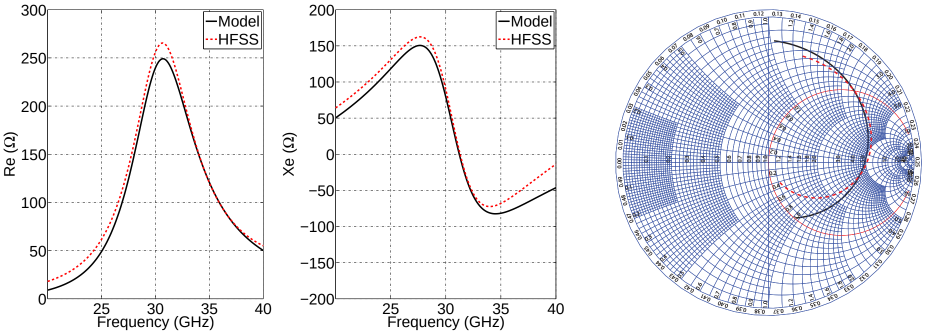

(a) Antenna Impedance (b) Reflection Coefficient

Figure 4.8: Validation of the analytical model with a Ka-band design

Fig. 4.8 and Fig. 4.9 compare the impedance and reflection coefficient at Ka-band and V-band respectively. In Fig. 4.8(a) and Fig. 4.9(a), the real and imaginary parts of the impedance are compared showing similar results using either the analytical model and the finite element method. In both cases the resonant frequency is the same, resulting 30.5GHz and 60GHz for each design. Fig. 4.8(b) and Fig. 4.9(b) illustrates the reflection coefficients in the Smith Chart referred to $Z_0 = 50\Omega$ from 20 to 40 GHz for the Ka-band model and from 50 to 75GHz for the V-band model.

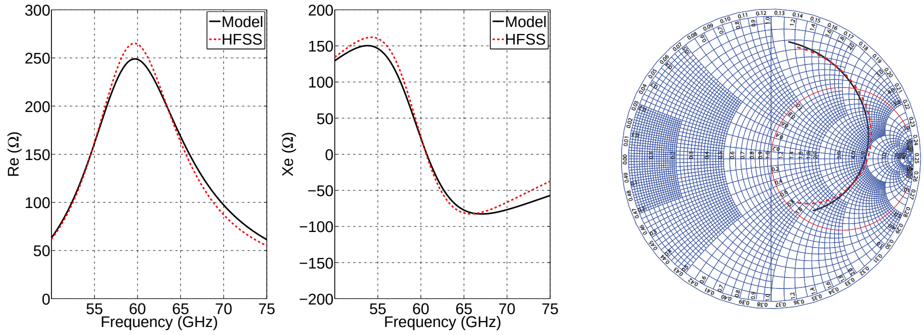

(a) Antenna Impedance (b) Reflection Coefficient

Figure 4.9: Validation of the analytical model with a V-band design

4.2.1.3 Linear Polarization Prototype

Starting from the analytical model previously presented, two linear polarization CPW Patch antenna prototypes printed on gold on a $500\mu m$ thick synthetic quartz glass have been designed with the finite elements method. One of the prototypes operates at Ka-band and the other operates at V-band. The resonant frequency for the different designs has been chosen slightly below the desired center frequency. This is because the excited linear mode will correspond to the lower frequency mode used to obtain circular polarization [50]. The antenna is fed inductively with a narrow strip. The parameters dimensions for each prototype are summarized in Table 4.1

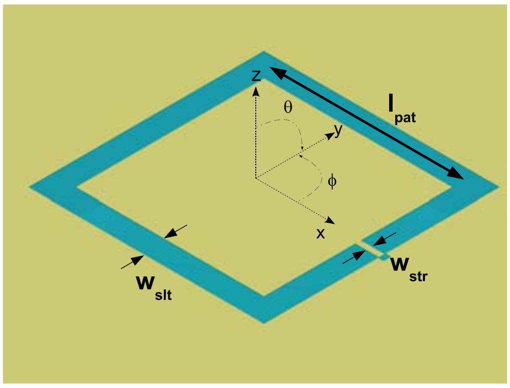

Figure 4.10: LP CPW Patch Antenna

Table 4.1: LP Antenna Parameters

Parameter	Ka-band	V-band
l_{pat}	0.220 λ_s	0.220 λ_s
w_{slt}	0.028 λ_s	0.029 λ_s
h_{die}	0.064 λ_s	0.137 λ_s
w_{str}	0.008 λ_s	0.005 λ_s

Ka-band: The field distribution of the linearly polarized CPW Patch antenna at 30GHz is illustrated in Fig. 4.11(a). The antenna E-plane, containing the electric field vector and the direction of maximum radiation, corresponds to the xz-plane ($\phi = 0^o$) and the H-plane, containing the magnetic field vector and the direction of maximum radiation, corresponds to the yz-plane ($\phi = 90^o$). Fig.4.11(b) shows the real and imaginary part of the simulated antenna impedance, where a high resistance of 320Ω can be observed at the resonant frequency. This frequency, denoted by having an impedance imaginary part equal to zero, has been set slightly lower than the center frequency as mentioned previously.

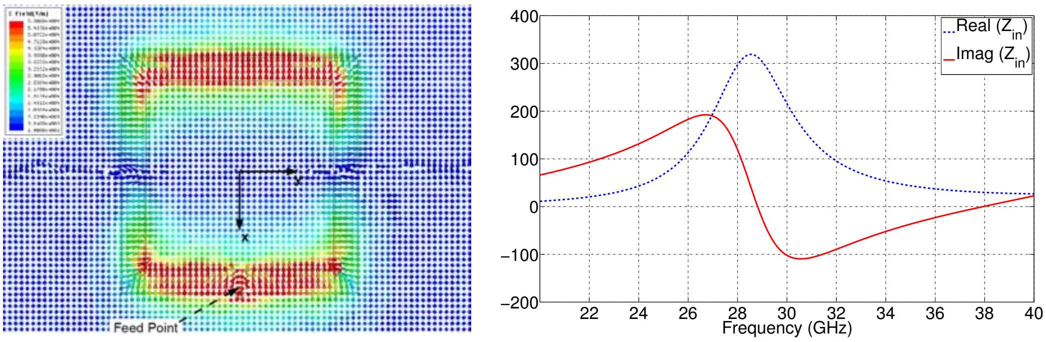

(a) Field Distribution at 30GHz (b) Input Impedance

Figure 4.11: Ka-band linearly polarized prototype field distribution and input impedance

Fig. 4.12(a) illustrates the radiation pattern for E- and H-plane at 30GHz, where a Half-Power Beamwidth (HPBW) of 60° is observed. Fig. 4.12(b) shows the antenna gain versus frequency for the two directions of maximum radiation. It can be seen a gain variation between the two main lobes of 1dB, resulting greater in the direction of $\theta = 180^o$. This is due to the existence of the dielectric which implies a level of confined fields in the dielectric side higher than in the air side. It can also be observed that the gain at $\theta = 0^o$ is more flatter than the one at $\theta = 180^o$.

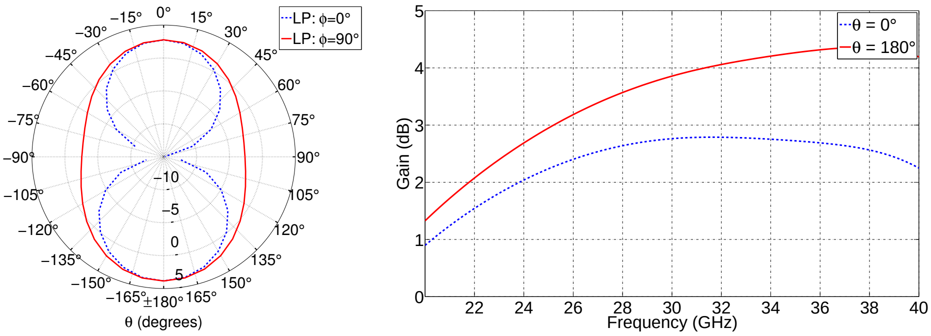

(a) Radiation Pattern at 30GHz (b) Gain vs Frequency

Figure 4.12: Ka-band linearly polarized prototype radiation pattern and antenna gain

V-band: Fig. 4.13(a) illustrates the field distribution at 60GHz for the linearly polarized CPW Patch antenna operating at V-band. Fig. 4.13(b) shows the simulated antenna input impedance with the resonant frequency below 60GHz, as desired.

Fig. 4.14(a) shows the antenna radiation pattern for E- and H-planes at 60GHz, with a HPBW of 80°. In Fig. 4.14(b), it is observed that the gain at $\theta = 180^o$ is 4dB higher than at $\theta = 0^o$. Compared to the 30GHz prototype, the 500μm dielectric is electrically thicker. This is translated into a density of radiated field confined into the dielectric side much higher at V-band than at Ka-band.

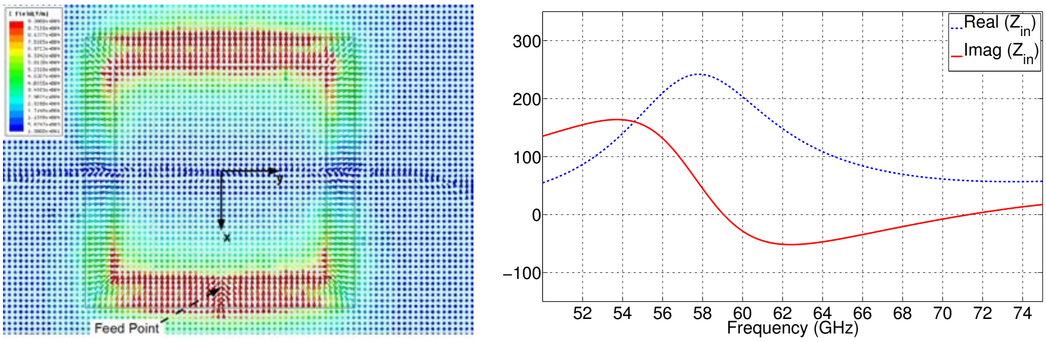

(a) Field Distribution at 60GHz

(b) Input Impedance

Figure 4.13: V-band linearly polarized prototype field distribution and input impedance

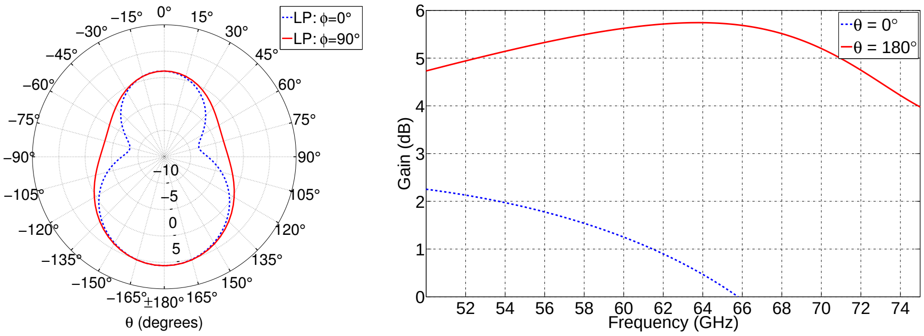

(a) Radiation Pattern at 60GHz

(b) Gain vs Frequency

Figure 4.14: V-band linearly polarized prototype radiation pattern and antenna gain

4.2.2 Circular Polarization CPW Patch Antenna

Circular Polarization (CP) is obtained by inducing two orthogonal modes with equal amplitude and quadrature phase. The technique used in this case consists of cutting two pair of opposite corners providing the necessary perturbation to obtain the two modes (Fig. 4.15). Depending which pair of corners are truncated, the CP resulting will be right-handed (RHCP) or left-handed (LHCP). Starting from the linearly polarized CPW Patch antenna structures perviously presented, two prototypes at Ka-band and V-band have been designed. The amount of perturbation necessary to obtain a good CP has been obtained empirically with the finite elements method simulator Ansoft HFSS. Because antenna symmetry in x-axis, the results for RHCP and LHCP configurations are equivalent, named both as CP configuration. The parameters dimensions for each prototype are summarized in Table 4.2

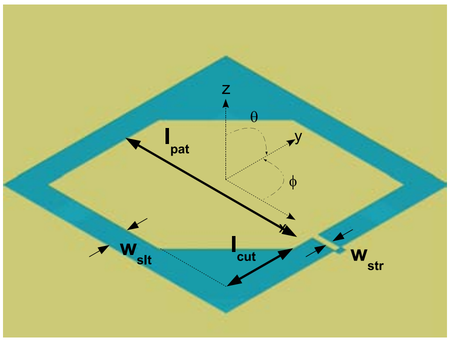

Figure 4.15: CP CPW Patch Antenna

Table 4.2: CP Antenna Parameters

Parameter	Ka-band	V-band
l_{pat}	0.220 λ_s	0.220 λ_s
w_{slt}	0.028 λ_s	0.0029 λ_s
l_{cut}	0.083 λ_s	0.111 λ_s
h_{die}	0.064 λ_s	0.137 λ_s
w_{str}	0.008 λ_s	0.005 λ_s

Ka-band: The field distribution for the circularly polarized CPW Patch antenna design at 30GHz is presented in Fig. 4.16(a) and Fig. 4.16(b). The field is observed in two different phase instants with a difference of 90^{o}, being in one instant horizontal and in the other vertical. This time variation of the radiated field illustrates clearly the circular behavior of the antenna polarization which has to be corroborated by computing the axial ratio. Fig. 4.17 illustrates the simulated antenna input impedance. The two resonant modes, at 28GHz and 32GHz, are denoted by a maximum in the resistance, matching the lowest frequency with the linear polarization design resonant frequency. At 30.5GHz, both resonant modes have the same amplitude, being denoted with an inflection point in the real part of the impedance. It is at this frequency where the Circular Polarization is expected to be more pure and therefore the axial ratio to be minimum as long as the two resonant modes are quadrature phase.

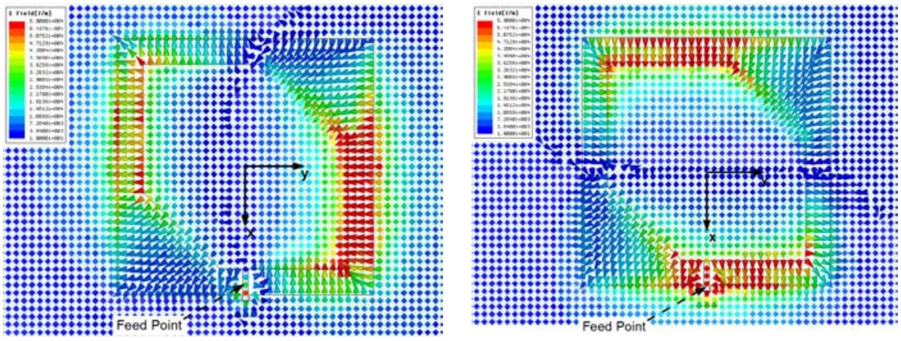

(a) 30GHz horizontal field distribution instant

(b) 30GHz vertical field distribution instant

Figure 4.16: Ka-band circularly polarized prototype field distribution

Concerning the radiation pattern, in Fig. 4.18(a) can be seen that the radiation field is similar for the xz-plane ($\phi = 0^{o}$) and yz-plane ($\phi = 90^{o}$), with a HPBW of 80^{o}. Similar to the linearly polarized design, due to the existence of dielectric in one side of the antenna, there is a higher density of confined fields in the substrate side ($\theta = 180^{o}$) which is translated into a gain difference between the two main directions lobes. This difference, as illustrated in Fig. 4.18(b), is 1dB at the center frequency and increases with the frequency. The gain as a function of frequency is flatter in

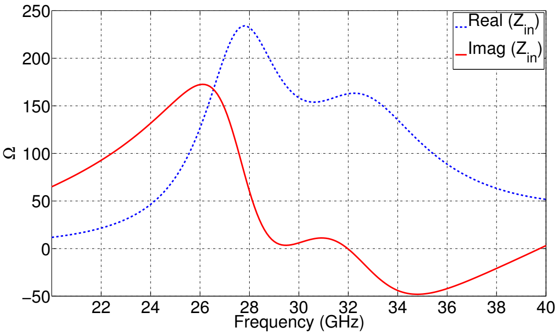

Figure 4.17: Ka-band circularly polarized prototype input impedance

$\theta = 0^o$ than in $\theta = 180^o$.

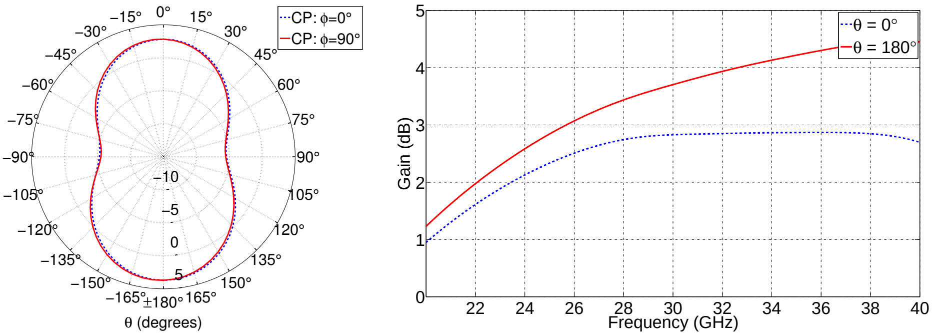

(a) Radiation Pattern at 30GHz (b) Gain (dB) at $\phi = 0$

Figure 4.18: Ka-band circularly polarized prototype radiation pattern and antenna gain

Fig. 4.19(a) illustrates the computed axial ratio versus frequency, showing a 3dB axial ratio frequency bandwidth of 6.5% centered at 30.5GHz. Fig. 4.19(b) shows the computed axial ratio versus θ at yz-plane. It has been computed for the center frequency (30.5GHz), and the upper (31.5GHz) and lower (29.6GHz) frequencies that define the 3dB axial ratio frequency bandwidth. The 3dB axial ratio beamwidth at the center frequency is 70^o for the $\theta = 0^o$ beam and 90^o for $\theta = 180^o$ beam. The 3dB beamwidth values do not remain constant for each frequency, being maximum for the lower frequency and almost null for the upper frequency.

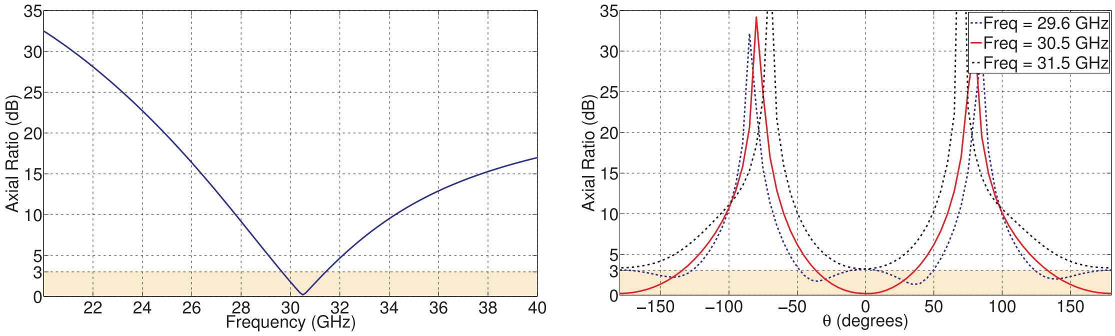

(a) Axial ratio versus frequency (b) Axial ratio versus Theta

Figure 4.19: Ka-band circularly polarized prototype axial ratio

V-band: Similarly to Ka-band, two 90° different phase instants of the field distribution at 60GHz for the V-band circular polarized antenna design are shown in Fig. 4.20(a) and Fig. 4.20(b), denoting again the circular behavior of the antenna polarization. The simulated antenna input impedance is shown in Fig. 4.21. The resistance inflection point at 62GHz indicates the frequency where the axial ratio should be minimum.

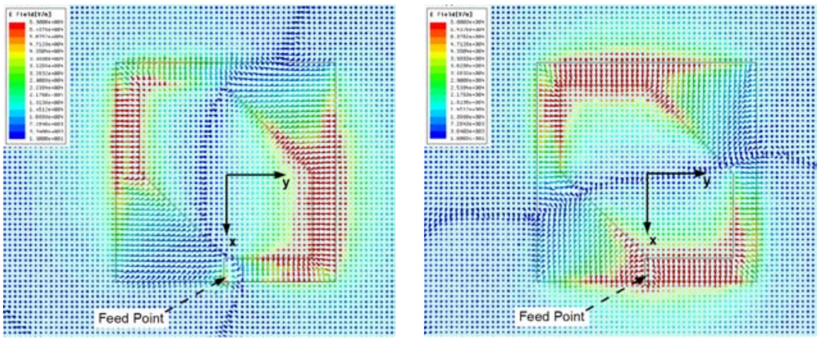

(a) 60GHz horizontal field distribution instant (b) 60GHz vertical field distribution instant

Figure 4.20: V-band circularly polarized prototype field distribution

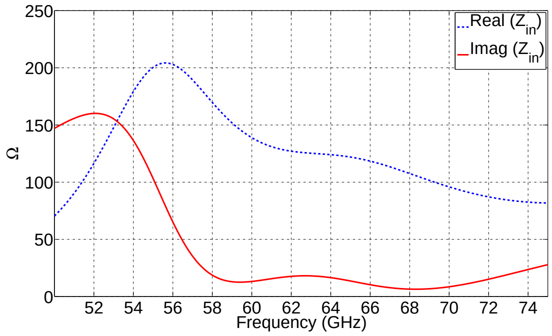

Figure 4.21: V-band circularly polarized prototype input impedance

The substrate electrical thickness for the V-band design has increased from the Ka-band design, resulting into an increase of the confined fields in the dielectric side of the antenna. Similar to the linearly polarized antenna at this frequency band, the gain at $\theta = 180^\circ$ is higher than the gain at $\theta = 0^\circ$ with a 5dB difference. Fig. 4.22(a) illustrates the radiation pattern for the xz-plane ($\phi = 0^\circ$) and yz-plane ($\phi = 90^\circ$). Fig. 4.22(b) shows the gain versus frequency. It can be seen how the gain remains flat at the V-band for the $\theta = 180^\circ$ direction while decreases fast for the $\theta = 0^\circ$ direction.

The computed axial ratio is presented in Fig. 4.23(a), showing a 3dB axial ratio bandwidth of 6.5% centered at 62GHz. The axial ratio versus θ at the yz-plane is shown in Fig. 4.23(b) for the center frequency, and the upper (64GHz) and lower (60GHz) frequencies that define the 3dB axial ratio bandwidth. The 3dB axial ratio beamwidth at the center frequency is 70° for the $\theta = 0^\circ$ beam and 200° for the $\theta = 180^\circ$ beam. For all the frequencies included in the 3dB axial ratio bandwidth, the axial ratio beamwidth for the $\theta = 180^\circ$ beam is wider than 90°.

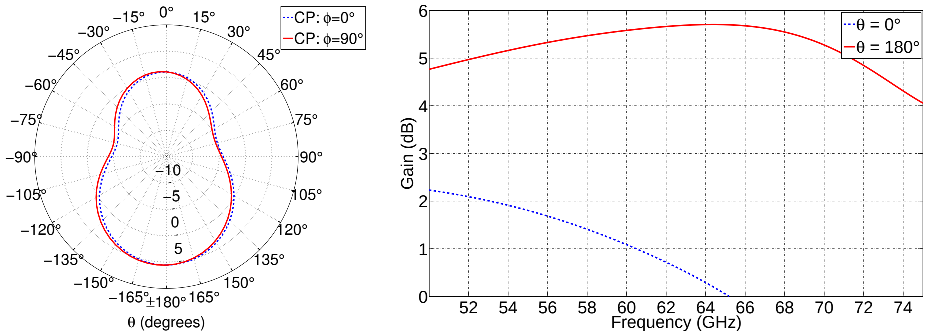

(a) Radiation Pattern at 60GHz

(b) Gain (dB) at $\phi = 0$

Figure 4.22: V-band circularly polarized prototype radiation pattern and antenna gain

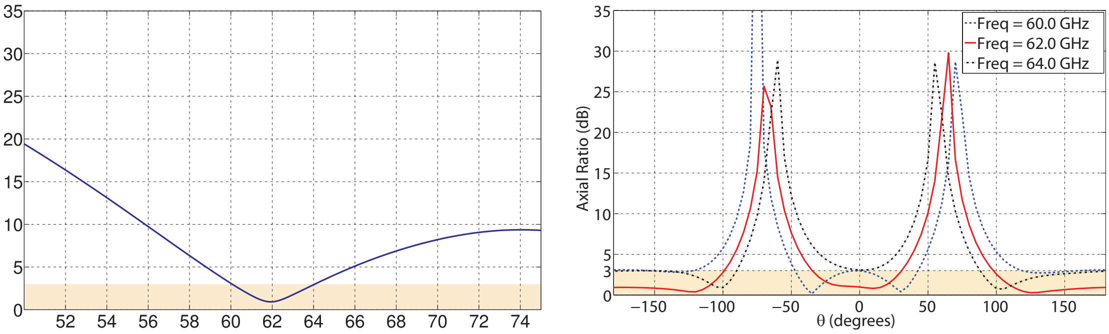

(a) Axial Ratio versus frequency

(b) Axial Ratio versus Theta

Figure 4.23: V-band circularly polarized prototype axial ratio

4.2.3 Polarization Reconfigurable CPW Patch Antenna

The previous linear and circular polarization designs have been combined to obtain the final reconfigurable antenna already presented in Fig. 4.3. The resulting corner-truncated square coplanar patch antenna has four small parasitic conductors of triangular shape that are connected to the patch by RF-MEMS switches. The polarization reconfiguration is being done by activating/deactivating the set of RF-MEMS switches as presented in Table 4.3, being able to switch between Vertical Linear Polarization (VLP), Left-Handed Circular Polarization (LHCP) and Right-Handed Circular Polarization (RHCP). This technique is well known and has been used in other frequencies and antenna structures [54].

Polarization	MEMS-1	MEMS-2	MEMS-3	MEMS-4
VLP	ON	ON	ON	ON
	OFF	OFF	OFF	OFF
RHCP	ON	ON	OFF	OFF
LHCP	OFF	OFF	ON	ON

Table 4.3: RF-MEMS Switch Configuration

Two prototypes have been designed, first a Hard-Wire (HW) geometry to test the polarization properties, and then the reconfigurable version.

4.2.3.1 Hard-Wire Reconfigurable CPW Patch antenna

As an initial attempt to proof the reconfigurability concept, the RF-MEMS switches have been replaced by a short-circuit when ON and by an open-circuit when OFF (Fig. 4.24), leading to a solution named *Hard-Wire (HW) reconfigurable antenna.* This antenna is fed by a CoPlanar Waveguide (CPW), with a lambda quarter transformer to obtain an input impedance of 50Ω.

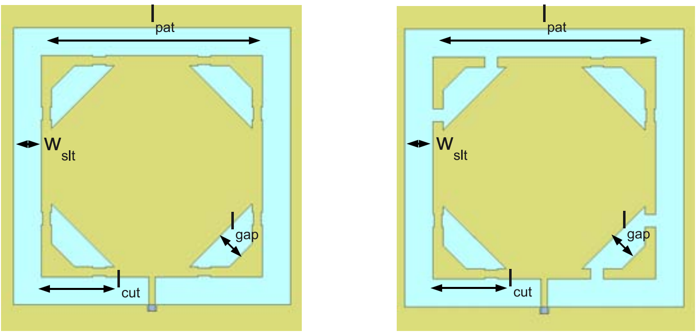

(a) Linear Polarization (b) Circular Polarization

Figure 4.24: Hard-Wire (HW) configurations

Two designs of HW reconfigurable CPW Patch antenna have been done, at Ka-band and at V-band. Table 4.4 summarizes the parameters dimensions for the Ka-band and V-band prototypes. Differences are due to the difference effective permittivity (ε_{eff}) produced by the different electric thickness of the dielectric substrate.

Parameter	Ka-band	V-band
l_{pat}	$0.220\ \lambda_s$	$0.220\ \lambda_s$
w_{slt}	$0.028\ \lambda_s$	$0.0029\ \lambda_s$
l_{cut}	$0.083\ \lambda_s$	$0.111\ \lambda_s$
l_{gap}	$0.028\ \lambda_s$	$0.034\ \lambda_s$
w_{str}	$0.008\ \lambda_s$	$0.005\ \lambda_s$
g_{ap}	$0.009\ \lambda_s$	$0.018\ \lambda_s$
h_{die}	$0.064\ \lambda_s$	$0.137\ \lambda_s$

Table 4.4: HW CPW Patch Antenna Parameters

Ka-band: Fig. 4.25(a) shows the input impedance for the antenna configured in linear and circular polarization. It can be clearly seen how the linear configuration has only one resonant mode while the circular configuration have two, with one of them equal to the linear case. Concerning the antenna resonant frequency, denoted by the imaginary part of the impedance being equal to zero, there is a slightly frequency shift and a resistance difference between both configurations. This may bring some difficulties to have a good impedance matching in both designs using the same feed network. In Fig. 4.25(b) it can be seen how the impedance has been matched for the circular polarization configuration, with a -10dB return loss frequency bandwidth of 16%. The antenna configured in linear polarization is not so good impedance matched, having a frequency bandwidth related to -10dB return loss of 3%. Under the assumption made in many mobile communication systems that a return loss of -6dB is considered a good threshold to have the antenna matched, the linearly polarized configuration has a frequency bandwidth related to -6dB return loss of 14% and the circularly polarized has a bandwidth of 25%.

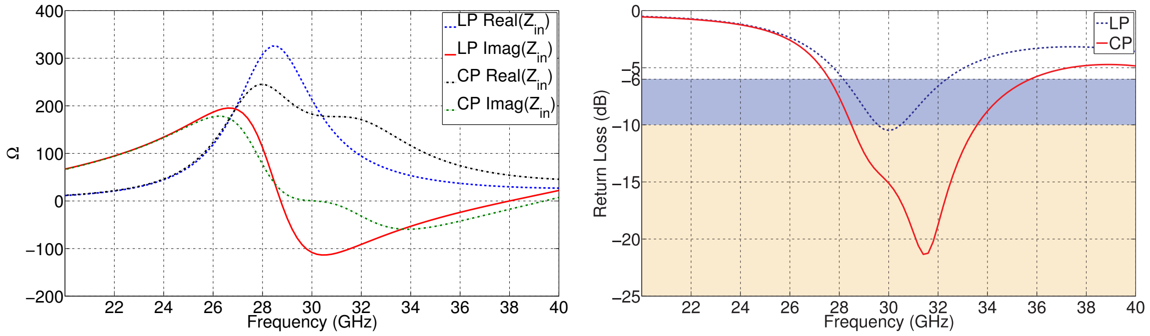

(a) Input Impedance (b) Return Loss (dB)

Figure 4.25: Ka-band HW prototype field distribution and input impedance

In Fig.4.26(a) it is shown the antenna radiation pattern when configured in linear and circular polarization. Both antennas have a HPBW of 70°. Fig. 4.26(b) illustrates the gain versus frequency for $\theta = 0^o$ and $\theta = 180^o$. The expected 1 dB gain difference between both directions it is observed at center frequency.

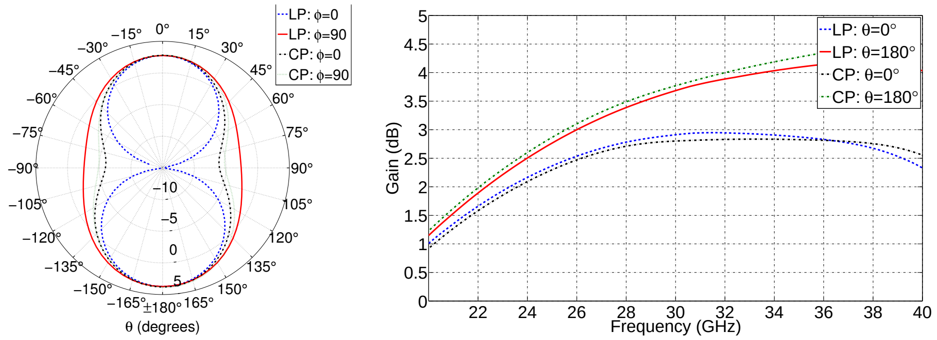

(a) Radiation Pattern at 30GHz (b) Gain (dB) at $\phi = 0$

Figure 4.26: Ka-band HW prototype radiation pattern and antenna gain

Concerning the axial ratio of the antenna when configured in circular polarization, Fig. 4.27 shows a 3dB axial ratio bandwidth of 5% at the maximum radiation direction. The HW CPW Patch antenna presents in Fig. 4.27(b) a 3dB axial ratio beamwidth of 90° at the center frequency for the $\theta = 0^o$ beam and a beamwidth of 120^o for the $\theta = 180^o$ beam.

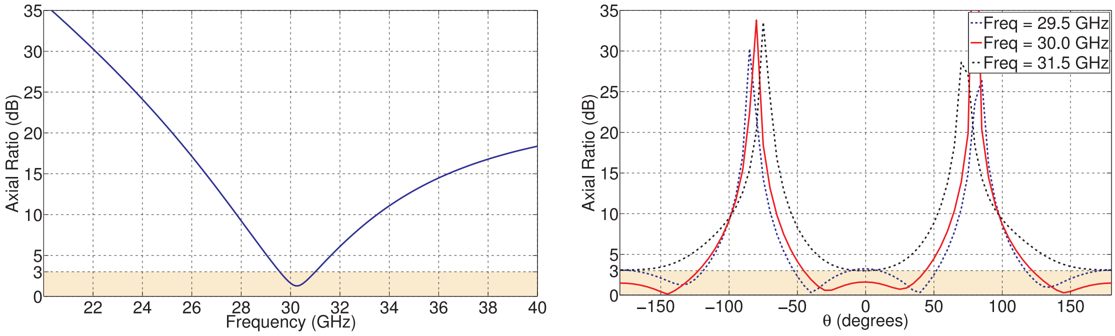

(a) Axial Ratio versus frequency

(b) Axial Ratio versus Theta

Figure 4.27: Ka-band HW prototype axial ratio

V-band: The input impedance of the HW CPW Patch antenna operating at V-band is presented in Fig. 4.28(a) for the antenna configured in linear and circular polarization. It can be seen that due to the influence of an electrically thicker substrate, this design has a lower resistance than the design at Ka-band. This lower impedance facilitates the antenna matching. Fig. 4.28(b) shows the return loss for both configurations, where a 16% and a 30% frequency bandwidth are observed for LP and CP respectively.

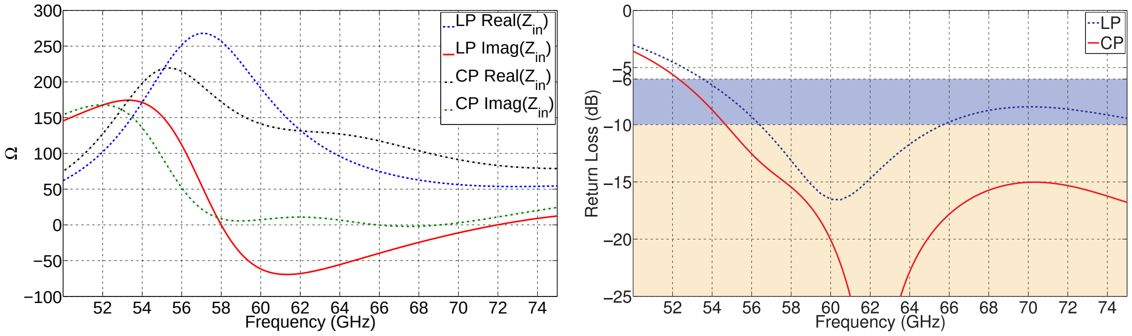

(a) Input Impedance

(b) Return Loss (dB)

Figure 4.28: V-band HW prototype field distribution and input impedance

The radiation patterns are similar than the ones obtained for each polarization case separately. Fig. 4.29(a) shows the pattern for both configurations in xz- and yz-planes. The HPBW in all the cases is 86^o. Like happened in non-reconfigurable V-band designs presented previously, the radiated fields are confined with higher density in the dielectric side of the antenna and therefore the radiation gain has a 4dB difference at the center frequency between $\theta = 0^o$ and $\theta = 180^o$. Fig. 4.29(b) shows the antenna gain versus frequency, being flatter at $\theta = 180^o$ direction.

Fig. 4.30(a) illustrates the simulated axial ratio when configured in circular polarization. A 3dB axial ratio frequency bandwidth of 6.4% is observed. From Fig. 4.30(b), the 3dB axial ratio beamwidth at the center frequency is 70^o for the $\theta = 0^o$ beam and 160^o for the $\theta = 180^o$ beam. The

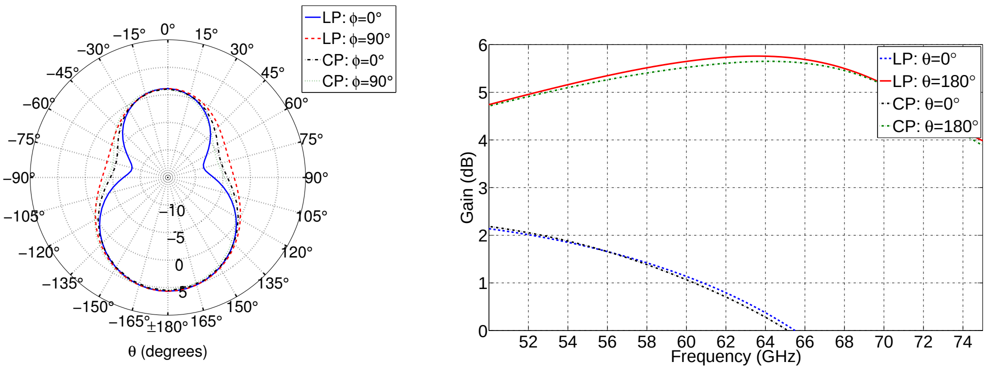

(a) Radiation Pattern at 60GHz (b) Gain (dB) at $\phi = 0$

Figure 4.29: V-band HW prototype radiation pattern and antenna gain

antenna 3dB axial ratio beamwidth changes for each frequency, being minimum for the bandwidth upper frequency and maximum for the bandwidth lower frequency.

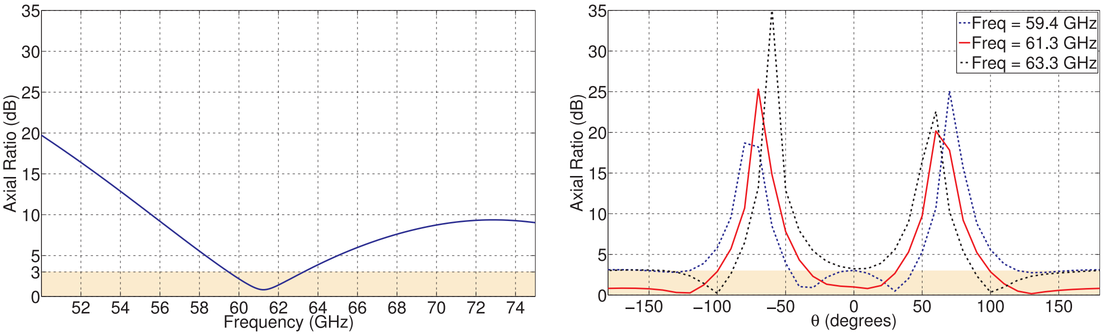

(a) Axial Ratio versus frequency (b) Axial Ratio versus Theta

Figure 4.30: V-band HW prototype axial ratio

Reconfigurability Validation: As a previous step before designing and manufacturing the RF-MEMS-integrated reconfigurable antenna, the Ka-band HW CPW Patch antenna prototype has been manufactured by laser technology. The antenna consists of copper printed on teflon-based Arlon CLTE-XT with a relative permittivity (ε_r) of 2.94 and a loss tangent of 0.0012 (characterized at 10GHz). The antenna has been manufactured in VLP, RHCP and LHCP as shown in Fig. 4.31.

The reflection coefficient and the axial ratio (Fig. 4.32) have been measured. The antenna presents a -6dB return loss frequency bandwidth of 13% when configured in LP and 17% when configured in CP. Concerning the axial ratio, the two circular polarization configurations present a 3dB axial ratio frequency bandwidth of 1.7%. These results validate the HW model, leading to design the microfabricated switch-integrated reconfigurable antenna.

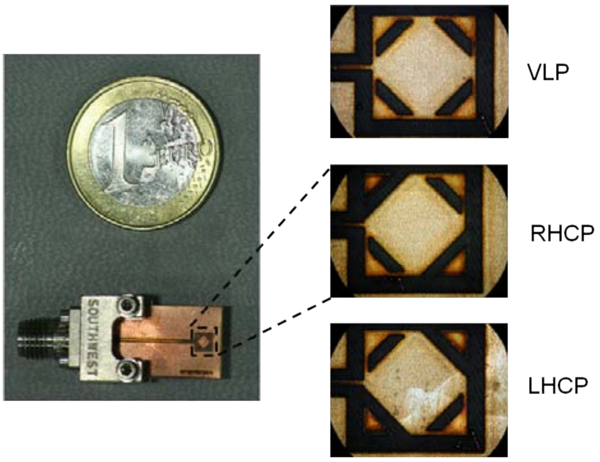

Figure 4.31: Ka-band HW prototypes printed on Arlon CLTE-XT

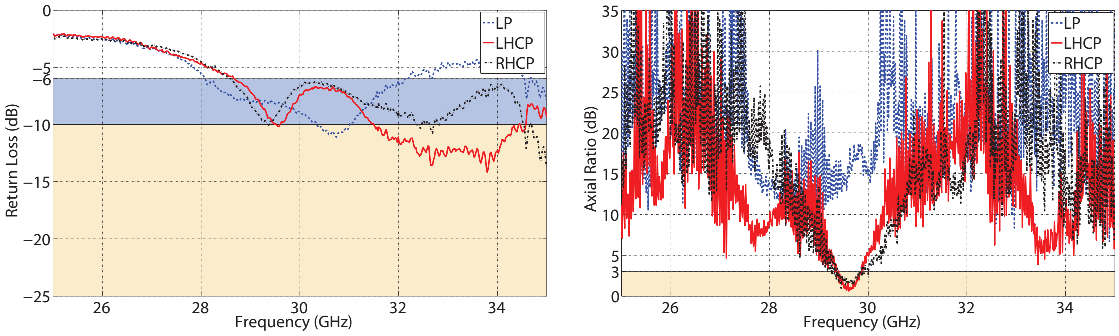

(a) Return Loss (dB)

(b) Axial Ratio versus Frequency

Figure 4.32: Ka-band HW prototypes measurements

4.2.3.2 RF-MEMS switches Reconfigurable CPW Patch antenna

A final design of the polarization reconfigurable CPW Patch antenna (Fig. 4.33) has been done by adding the 3D model of the RF-MEMS switch and it has been simulated with the finite elements method. Because the dimensions of the RF-MEMS switch and its low isolation at high frequencies, the prototype has only been designed to operate at Ka-band. The design also includes the final air-bridges that will be used in the CoPlanar Waveguide to avoid the excitation of the odd-modes and that will be fabricated using the RF-MEMS switch fabrication process. The antenna parameters have been optimized to compensate parasitic capacitances from the switches when are in OFF state. Table 4.5 summarizes the parameters dimensions.

Fig. 4.34(a) illustrates the antenna input impedance for the LP and CP configurations. Fig. 4.34(b) shows the return loss of the antenna with the matching network designed with the CPW circuital model in Agilent ADS simulator. The difficulty to match both configurations for the same frequency has been increased with the air-bridges capacitance influencing the impedance. Focusing in the CP configuration, it can be seen that the frequency bandwidth related to a -10 dB return loss is 11% while if the return loss threshold considered is -6dB, the bandwidth increases up to 30%. The LP is not so well matched by the impedance transformer and it has a frequency bandwidth

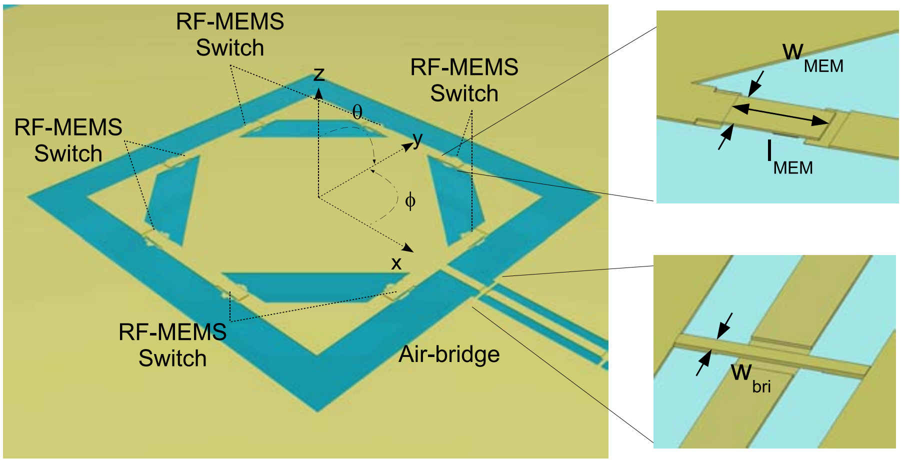

Figure 4.33: RF-MEMS integrated CPW Patch Antenna (switch and bridge details)

related to -6dB return loss of 9%.

Parameter	Ka-band (in λ_s)
l_{slt}	0.276
l_{pat}	0.220
w_{slt}	0.028
l_{cut}	0.083
h_{die}	0.064
w_{bri}	0.002
l_{MEM}	0.015
w_{MEM}	0.008
w_{str}	0.008
g_{ap}	0.009

Table 4.5: RF-MEMS integrated CPW Patch Antenna Parameters

Fig. 4.35(a) shows the radiation pattern in xz- and yz-planes for LP and CP configurations. Both designs have a HPBW of 70°. Fig. 4.35(b) illustrates the antenna gain versus frequency for both antenna configurations at $\theta = 0^o$ and $\theta = 180^o$ directions.

When the RF-MEMS switches are set to configure the antenna polarization circular, the minimum simulated axial ratio is 0.5dB at 30.4GHz as shown in Fig. 4.36(a). It can be observed a 3dB axial ratio frequency bandwidth of 5.25%. Fig. 4.36(b) illustrates the axial ratio versus the radiation angle (θ). It can be seen that the 3dB axial ratio beamwidth is different for each frequency, being maximum for the bandwidth lower frequency and minimum for the bandwidth upper frequency. At the center frequency, the 3dB axial ratio beamwidth is 80° for the $\theta = 0^o$ beam and 100° for $\theta = 180^o$ beam.

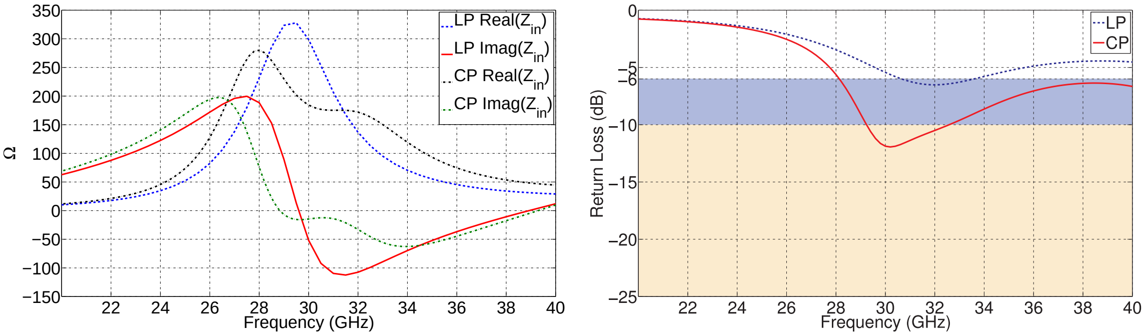

(a) Input Impedance (b) Return Loss (dB)

Figure 4.34: Ka-band reconfigurable polarization prototype field distribution and input impedance

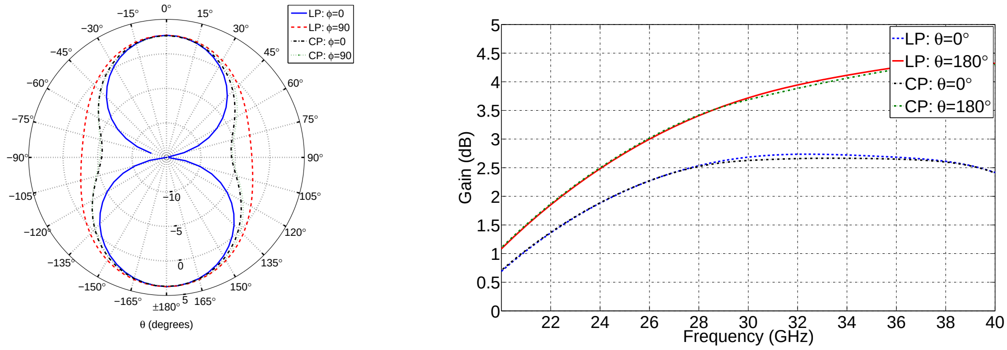

(a) Radiation Pattern at 30GHz (b) Gain (dB) at $\phi = 0$

Figure 4.35: Ka-band reconfigurable polarization prototype radiation pattern and antenna gain

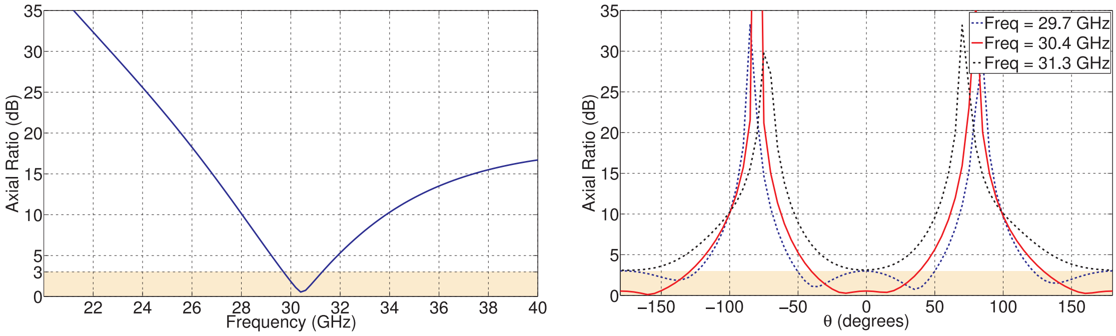

(a) Axial Ratio versus frequency (b) Axial Ratio versus Theta

Figure 4.36: Ka-band reconfigurable polarization prototype axial ratio

4.3 4-Qdime Antenna

The 4-Qdime antenna results from the need to have a reconfigurable antenna with a 3dB axial ratio frequency bandwidth wider than the previous CPW Patch antenna. The antenna architecture proposed in Fig. 4.37 consists of four radiating elements (Qdime antenna) placed in a 2×2 grid and successively rotated 90^o one from the other. Depending on each element feeding phase, the antenna polarization may be switched between Vertical Linear Polarization (VLP), Horizontal Linear Polarization (HLP), Left-Handed Circular Polarization (LHCP) or Right-Handed Circular Polarization (RHCP).

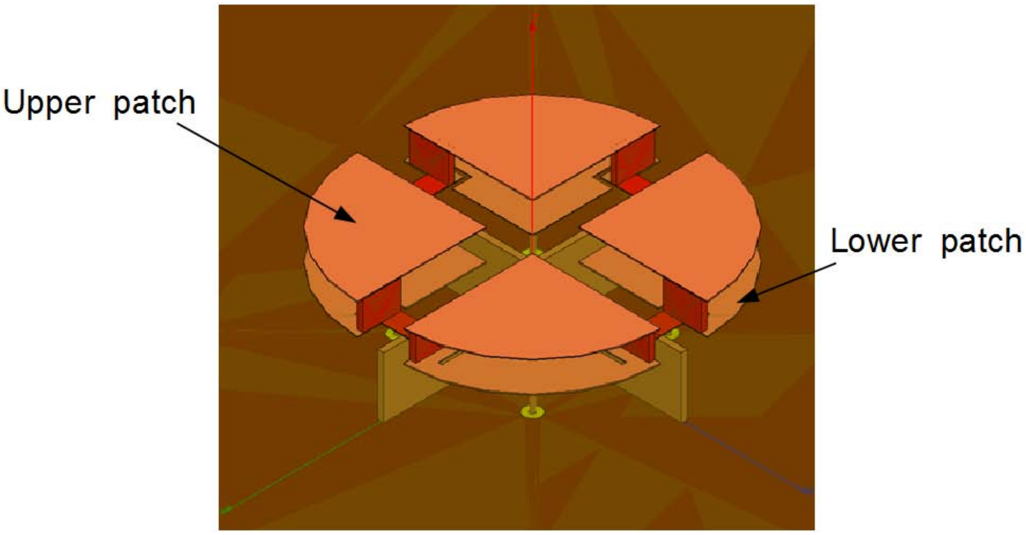

Figure 4.37: 4-Qdime Antenna

4.3.1 Qdime Antenna

The Qdime antenna [55] is characterized by its multilayer structure formed by 3 metallic layers (*upper patch*, *lower patch* and *ground plane*) printed on two dielectric substrates of thickness h_{upp} and h_{low}. Fig.4.38 illustrates the top view of the lower and the upper patches. Circular geometry is used to optimize the volumetric modal distribution in accordance with the minimum radiation Q attainable and the shorting walls technique is used to reduce the antenna dimensions. Each patch resonates to a different frequency, with the capacity to have a dual-band or a single broad-band antenna. The work in this thesis is focused in the design of a single broad-band integrated Qdime antenna, which means that the upper and lower resonant frequencies will be close. Each substrate thickness fix the bandwidth related to each resonant frequency.

The upper and lower slot length (S_{upp} and S_{low}) have to be approximated half wavelength of the resonant frequencies (f_{upp} and f_{low}). The slot lengths are computed as the patch arch perimeter (S_{pat}) plus twice the distance from the patch edge to the shorting wall (l_{upp} and l_{low}).

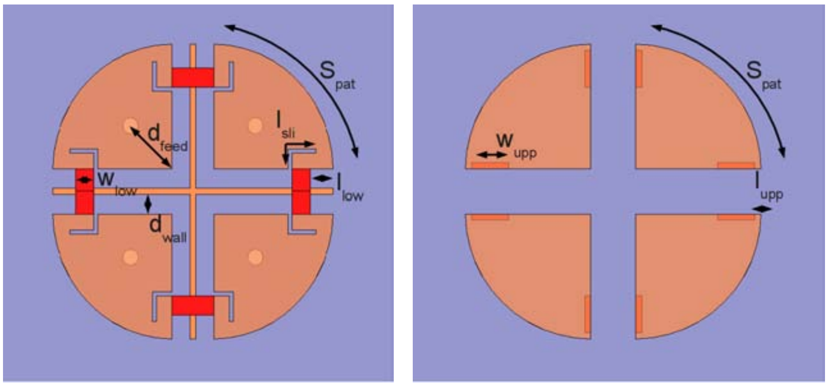

(a) Lower Patch (b) Upper Patch

Figure 4.38: Top views of the 4-Qdime lower and upper patches

$$\begin{aligned} S_{upp} &= S_{pat} + 2l_{upp} \Longrightarrow \quad S_{upp} \approx \frac{\lambda_{upp}}{2} \\ S_{low} &= S_{pat} + 2l_{low} \Longrightarrow \quad S_{low} \approx \frac{\lambda_{low}}{2} \end{aligned} \tag{4.14}$$

An initial design with air as dielectric ($\varepsilon_r = 1$) operating at V-band has been done. Fig. 4.39(a) shows the imaginary part of the input impedance, illustrating how variations in l_{low} are translated into variations of the lower resonant frequency f_{low}. The same effect happens with l_{upp}, where its variations are related to the upper resonant frequency f_{upp}, as seen in Fig. 4.39(b)

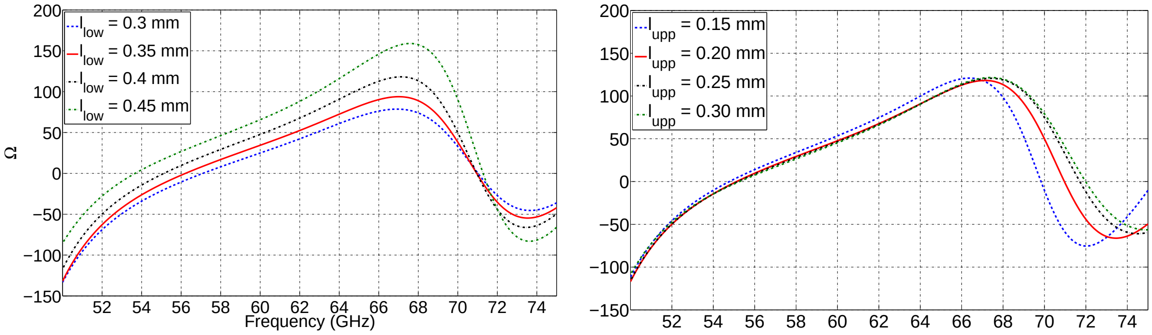

(a) l_{low} tunning (b) l_{upp} tunning

Figure 4.39: Qdime input impedance imaginary part for different l_{low} and l_{upp}

A slit in the lower patch, of length l_{sli}, is etched to increase the electrical path from the feeding point to the ground plane, obtaining a better impedance matching. Fig. 4.40(a) illustrates the effect of the slit on the impedance matching for the antenna designed. The width of the shorting walls are also used to tune the input admittance. The antenna is fed by a coaxial probe. The position of the feed point is chosen in order to have an input resistance of 50Ω. Fig. 4.40(b) shows the input resistance for different coaxial probe positions from the corner.

Fig. 4.41 represents the simulated return loss for the initial Qdime antenna designed. A -10dB return loss frequency bandwidth of 22% is observed. The Qdime with air as dielectric is not possible to be manufactured, but gives the necessary information to understand its behavior without the

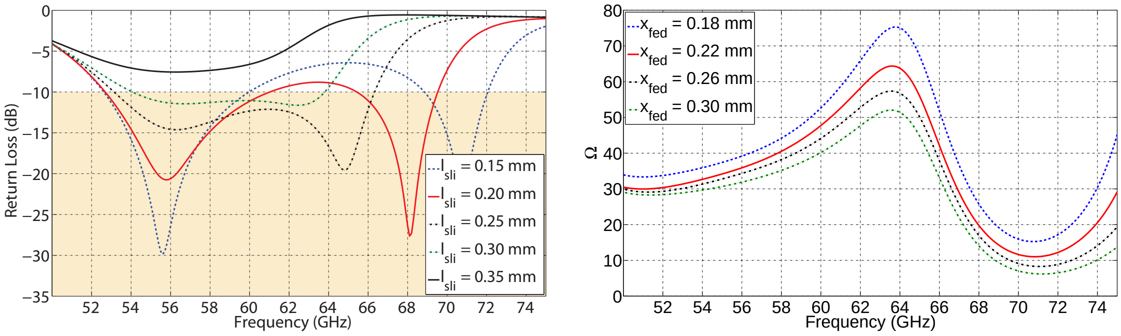

(a) l_{sli} tunning (b) x_{fed} tunning

Figure 4.40: Qdime Return Loss and impedance real part for different l_{sli} and x_{fed}

influence of the dielectric effects.

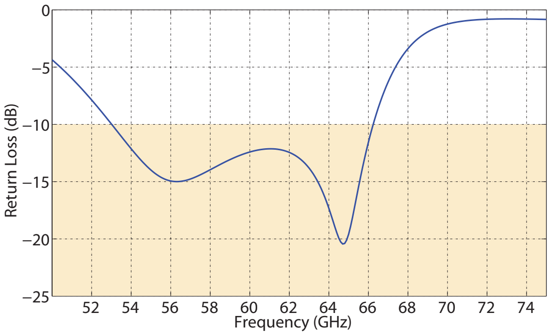

Figure 4.41: Qdime Return Loss with air as dielectric

4.3.2 4-Qdime

A set of four Qdime elements are arranged in a 2×2 square grid, rotated 90° one from each other as shown in Fig. 4.42. A ground metal wall between elements is used to reduce the mutual coupling. This lineal polarized elements arrangement may be used to generate CP just by applying the appropriate current phase at each element port [56]. Table 4.6 summarizes the required phases to achieve Horizontal Linear Polarization (HLP), Vertical Linear Polarization (VLP), Left-Handed Circular Polarization (LHCP) and Right-Handed Circular Polarization (RHCP).

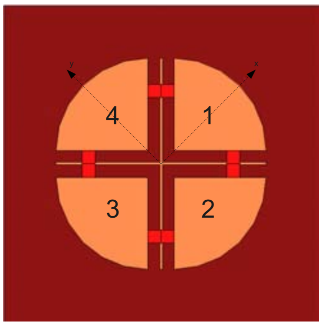

Figure 4.42: 4-Qdime 2 × 2 square grid elements

Table 4.6: Elements phase difference

Qdime element	HLP	VLP	RHCP	LHCP
1	0°	0°	0°	0°
2	0°	180°	270°	90°
3	180°	180°	180°	180°
4	180°	0°	90°	270°

The reconfigurable feed network topology in Fig. 4.43 has been proposed to feed the 4-Qdime. It consists of a 180-degree Hybrid (*Rat-race*) [46] connected to two Quadrature (90°) Hybrids [46]. The ports phase reconfigurability of this antenna is obtained by switching two RF-MEMS switches that connect the Rat-race with the different input ports of the Quadrature Hybrids. Depending the switches state, the ports will have a different phase and then the antenna will be configured in one of the possible polarizations: RHCP, LHCP or HLP. The VLP case can not be obtained with this topology as seen in Table 4.7, together with the summary of the different switches positions, the phases feeding each element and finally the radiated field and its module. It can be seen that as expected, when the antenna is configured with circular polarization, the radiated fields are maximum while when configured in linear polarization, the radiated field will be 3dB lower.

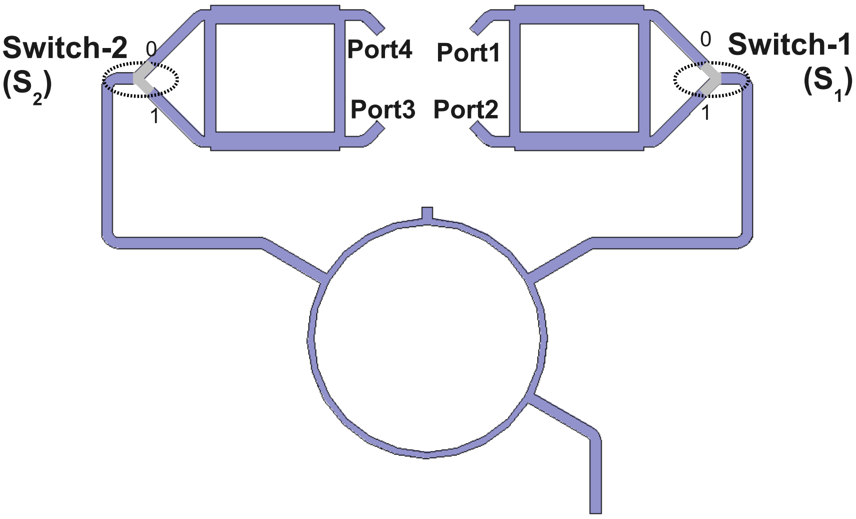

Figure 4.43: 4-Qdime Feed Network

Because the existence of a ground plane and the complexity of the network, the technology used in this case have been microstrip lines. The substrate used in this case has been chosen between the four MMW frequencies materials studied previously: Quartz, PTFE, LTCC and BCB. Quartz glass and PTFE materials have been rejected because their minimum commercial thicknesses ($500\mu m$)

requires a wider microstrip lines compared to the final antenna dimensions. Because the feed network is at a separate layer than the antenna, the use of an elevated permittivity substrate would reduce the lines dimensions without effecting the antenna radiation characteristics. Therefore, LTCC seems to be the most suitable substrate because its higher permittivity and lower losses in a microstrip structure. An initial feed network design has been done with the circuital model in Advanced Design System (ADS) from Agilent. The problem appeared because LTCC fabrication technology exhibits a minimum lines strip width of $50\mu m$ with a 1% tolerances [42], which are higher than the required in the network designed. Finally, a feed network printed on $30\mu m$ thick Benzocyclobuten polymer (BCB) has been designed, with a fabrication tolerances of $1\mu m$ using Microfabrication.

Switches		Antenna Ports				$\overrightarrow{E}$	$\lvert\overrightarrow{E}\rvert$	Polarization
S_1	S_2	1	2	3	4			
0	0	0°	90°	270°	180°	$(1+j)\widehat{x}-(1+j)\widehat{y}$	2	HLP
0	1	0°	90°	180°	270°	$2\widehat{x}-2j\widehat{y}$	$2\sqrt{2}$	LHCP
1	0	90°	0°	270°	180°	$-2j\widehat{x}-2\widehat{y}$	$2\sqrt{2}$	RHCP
1	1	90°	0°	180°	270°	$(1+j)\widehat{x}-(1+j)\widehat{y}$	2	HLP

Table 4.7: Switches configuration to have polarization reconfigurability

Rat-race Hybrid: The 180° Hybrid junction is characterized for being a four-port network with a 180° phase shift between the two output ports (Fig. 4.44). When a signal is applied to port 4, it is split into two components with a 180° phase difference at ports 2 and 3 while port 1 is isolated. If the signal is applied to port 1, is split into two in-phase components at port 2 and 3 while port 4 is isolated.

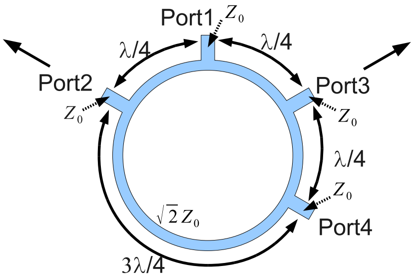

$$[S_{180^o}] = \frac{-j}{\sqrt{2}}\begin{bmatrix} 0 & 1 & 1 & 0 \\ 1 & 0 & 0 & -1 \\ 1 & 0 & 0 & 1 \\ 0 & -1 & 1 & 0 \end{bmatrix}$$

Figure 4.44: Rat-race hybrid

Two different designs of the *Rat-race* have been done for V- and W-band, centered at 60GHz and 76GHz respectively. Fig. 4.45(a) illustrates the power amplitude at the hybrid two output ports and the good matching of the input port. As needed, the power applied at the hybrid junction is distributed equally between ports 2 and 3. Fig. 4.45(b) illustrates the phase difference of the signal in the two ports. Can be easily seen that at the center frequency, both designs induce a 180°

phase shift between the two output ports.

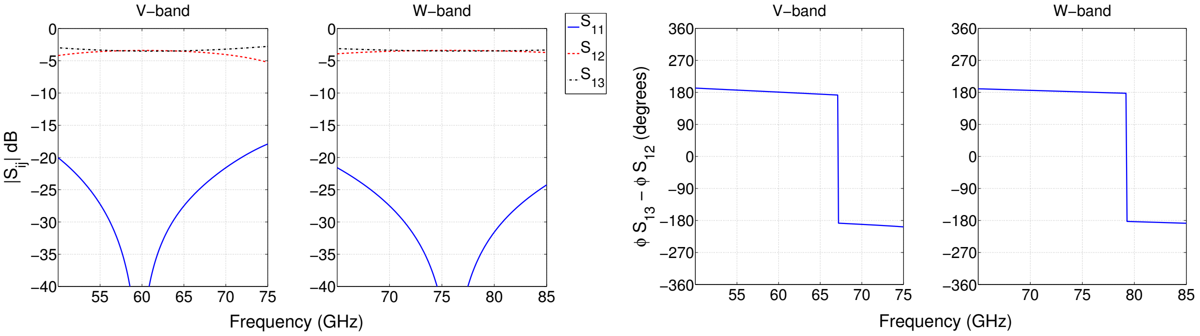

(a) Power Amplitude

(b) Phase difference

Figure 4.45: Rat-race Hybrid S-parameters and Phase difference

Quadrature Hybrid: The 90° Hybrid junction is a 3dB directional coupler with a 90° phase difference in the output ports (Fig. 4.46). With all ports matched, its basic operation consists of dividing the power entering at port 1 into equal powered signals at port 2 and 3 with a 90° phase shift. No power is coupled to port 4, which is isolated. Depending if the input port is 1 or 4, the phase shift will be ±90°.

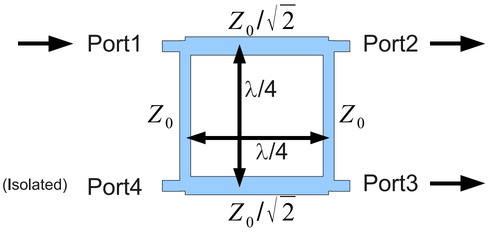

$$[S_{90^o}] = \frac{-1}{\sqrt{2}} \begin{bmatrix} 0 & j & 1 & 0 \\ j & 0 & 0 & 1 \\ 1 & 0 & 0 & j \\ 0 & 1 & j & 0 \end{bmatrix}$$

Figure 4.46: Quadrature hybrid

The Quadrature hybrid has been designed to operate at V-band and W-band. Fig. 4.47(a) shows the power at ports 2 and 3 when a signal is applied at port 1. Fig. 4.47(b) shows the resulting 90° phase shift at the center frequency (60GHz) between the output ports.

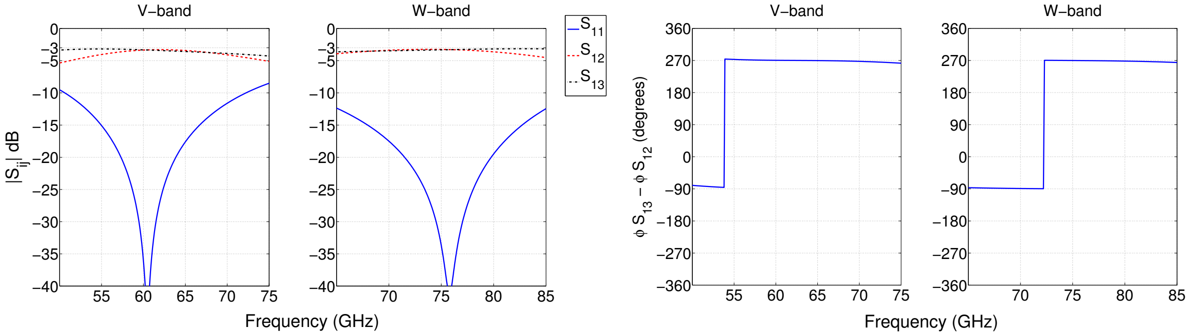

(a) Power Amplitude

(b) Phase difference

Figure 4.47: Quadrature Hybrid S-parameters and Phase difference

Qdime parameter	Quartz Antenna	BCB Antenna
S_{pat}	1000 μm	1270 μm
l_{upp}	30 μm	400 μm
l_{low}	120 μm	389 μm
l_{sli}	250 μm	116 μm
h_{upp}	150 μm	30 μm
h_{low}	300 μm	30 μm
h_{rad}	None	500 μm
w_{upp}	190 μm	50 μm
w_{low}	100 μm	121 μm
d_{feed}	202 μm	35 μm

Table 4.8: 4-Qdime antenna parameters to operate at V-band

4.3.3 V-band Prototypes

Two different prototypes of the 4-Qdime antenna have been designed to operate at 60GHz. One uses Quartz ($\varepsilon_r = 3.9$ and $tan\delta = 0.0007$) as dielectric and the other uses Benzocyclobuten polymer (BCB) ($\varepsilon_r = 2.52$ and $tan\delta = 0.002$). The reason to have done two designs in different substrates comes from the difficulty to etch quartz for the antenna feed probe and vertical walls, while this etching process has not difficulty when done in a BCB substrate. By the other hand, the maximum amount of BCB deposition possible is $30\mu m$ [41] which is substantial lower than the $500\mu m$ of quarts substrate, resulting into a narrower frequency bandwidth. A $500\mu m$ (h_{rad}) quartz top layer has been used in the BCB design, primarily to obtain a good impedance matching by reducing the ε_{eff} and also used as a base surface when manufactured. The feed network in both designs consists of gold printed on $30\mu m$ thick BCB deposited layer. Table 4.8 summarizes the antenna main parameters for both designs.

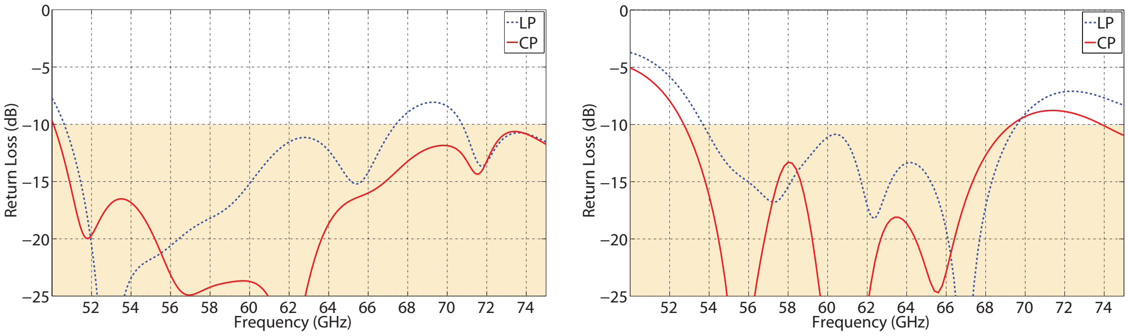

(a) Quartz Substrate (b) BCB Substrate

Figure 4.48: V-band 4-Qdime antenna Return Loss

The two antenna designs have been simulated with the finite elements method Ansoft HFSS simulator. Fig. 4.48(a) illustrates the return loss of the Quartz substrate antenna when configured in LP and CP, showing a -10dB return loss frequency bandwidth of 28%. Fig. 4.48(b) represents the impedance matching for the BCB substrate antenna, with a frequency bandwidth of 25%.

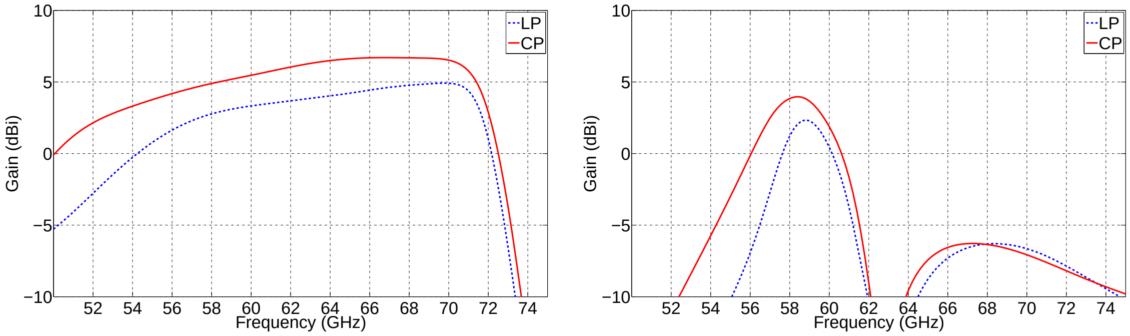

(a) Quartz substrate (b) BCB Substrate

Figure 4.49: V-band 4-Qdime antenna Gain

Fig. 4.49 illustrates the antenna gain as a function of frequency for the two prototypes. In both cases, the antenna gain when configured in CP is higher than when configured in LP as expected. In the quartz substrate prototype, the gain is 5.46dB at the center frequency (60GHz) when in CP and it is 3.8dB when in LP. The gain in the antenna with BCB drops radically inside the V-band bandwidth. This drop is caused by the higher loss tangent presented in BCB together with the narrow bandwidth due to the electrically thin substrate. The gain at the center frequency is 1.9dB and 0.4dB for each polarization. Looking at the radiation pattern presented in Fig. 4.50, the antenna with quartz has a HPBW of 90° when configured in CP and 50° when configured in LP. The pattern for the BCB at 60 GHz, out of the gain drop, shows 60° and 30° HPBW when configured in CP and LP respectively.

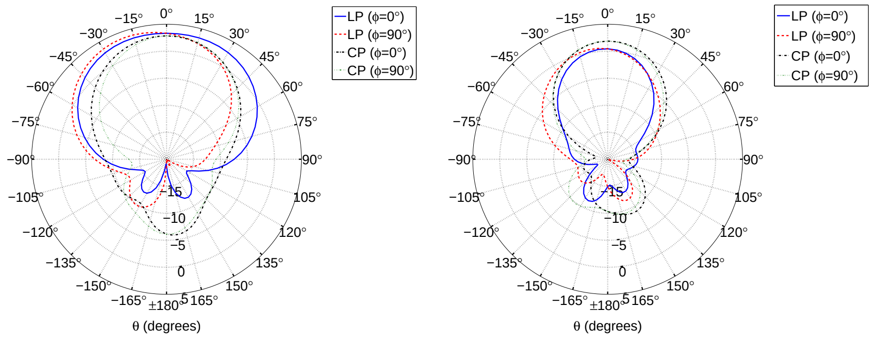

(a) Quartz substrate (b) BCB Substrate

Figure 4.50: V-band 4-Qdime antenna Radiation Pattern at 60GHz

The 4-Qdime antenna axial ratio against frequency for the maximum radiation direction is presented in Fig. 4.51. As expected from its wider frequency bandwidth, the antenna with quartz has a wider 3dB Axial Ratio frequency bandwidth of 29% in front the BCB antenna 10%. Concerning the axial ratio in the yz-plane (Fig. 4.51(b)) it can be seen that the design with quartz has a 3dB

Qdime parameter	BCB Antenna
S_{pat}	900 μm
l_{upp}	250 μm
l_{low}	296 μm
l_{sli}	171 μm
h_{upp}	30 μm
h_{low}	30 μm
h_{rad}	30 μm
w_{upp}	46 μm
w_{low}	92 μm
d_{feed}	15 μm

Table 4.9: 4-Qdime antenna parameters to operate at W-band

beamwidth of 190° while the BCB design has a 3dB beamwidth of 85° .

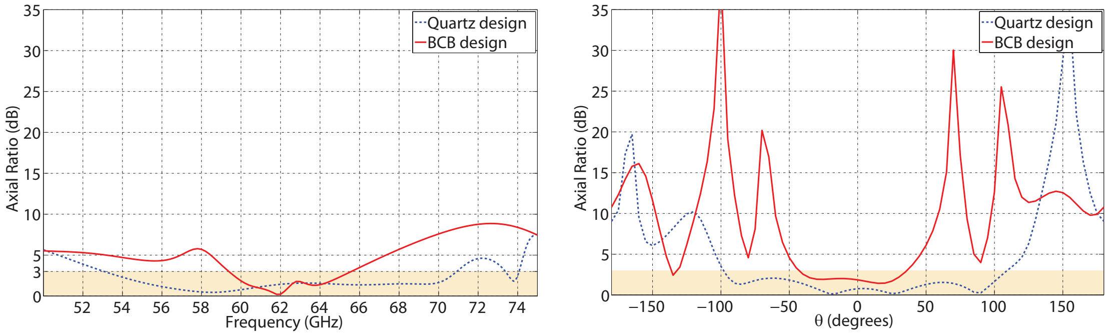

(a) Axial Ratio against Frequency

(b) Axial Ratio against θ

Figure 4.51: V-band 4-Qdime antenna Axial Ratio

4.3.4 W-band Prototypes

One of the designs has been also studied into the W-band. The substrate chosen in this design has been BCB ($\varepsilon_r = 2.52$ and $tan\delta = 0.002$), with a thickness of 30μm for each layer. A quartz top layer has also been used to obtain a correct impedance matching. This layer also works as the base surface in the manufacturing process. Like it was done in the V-band designs, the feed network consist of gold printed on BCB of 30μm thickness. Table 4.9 summarizes the design main parameters.

The antenna return loss for the antenna configured in Circular Polarization (CP) and Linear Polarization (LP) is shown in Fig. 4.52. It can be observed a -10dB return loss frequency bandwidth of 22% and 14% respectively.

The antenna gain against frequency is presented in Fig. 4.53(a), showing at the center frequency (76 GHz) a gain of 2.3dB and 0.1dB for the antenna configured in CP and LP respectively. Because

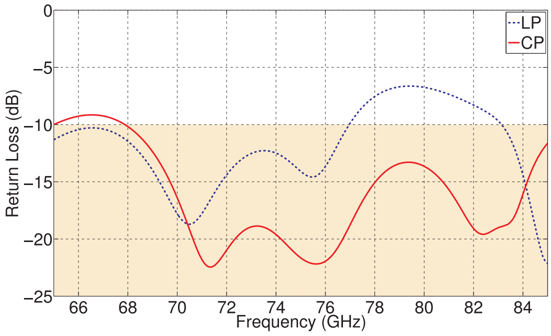

Figure 4.52: W-band 4-Qdime antenna Return Loss

the electrical thickness has increased together with the frequency, the W-band design presents a wider frequency bandwidth that is also reflected in the gain. Fig. 4.53(b) shows the radiation pattern at the center frequency, with a HPBW of 75° when configured in CP and 70° when configured in LP.

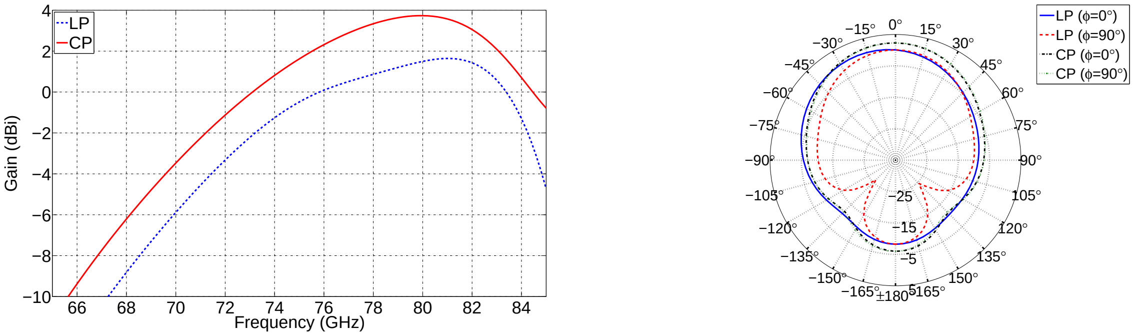

(a) Antenna Gain

(b) Radiation Pattern at 76GHz

Figure 4.53: W-band 4-Qdime antenna Gain and Radiation Pattern

The last parameter to analyze is the axial ratio. Fig. 4.54(a) illustrates the antenna axial ratio with a 3% frequency bandwidth related to a 3dB axial ratio. The antenna radiation pattern shows a 65° beamwidth related to the 3dB axial ratio.

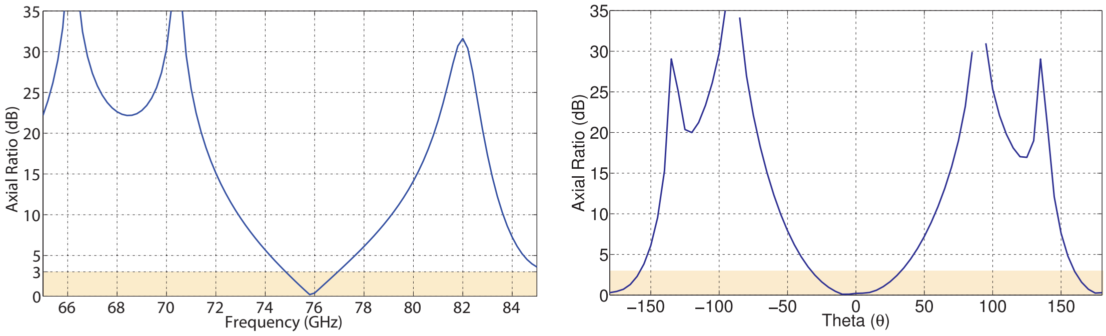

(a) Axial Ratio against Frequency

(b) Axial Ratio against θ

Figure 4.54: W-band 4-Qdime antenna Axial Ratio

4.4 Summary and Comparison

In this chapter, two different polarization reconfigurable antenna structures have been presented. One is a single reconfigurable element (CPW Patch) and the second is a composed architecture (4-Qdime). The CPW Patch antenna has been designed to operate at Ka-band (26.5 to 40GHz) and at V-band (50 to 75GHz), and the 4-Qdime antenna has been designed to operate at V-band and W-band (75 to 110GHz). Table 4.10 summarizes the main characteristics of the different antennas.

Parameter		Ka-band	V-band			W-band
		CPWP	CPWP	Quartz Qdime	BCB Qdime	BCB Qdime
RL Frequency Bandwidth	LP	9%	16%	28%	25%	14%
	CP	30%	30%			
Gain (dBi)	LP	3.6	5.6	3.8	0.4	0.1
	CP			5.5	1.9	2.3
Half Power Beamwidth	LP	70^o	86^o	80^o	30^o	70^o
	CP			90^o	60^o	75^o
3dB Axial Ratio Frequency Bandwidth		5%	6%	29%	10%	3%
3dB Axial Ratio Beamwidth		80^o	70^o	190^o	85^o	65^o

Table 4.10: Polarization Reconfigurable Antennas Electrical Characteristics Comparison

The first design presented has been the polarization reconfigurable CPW Patch. From the linearly polarized square structure, the circular polarization is obtained by truncating two pairs of opposite corners, inducing the required orthogonal modes with equal amplitude and phase quadrature. Reconfigurability is obtained connecting four parasitic triangular shape conductors to the main patch with RF-MEMS switches. Because the antenna coplanar architecture and the high operating frequency, the antenna is fed with CoPlanar Waveguide. These lines require the use of air-bridges to avoid the odd-mode excitation. Initial designs at Ka- and V-band have been proposed as Hard-Wire (HW) prototypes. It means that the switches are represented with a short-circuit when ON and with an open-circuit when OFF. Because the dimensions and low isolation at high frequencies of the RF-MEMS switches presented, only a Ka-band prototype has been designed with integrated switches.

Concerning the electrical characteristics of the CPW Patch antenna, the Ka-band prototype has a frequency bandwidth related to the return loss of 9% when configured in LP and of 30% when configured in CP, while the V-band prototype has a 16% and 30% respectively. The CP has a wider bandwidth because it has two resonant modes that combined increase the bandwidth in comparison to the single resonant mode used in LP. Due to different substrate electrical thickness, the V-band design increases its directionality, having a gain in the main direction of 5.6dBi in front of the 3.6dBi presented in the Ka-band. Both antennas have a wide beamwidth, with a HPBW of 70° and 86° for Ka- and V-band respectively. The antenna axial ratio presents a 5% frequency bandwidth and a central frequency beamwidth of 80°.

In order to obtain a wider frequency bandwidth related to the axial ratio, a linear-polarized elements composed architecture such as the 4-Qdime antenna has been studied. The antenna consist of a four Qdime antennas arranged in a 2×2 square grid and rotated 90°. Depending on each Qdime excitation phase, the antenna is capable to radiate in LP or in CP. An RF-MEMS switches reconfigurable feed network architecture with microstrip transmission lines has been proposed. It consist of a Rat-race hybrid (180°) connected to two Quadrature hybrids (90°). Depending on which port the Rat-race is connected to the Quadrature hybrids, the antenna presents linear or circular polarization. Two prototypes of the 4-Qdime antenna have been designed to operate at V- and W-band. Quartz substrate has been used as the antenna dielectric in a V-band prototypes while Benzocyclobuten polymer (BCB) has been used in designs at both frequency bands. The two antennas with BCB require the use of a quartz top layer which increases the effective permittivity (ε_{eff}) and therefore helps with the antenna matching. The three antennas microstrip feed networks are printed on $30\mu m$ BCB substrate.

Parameter	Ka-band	V-band			W-band
	CPWP	CPWP	Quartz Qdime	BCB Qdime	BCB Qdime
Electrical Dimensions	$0.21\lambda_0 \times 0.21\lambda_0$		$0.78\lambda_0 \times 0.78\lambda_0$		$0.9\lambda_0 \times 0.9\lambda_0$
Polarization Types	LHCP RHCP VLP	LHCP RHCP VLP	LHCP RHCP HLP	LHCP RHCP HLP	LHCP RHCP HLP
Minimum Linewidth	$50\mu m$	$10\mu m$	$30\mu m$	$30\mu m$	$30\mu m$
Minimum Slotwidth	$10\mu m$	$5\mu m$	$20\mu m$	$20\mu m$	$200\mu m$
Radiation Directionality	Bidirectional		Unidirectional		
Single Layer/Multilayer	Single Layer		Multilayer		
Feed Network	CPW		Microstrip		

Table 4.11: Polarization Reconfigurable Antennas Characteristics Comparison

Focusing on the electrical characteristics, the V-band prototypes have a frequency bandwidth related to return loss wider than 25% and the W-band prototype has a 14% bandwidth. The gain of the antenna depends on the configured polarization , being higher for the two CP than for the LP.

The antenna gain when configured in CP is 5.5dBi for the quartz based antenna, while is 1.9dBi and 2.3dBi for the BCB based antenna at V- and W-band respectively. The HPBW also differs from the polarization type, being between 60^o and 90^o for the different prototypes. Concerning the axial ratio of the 4-Qdime antenna when configured in CP, the 3dB axial ratio frequency bandwidth is 29% for the quartz antenna at V-band, 10% for the BCB antenna at V-band and 3% for the antenna operating at W-band. The gain and axial ratio bandwidth differences between the Quartz and BCB prototypes are mainly because the different electrical thickness, with $0.1\lambda_0$ for the Quartz and $0.006\lambda_0$ for the BCB.

Concerning physical dimensions, it can be seen that while the CPW Patch antenna has a fixed square dimension around $0.2\lambda_0$, the 4-Qdime antenna dimensions depend on the feed network and therefore it depends on the network dielectric used and its permittivity. CPW Patch antennas are good candidates to be used in phased arrays because it is possible to set an array with elements distance lower than $\lambda_0/2$, eliminating grating lobes. All designed antennas require a fabrication accuracy of tenths of micrometers. Differences between the CPW Patch antenna and the 4-Qdime relay into their radiation directionality, number of layer used and feed network technology used. While CPW Patch antenna is a bidirectional single-layer CPW antenna, the 4-Qdime is an unidirectional multilayer microstrip antenna. Table 4.11 summarizes the different antenna comparisons.

Chapter 5

Polarization- and Pointing-Reconfigurable Array Antenna

High gain antennas are commonly used in MMW communication systems to compensate the high path loss. This type of antennas are also characterized for having a narrow beamwidth which reduces the multipath contributions by limiting the angle from which radiation is emitted and captured. In some applications, the use of narrow beamwidth antennas improves also the spatial utilization with a frequency reuse. Such antennas precise to be pointed in order to have a Line-of-sight (LOS) path link, being this pointing done mechanically or electrically. In communication systems where the antennas alignment is essential for the good link performance, the antenna capability to reconfigure the pointing direction electrically is very useful to avoid constantly antenna manipulation. The use of antenna arrays provides high gain antennas with pointing direction reconfigurability capability by changing the phase that feeds each element. Polarization reconfigurable base elements allow the system to readjust the orientation of the radiated field to minimize polarization loss factor.

In this chapter, beamsteering using phased arrays is introduced. Then, 1-bit discrete phase-shifter pointing-reconfigurable array antennas using the polarization reconfigurable CPW Patch and 4-Qdime antennas are presented and compared.

5.1 Phase-shift Beamsteering

The term beamsteering relates to the capability of an antenna to focus energy toward a specific direction in space [57]. In an antenna array, beamsteering may be accomplished by changing the relative phases of the RF signal driving the array elements and thus controlling the phase contribution to the electromagnetic radiated far-field.

The number of elements used in the array and therefore its effective area (A_{eff}) is being defined by the final antenna desired directivity. Also the HPBW in the two main radiation pattern axis ($\Delta\theta^{(1)}_{-3dB}$ and $\Delta\theta^{(2)}_{-3dB}$) are related to the antenna directivity through the antenna solid angle (Ω_e)

$$D = A_{\text{eff}}\frac{4\pi}{\lambda_0^2} \tag{5.1}$$

$$D = \frac{4\pi}{\Omega_e} = \frac{4\pi}{\Delta\theta^{(1)}_{-3dB}\Delta\theta^{(2)}_{-3dB}} \tag{5.2}$$

The distance between the array elements will be preferably lower than λ_0 in order to avoid the appearance of grating lobes in the radiation pattern [34]. When designing phased array antennas, an element distance lower than $\lambda_0/2$ assures no grating lobes for any value of the progressive phase.

5.1.1 Array Factor (AF)

The radiation pattern of an antenna array is the result of multiplying the single element radiation pattern, $\vec{E}_0$, by the Array Factor, $AF(\psi)$, which takes into account the interference of each wave radiated by each element [32]. The AF depends exclusively of the elements distance, the excitation amplitude and phase, and the operating frequency. The antenna array can be one-dimensional or two-dimensional. In a planar array, the AF can be computed as combination of the AF for the two main planes if the feeding can be separated in two variables for each plane $AF(\psi_x, \psi_y) = AF_x(\psi_x)AF_y(\psi_y)$. This thesis focuses in linear arrays, with the AF computed as:

$$AF(\psi) = \sum_{n=0}^{N_{arr}-1} a_n e^{jn\psi} \tag{5.3}$$

where ψ is the electrical angle, N_{arr} the number of array elements and a_n the current feeding the n^{th} element.

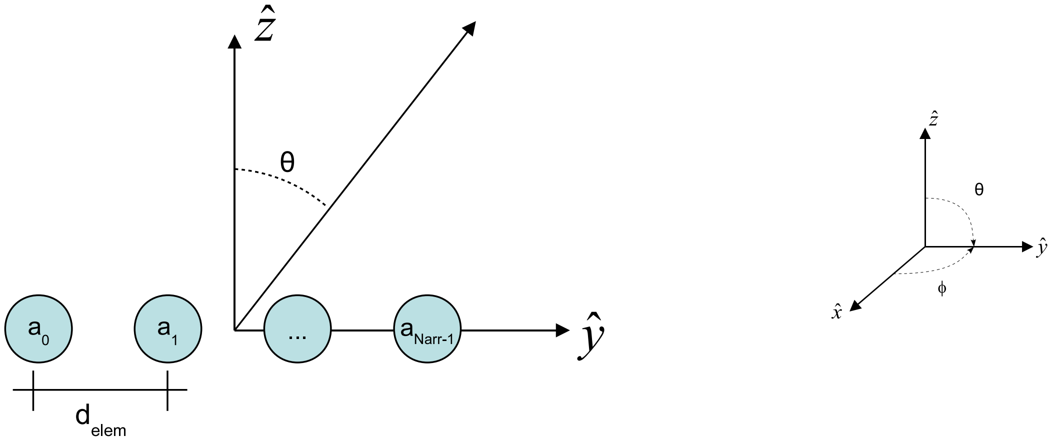

Figure 5.1: Antenna Array along y-axis

For an antenna array with the elements placed along y-axis as shown in Fig. 5.1, the electrical angle is computed as $\psi = k_0 d_{elem} sin(\theta) + \alpha$, where k_0 is the wave number in vacuum, d_{elem} is the elements distance, and α is the array progressive phase. The maximum radiation direction, θ_{max}, depends on the elements progressive phase (α) and corresponds to the pointing angle which sets the electrical angle to zero ($\psi = 0$). In the case under study, θ_{max} is computed as:

$$\theta_{max} = arcsin\left(-\frac{\alpha}{k_0 d_{elem}}\right) \tag{5.4}$$

As an example, Fig. 5.4 illustrates the radiation pattern of a 16 omnidirectional elements with a d_{elem} equal to $\lambda_0/2$ for three different values of α (0°, -90° and -155°) corresponding to a beam tilt of 0°, 30° and 60° respectively.

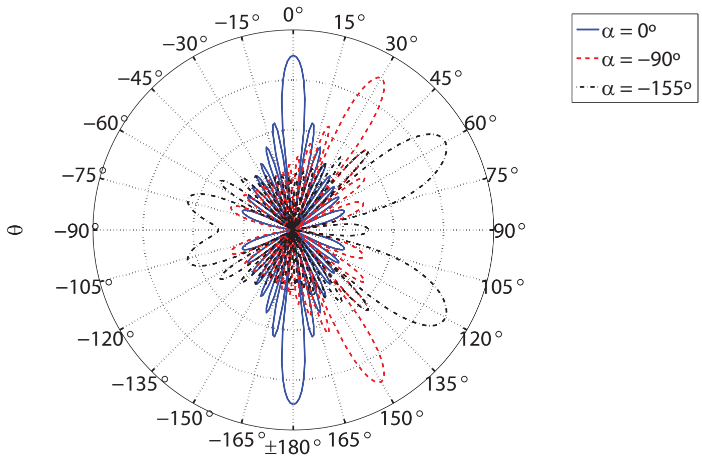

Figure 5.2: 16 omnidirectional-elements array radiation pattern for three different values of the progressive phase (α)

5.1.2 Discrete Phase-Shifters

Digital reconfigurable phase-shift beamsteering has the inconvenience that the number of phase-shifter states at each element is finite and it should be minimized in order to reduce the antenna complexity. An easy way to implement a digital phase-shifter is by using the switched delay-time technique [16], which has different phase-shifts that combined result into the desired phase-shifter. Fig. 5.3 shows a 3-bit phase-shifter based in concatenating three different phase-shifts. The final phase shift depends of the shifts combination as summarized in Table 5.1.

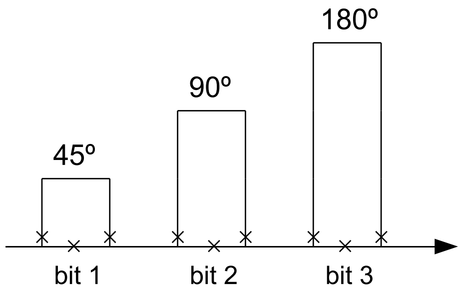

Figure 5.3: 3-bit phase-shifter using switched-lines

Table 5.1: 3-bit Final Phase

bit-1	**bit-2**	**bit-3**	**Final Phase**
0	0	0	0°
1	0	0	45°
0	1	0	90°
1	1	0	135°
0	0	1	180°
1	0	1	225°
0	1	1	270°
1	1	1	315°

In an antenna array, there are two equivalent ways to analyze the use of discrete phase-shifters.

The first one is to compute each element phase error as the difference between the progressive phase at the element with its discrete phase ($e_{\beta n} = n\alpha - \beta_n$) and apply it to the current , leading to compute the Array Factor for an y-axis elements distribution as:

$$AF(\psi) = \sum_{n=0}^{N_{arr}-1} |a_n| e^{je_{\beta n}} e^{jn(k_0 d_{elem} sin(\theta)+\alpha)}$$

The second way is to consider the progressive phase null (α=0) and apply each discrete phase (β_n) to the element current, $a_n = |a_n|e^{j\beta_n}$. β is defined as the vector that describes each element phase, $\beta = [\beta_1 \beta_2 \cdots \beta_{Narr}]$. Then the phase-shifted Array Factor is computed as:

$$AF(\psi) = \sum_{n=0}^{N_{arr}-1} |a_n| e^{j\beta_n} e^{jnk_0 d_{elem} sin(\theta)}$$

5.2 1-bit CPW Patch Antenna Array

The polarization reconfigurable CPW Patch antenna presented previously, has been used to design a beam pointing reconfigurable antenna. A 4-element linear array is being used to achieved an antenna gain higher than 10.5 dB. Two different designs have been done, one that operates at Ka-band and another at V-band. Focusing at V-band applications, this gain value corresponds to the minimum antenna gain required for a 10 meters BPSK and QPSK modulation communication link.

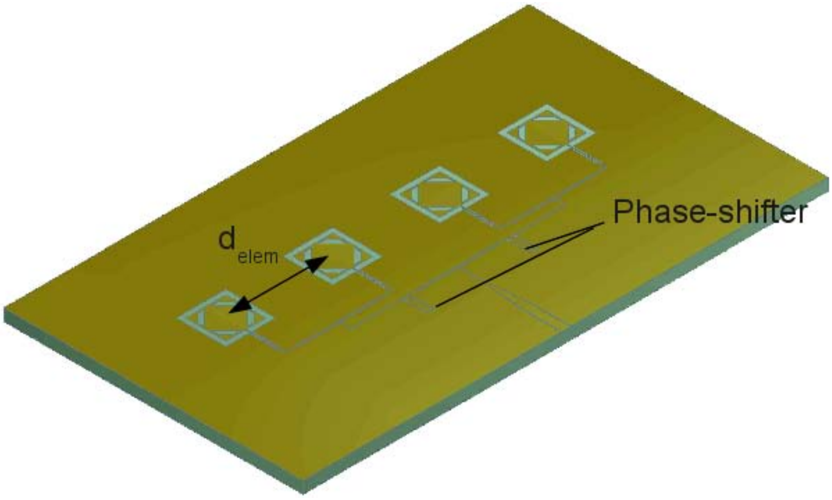

Figure 5.4: 4-elements CPW Patch antenna array

The array is characterized for having an inter-element distance (d_{elem}) of $0.45\lambda_0$, which assures no grating lobes for any value of the progressive phase. The final radiation pattern is obtained by multiplying the array factor (AF) to the single element radiated field ($\vec{E}_0(\vec{r})$). Fig. 5.5 shows the 4-element linear array radiation pattern for a uniform amplitude distribution ($a_n = 1$) and a null progressive phase (α=0). The Ka-band array has a gain of 9.4 dBi with a beamwidth of 30° at yz-plane. The gain difference between $\theta = 0^o$ and $\theta = 180^o$ beams is 1dB and the Sidelobe Level (SLL) is 15dB. The V-band array has a gain of 10.3dBi with a Half-Power Beamwidth (HPBW) of 30^o. The two main direction beams have a gain difference of 4.8dBi and the SLL is 14.5dB.

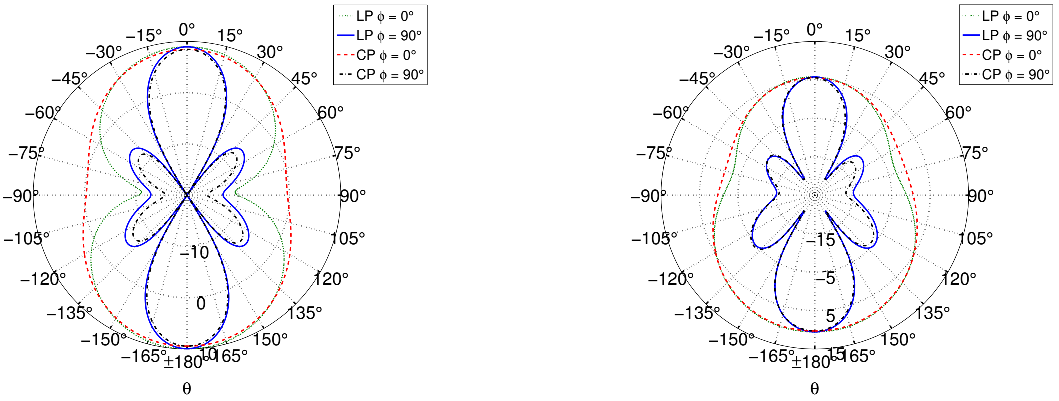

(a) Ka-band (b) V-band

Figure 5.5: Radiation Pattern of a 4-elements CPW Patch linear array with d_{elem}=$0.45\lambda_0$, $a_n = 1$ and $\alpha = 0$

Because the array HPBW is 30^o, it is desired that the phased array has the capability to point the main beam with steps of 15^o. Fig. 5.6 shows the radiation pattern for the three progressive phases that give a tilt angle of 15^o, 30^o and 45^o. It can be seen that for α=-115^o the beam is not pointing at 45^o degrees. This is due to the base element lack of omnidirectionallity, resulting in gain reduced more than 3dB at the desired pointing angle.

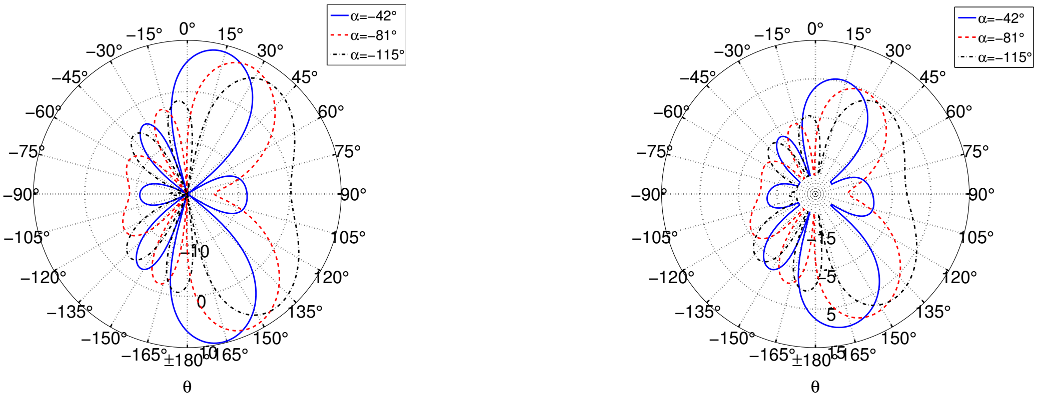

(a) Ka-band (b) V-band

Figure 5.6: Radiation Pattern of a 4-elements CPW Patch linear array with d_{elem}=$0.45\lambda_0$ and $a_n = 1$

In order to implement the pointing reconfigurable array, discrete phase-shifters have to be used. The difficulty relays in the fact that to feed each element with the appropriate phase would require four phase-shifts at each element. An alternative is to find a set of phases that generate a similar-like slope between elements phases. In the case under study, it has been decided to reduce the complexity by limiting the system to 1-bit phase-shifter, limiting then the pointing angles to $\theta = 0^o$ and $\theta = \pm 15^o$. The progressive phase required to point the beam to $\theta = \pm 15^o$ is $\alpha = \mp 42^o$. The closest approximation to an ideal progressive phase using 1-bit phase-shifter is given by grouping the elements in two groups. In the four elements array case, the grouping results in two groups of two elements with a distance between groups double than the original distance. Then, in order to maintain the pointing angle, the progressive phase in equation 5.4 has to be doubled. Therefore, the phase-shift of the discrete phase-shifter will be $\alpha = \mp 84^o$, which in the case under study has been approximated to -90^o as shown in Fig. 5.7.

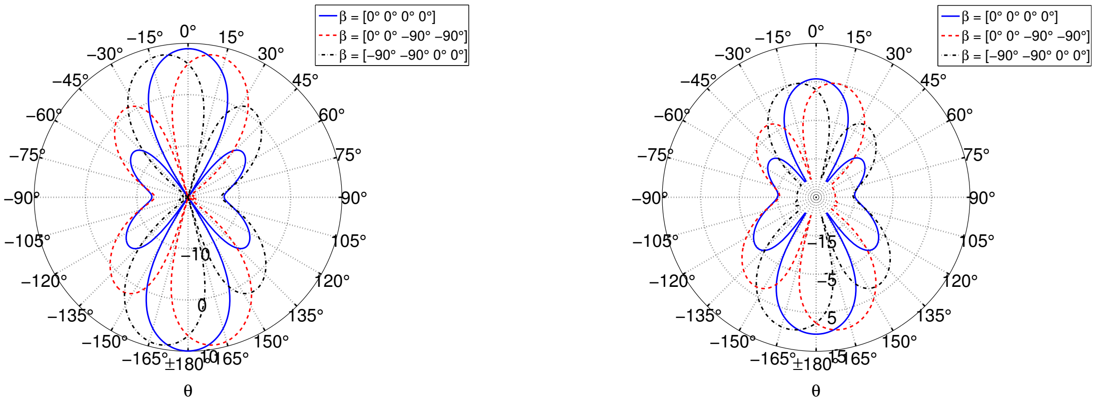

(a) Ka-band

(b) V-band

Figure 5.7: Radiation Pattern of a 4-elements CPW Patch linear array with 1-bit phase-shifter

A prototype of the pointing reconfigurable array with the presented RF-MEMS switches integrated has been designed to operate at Ka-band. The structure has been modeled and optimized with the finite elements method Ansoft HFSS simulator. The network to feed the 4-elements array has been designed using CPW lines. This type of lines requires the existence of air-bridges in all the discontinuities to avoid the excitation of the odd-modes. Each element equal power distribution has been done using $\lambda/4$ power dividers. (Fig. 5.8(a)). The final phase-shifter configurations allows to reduce the amount of phase shifters to two. They consist of a transmission line of length $\lambda_0/2$ and they are connected by using RF-MEMS switches as seen in Fig. 5.8(b).

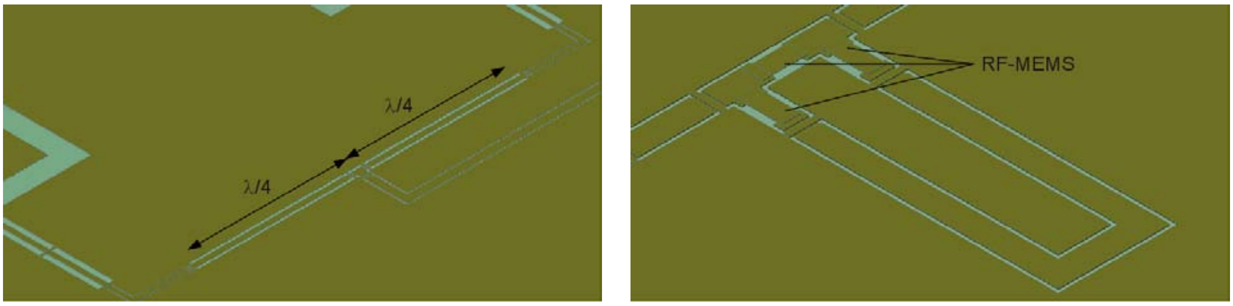

(a) Power Divider

(b) 90^o Phase-shifter

Figure 5.8: CPW Patch linear details

As an attempt to proof the reconfigurability concept, a Hard-Wire (HW) prototype has been designed replacing the RF-MEMS switches by a short-circuit when ON and by an open-circuit when OFF. The array has been simulated with the base element configured in LP and CP. Fig. 5.9(b) shows the gain pattern when all the elements have the same phase ($\beta = [0^o \quad 0^o \quad 0^o \quad 0^o]$) and when one phase-shifter is activated ($\beta = [0^o \quad 0^o \quad -90^o \quad -90^o]$) and therefore the radiation diagram is pointing $\pm 15^o$. It can be seen in Fig. 5.9(a) that both configurations have a good impedance matching for both base-elements polarization-configurations, with a minimum -10dB return loss frequency bandwidth of 18%.

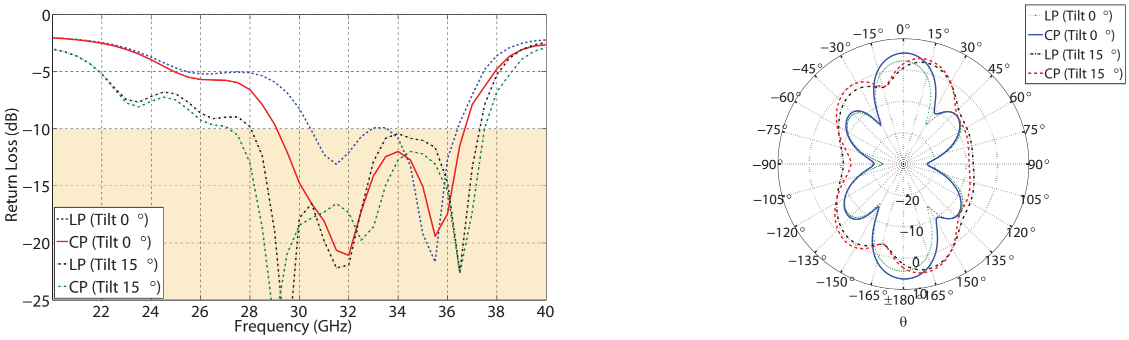

(a) Return Loss (dB)

(b) Radiation Pattern

Figure 5.9: HW reconfigurable array Radiation Pattern and Return Loss

Not only the pointing capacity of the array is needed, but also the capability to maintain the base element polarization. Fig. 5.10(a) shows the antenna axial ratio against frequency in the main beam direction when the base element is configured in CP, for the two pointing cases under study. It can be seen that the 3dB Axial Ratio frequency bandwidth is 3%. Fig. 5.10(b) shows the AR against the pointing angle θ in the yz-plane, where a 3dB AR beamwidth of 18° it is observed when the phase-shifter is not activated and a beamwidth of 12° when the phase-shifter is activated.

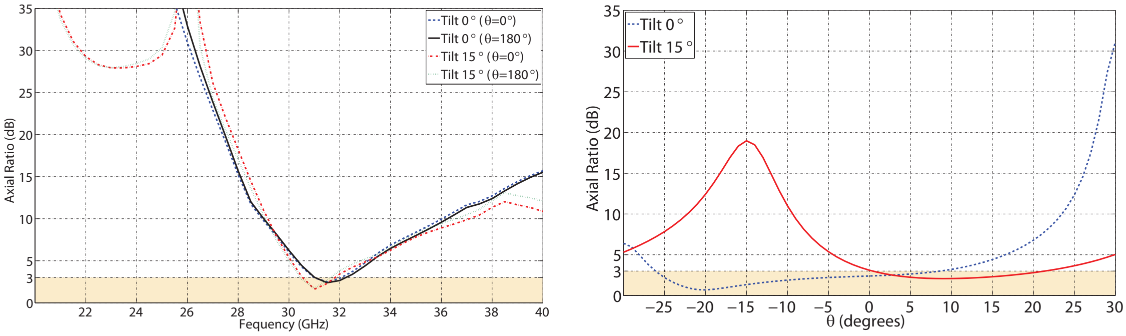

(a) Axial Ratio against frequency

(b) Axial Ratio against theta

Figure 5.10: HW reconfigurable array Axial Ratio

Fig. 5.11 illustrates an instant of the antenna fields when the HW switches are open-circuit and therefore there is no phase shift between the array elements. In the CPW feed network, can be seen the power transmitted to the elements, showing clearly symmetry, having all the elements fed with the same amplitude and in-phase. Fig. 5.12 shows the field when the RF-MEMS from on of the phase shifters are turned ON. In that case, it can be seen the existence of a phase shift because there is no symmetry in the fields, being the signal driven through one of the phase shifters and none in the other.

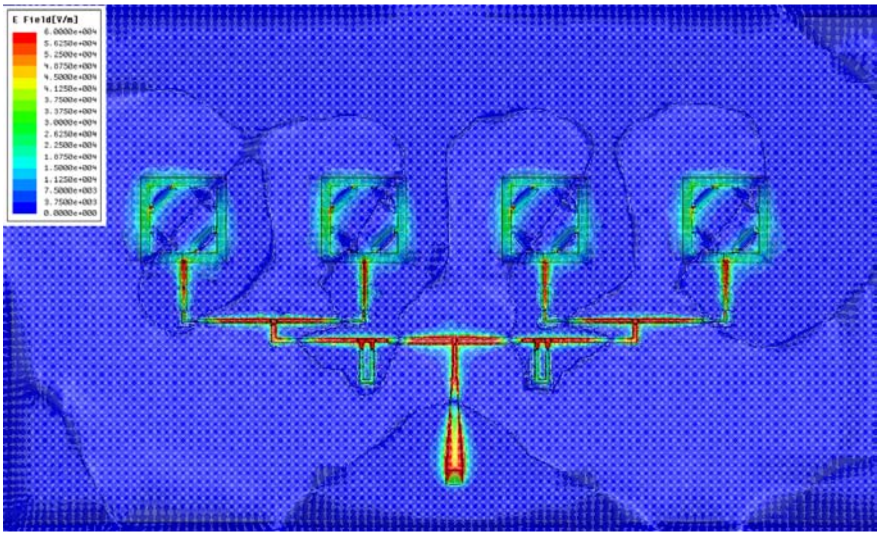

Figure 5.11: CP antenna fields without phase shift between elements

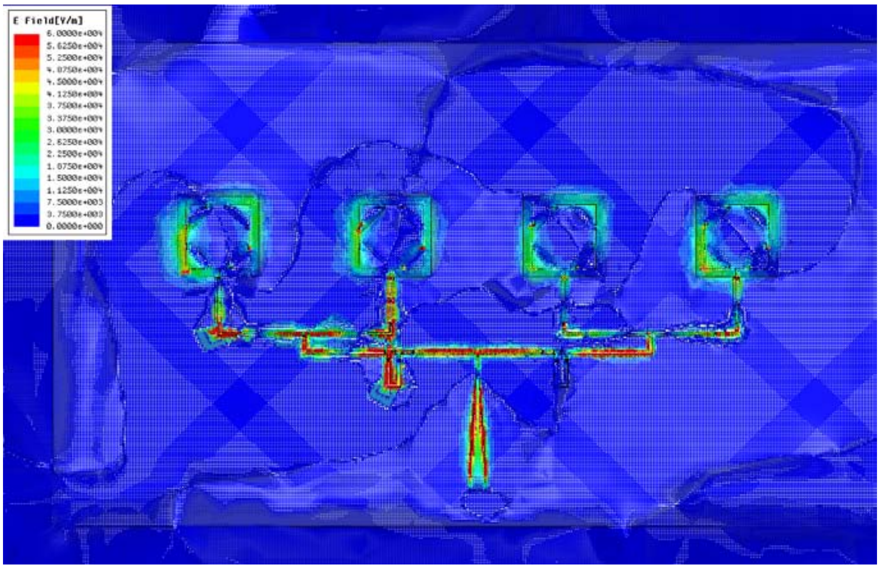

Figure 5.12: CP antenna fields with phase shift between elements

5.3 1-bit 4-Qdime Antenna Array

Two 4-Qdime antenna array have been designed to operate at V-band. The array consist of a four elements with a distance of λ_0, to obtain a gain higher than 10dB. The elements distance has been taken as smaller as possible limited by the base elements dimensions (Fig. 5.13). The elements are fed with a uniform current amplitude and the beam pointing direction reconfigurability is achieve by using discrete phase-shifters. The base elements used are the two different 4-Qdime at V-band presented previously, one using quartz substrate and the other using BCB.

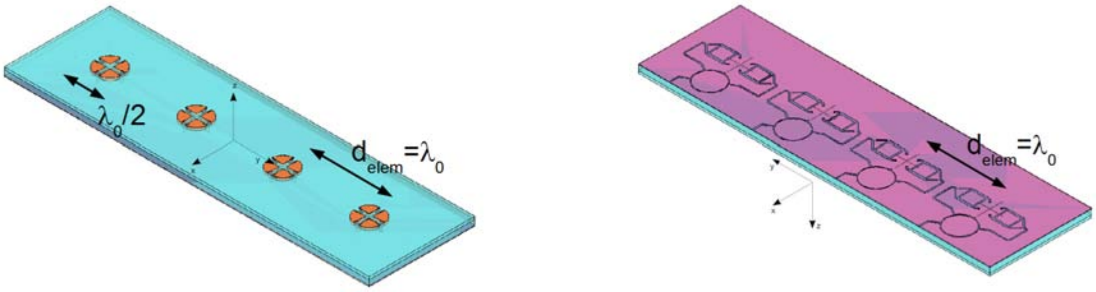

(a) Top View (b) Bottom View

Figure 5.13: 4-Qdime array with 4 elements

The array radiation pattern is obtained by multiplying the base element radiated field ($\vec{E}_0(\vec{r})$) with the array factor (AF). Fig. 5.14 shows the radiation pattern in xz-plane ($\phi = 0^o$) and yz-plane ($\phi = 90^o$) for the array with quartz and with BCB, computed for the antennas configured in LP and CP. The antenna quartz-based has a gain of 13.8dBi with a SLL of 8dB. It also presents a HPBW of 12°, which is lower than the one with the CPW Patch array due to higher elements distance. The antenna BCB-based has a gain of 15.61dBi with a SLL of 13dB. The HPBW for this antenna is 12°.

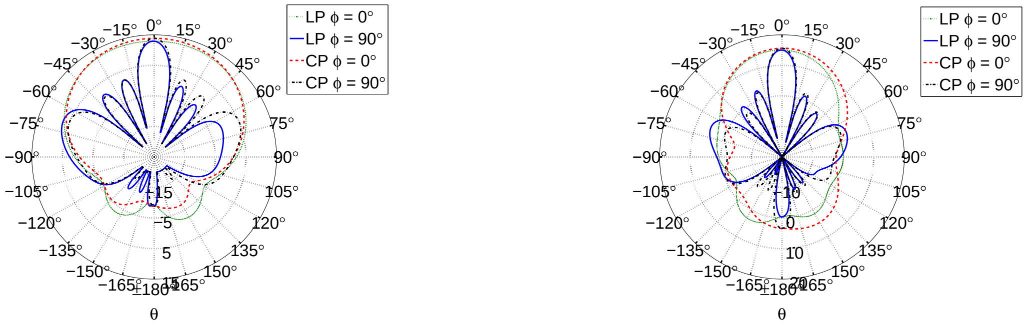

(a) Quartz-based (b) BCB-based

Figure 5.14: Radiation Pattern of a 4-elements 4-Qdime antenna linear array with $d_{elem} = \lambda_0$

A phased array with the capacity to tilt the radiation beam to a maximum angle of ±45° with a step of 15° has been designed. A progressive phase of -93°, -180° and -254° is required to tilt the beam 15°, 30° and 45° respectively. Fig. 5.15 illustrates the resulting radiation pattern at the yz-plane for the different progressive phases. Because the elements distance is λ_0, grating lobes appear into the diagram when progressive phase is applied. It can be seen then that pointing at ±15° and at ∓45 require the same progressive phase and that to point at ±30° it is required a progressive phase of 180°.

Like happened with the CPW Patch array, there is an implementation complexity due to the high number of discrete phase shifts required at each element. The alternative relays into finding

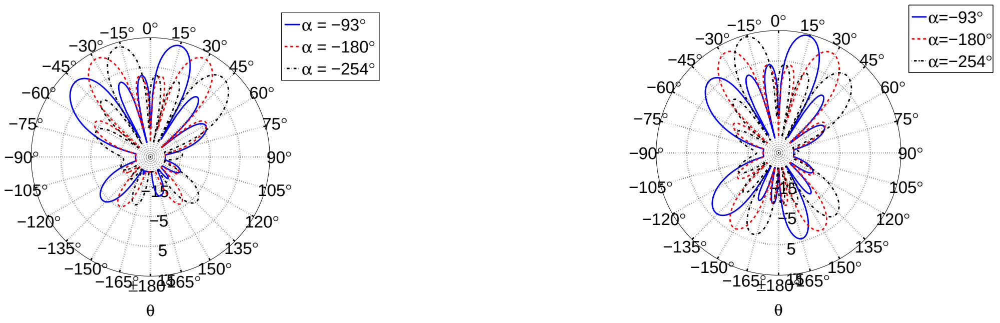

(a) Quartz substrate (b) BCB substrate

Figure 5.15: Radiation Pattern of a 4-elements 4-Qdime antenna linear array with progressive phase

a phase that applied to some of the elements generate a slope phase similar than the one with the progressive phase. In this case, analogously to the CPW Patch array, it has been decided to use a 1-bit 180^o phase-shifter. Of all possible phases combinations, [0^o 0^o 180^o 180^o] and [180^o 180^o 0^o 0^o] generate a radiation pattern pointing to ±15^o, as seen in Fig. 5.16. In this case, the array is capable to point to or have a radiation null at $\theta = 0^o$.

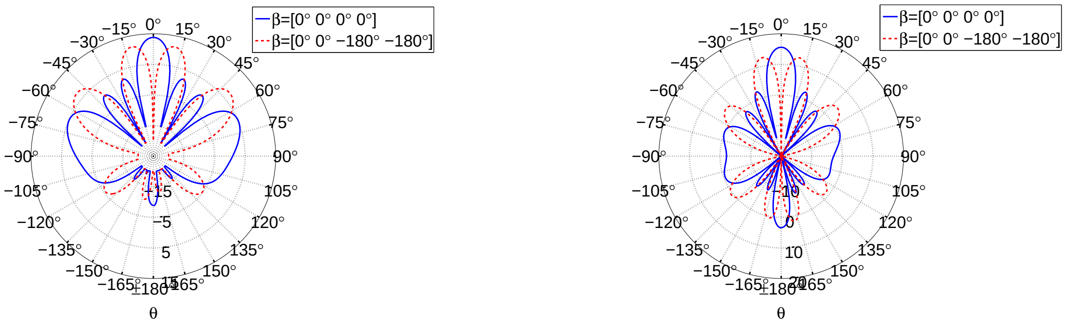

(a) Quartz substrate (b) BCB substrate

Figure 5.16: Radiation Pattern of a 4-elements 4-Qdime antenna linear array with discrete phases

5.4 Summary and Comparison

In this chapter, beamsteering using discrete phase-shifters has been presented. Different 4×1 arrays with polarization-reconfigurable base-elements have been designed to operate at Ka- and V-band. Table 5.2 summarizes the main parameters of each antenna.

The first array type design has used the CPW Patch with an element distance of $0.45\lambda_0$ and a uniform amplitude distribution. The gain when no phase shifting is applied is 9.4dBi for the antenna operating at Ka-band and 10.3dBi for the antenna operating at V-band. Both designs have a Sidelobe Level better than 14.5dB. It has been computed that for the given element distance, a progressive phases of -42^o, -81^o and -115^o make the antenna point to a tilt angle of 15^o, 30^o and 45^o respectively. In this case, the pointing limitations are given by the base element radiation pattern, and concretely the HPBW. For the prototype under study, the discrete phase-shifter complexity

Parameter	Tilt Angle	Ka-band	V-band		
		CPWP	CPWP	Quartz 4-Qdime	BCB4-Qdime
Number of Elements		4	4	4	4
d_{elem}		$0.45\lambda_0$	$0.45\lambda_0$	λ_0	λ_0
Gain (dBi)		9.4	10.3	13.8	15.6
SLL (dB)		15	14.5	10	15
HPBW		30°	30°	12°	12°
Progressive Phase	15°	-42°	-42°	-93°	-93°
	30°	-81°	-81°	-180°	-180°
	45°	-115°	-115°	-254°	-254°
1-bit Phase-shifter		-90	-90	180	180
Grating Lobes		No	No	Yes	Yes

Table 5.2: Polarization- and Pointing- Reconfigurable Array Antenna summary

has been reduced by using a 1-bit phase-shifter with 90° phase-shift, and thus being able to point only to $\theta = \pm 15^{\circ}$. Considering all possible combinations, only two different states have been proofed to have the desired pointing capability, $[0^{\circ}\ 0^{\circ}\ -90^{\circ}\ -90^{\circ}]$ and $[-90^{\circ}\ -90^{\circ}\ 0^{\circ}\ 0^{\circ}]$. This two valid states allow the design to use only two phase-shifters, one for each pair of elements. A polarization- and pointing- reconfigurable prototype operating at Ka-band has been designed with a feed network characterized for having a CoPlanar Waveguide symmetrical-configuration parallel-topology. A prototype with HW switches has been presented. It shows a -10dB return loss frequency bandwidth of 18% for both polarization configurations (LP and CP) and a pointing angle of ±15° when one of the phase-shifters is activated. When polarized in CP, the antenna array presents a 3dB axial ratio frequency bandwidth of 3% and beamwidth of 12°.

The second array studied consisted of four 4-Qdime elements separated λ_0 and fed uniformly. The elements distance is being constrained for each elements feed network. A distance between elements of λ_0 is translated into the appearance of grating lobes into the radiation pattern. The 4-Qdime array radiation pattern has been computed for the V-band antenna with quartz and BCB substrates. Both antennas have a gain higher than 13dBi with a SLL better than 10dB and a HPBW of 12°. Due to the elements distance, the progressive phases that points the main beam through the pointing angle 15°, 30° and 45° are -93°, -180° and -254° respectively. In this case, the grating lobes have a great effect and for example when it is desired to point at 45°, a grating lobe with higher gain appears at -15°. 1-bit phase-shifter of 180°, has been used to reduced the discrete phase-shifter complexity. It has resulted that when the phase-shifter is not activated, the radiation pattern points to $\theta = 0^{\circ}$, having a null in $\theta = \pm 15^{\circ}$. In the case that the phase-shifter is activated, the radiation pattern points simultaneously to ±15° having a null in $\theta = 0^{\circ}$.

Chapter 6

Antenna Microfabrication Process

Once the different base elements and antenna arrays have been designed, next step is the prototype manufacturing. Previously to the fabrication process itself, an analysis of the dimensional and tolerances requirements has to be done to ensure a certain pattern quality (gain, HPBW, beam pointing, SLL and axial ratio). In this chapter, an study of fabrication tolerances for generic antenna arrays is presented and then applied to the CPW Patch array and 4-Qdime array prototypes. Once the fabrication tolerances have been set, the appropriate fabrication process has to be chosen. This chapter includes a summary of the different microfabrication techniques required to fabricate the presented antennas.

6.1 Analysis of Tolerances

The accomplishment of the antenna specifications in terms of directivity, beamwidth, sidelobe levels and axial ratio not only depends on the design itself but also depends on the technology fabrication tolerances. Focusing in an antenna array, the errors may be of two types:

- Systematic or correlated errors. This type of errors are usually related to the array element position and orientation, and can be easily replaced by compensation.

- Random errors. This type of errors are related to radiating element excitation phase and amplitude, and are subjected to statistical manipulation.

In this section, the amplitude and phase errors feeding each base element of an array (Fig. 6.1) are being studied to see how they affect the antenna characteristics such as: gain, Half-Power Beamwidth, Sidelobe Level, and beam pointing. It also has been studied the amplitude and phase errors of the two radiated modes which generate circular polarization. It is assumed that all correlated errors are being removed and that the remained errors are random, assuming to be normally distributed (Gaussian) with a zero mean and variance of σ^2 [58].

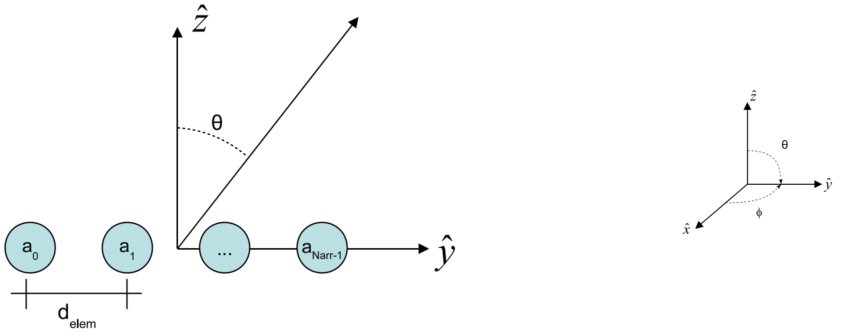

Figure 6.1: N_{array} elements antenna array

6.1.1 Gain Loss

In order to analyze the gain variation of an array with errors in the elements excitation amplitude and phase, an isotropic radiation element will be considered and therefore the array radiation intensity will be equal to the square of the Array Factor (AF). In a *broadside* linear array, the final directivity may be computed as:

$$D_0 = 4\pi \frac{|AF_{max}|^2}{\int_0^{2\pi}\int_0^{\pi}|AF\left(\theta\right)|^2 \sin\theta d\theta d\phi} = \frac{2|AF_{max}|^2}{\int_0^{\pi}|AF\left(\theta\right)|^2 \sin\theta d\theta} \tag{6.1}$$

An analytic method to compute the gain variation due to amplitude and phase errors is [59,60]:

$$\frac{G}{G_0} = \frac{1}{1+\sigma} = \frac{1}{1+\sigma_\delta^2+\sigma_\phi^2} \tag{6.2}$$

where σ_δ is the amplitude standard deviation and σ_ϕ is the phase standard deviation in radians. This expression assumes that arrays are large enough to apply the central limit theorem, which implies $N_{arr} > 10$. Fig. 6.2 illustrates the analytical array gain loss as function of the amplitude and phase standard deviations.

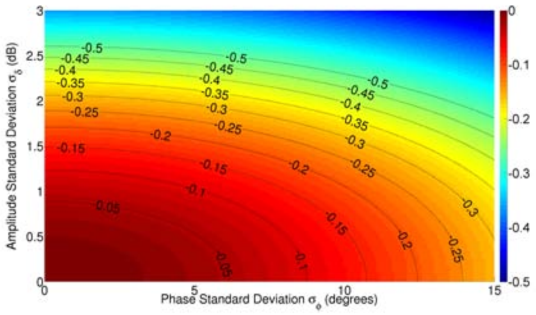

Figure 6.2: Theoretical Gain Loss against amplitude (σ_δ) and phase errors (σ_ϕ) in an array ($N_{array} > 10$)

To analyze the gain variation in arrays with a number of elements lower 10 and to validate the analytical model when the central limit theorem is applied, an statistical analysis has been done using different N_{arr} (2, 4, 8 and 16), with a *Monte Carlo method*. The process relies on computing the gain loss with a high number of random errors. For each possible amplitude and phase errors, the analysis has been:

- Fix amplitude and phase standard variation (σ_δ and σ_ϕ).
- Compute N_m=20000 times the gain variation by adding a random noise in the amplitude and phase.
- Compute the average gain loss for each error case.

Fig. 6.3 shows the average gain loss against amplitude- (σ_δ) and phase-errors (σ_ϕ) in four different array cases. The average gain variation seems to be independent of the array elements number, when it is larger than 10, and results similar to the obtained with the analytical method. In the case where the elements number is below 10, the theoretical model is not valid and differences can be observed, especially when N_{arr}=2 and N_{arr}=4.

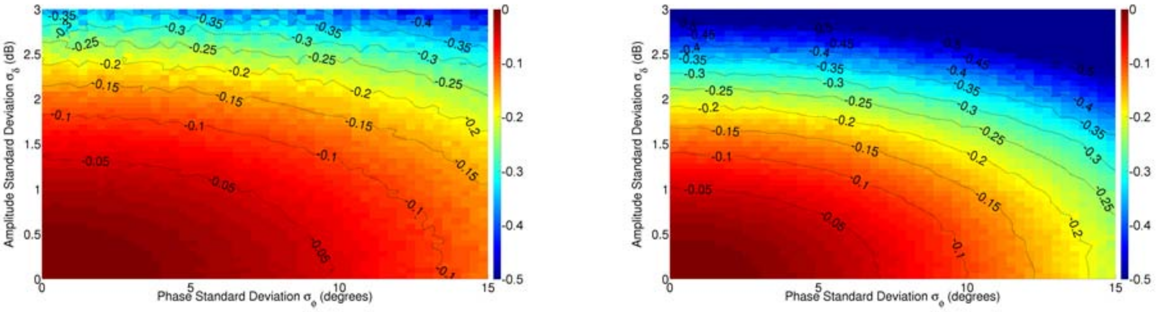

(a) Array Elements = 2 (b) Array Elements = 4

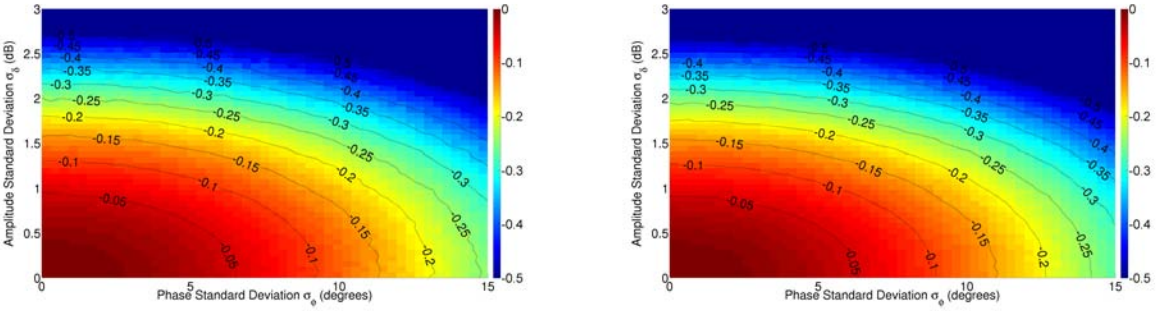

(c) Array Elements = 8 (d) Array Elements = 16

Figure 6.3: Average Gain Loss against amplitude (σ_δ) and phase (σ_ϕ) errors for different array elements number

6.1.2 Half-Power Beamwidth (HPBW) Error

In a broadside antenna array, the HPBW ($\Delta\theta_{-3dB}$) is proportional to the inverse of the electrical length, being analytically computed as:

$$\Delta\theta_{-3dB} \approx 0.88\frac{\lambda_0}{N_{arr}d_{elem}} \tag{6.3}$$

Using the *Monte Carlo* method, variations on the HPBW have been studied for 2, 4, 8 and 16 array elements with an elements distance (d_{elem}) of $\lambda_0/2$. It can be observed from the HPBW analytical method that increasing the array number of elements is translated into a narrower beamwidth. Then, the beam absolute variation due to errors is reduced. Fig. 6.4 illustrates the HPBW standard variation normalized for each array, presented as percentage. For a short number of elements, it can be seen a large influence of the amplitude errors. By the other hand, it can be seen how when the beamwidth is reduced (large number of elements), the HPBW variation tends to be smaller. Like happened with the beam pointing error, in large arrays, the HPBW variation is reduced due to the lower weight of each elements amplitude and phase when computing the total beamwidth. This is translated into a lower influence of each elements feed errors. It can be seen how in the 2 elements array the maximum beamwidth standard variation is 30% while in the 16 elements array the maximum variation is only up to 8% with the same amplitude and phase errors.

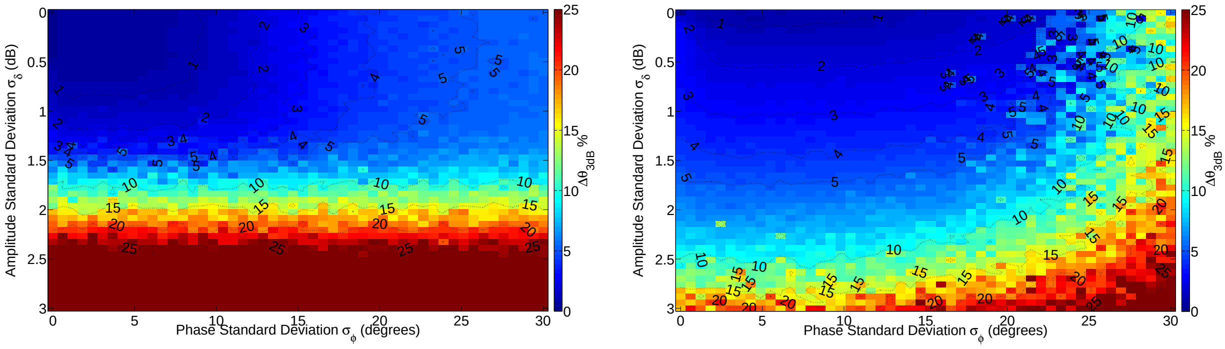

(a) Array Elements = 2 (b) Array Elements = 4

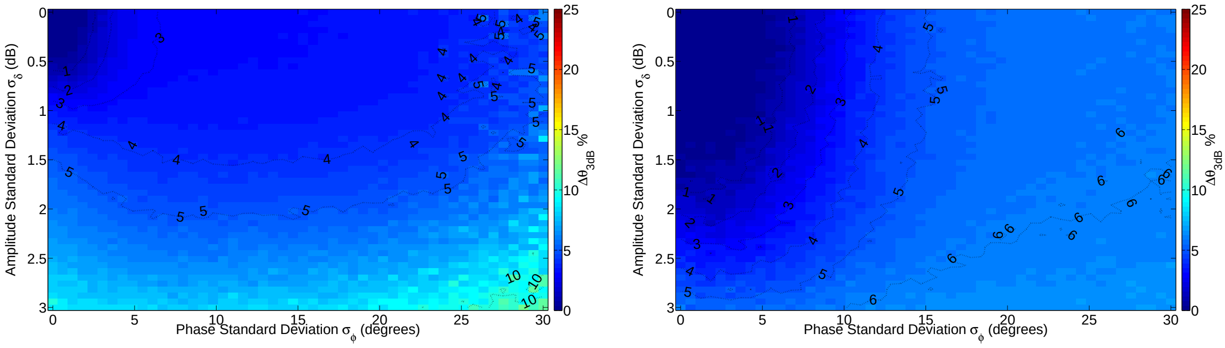

(c) Array Elements = 8 (d) Array Elements = 16

Figure 6.4: Percentage HPBW standard variation normalized to $\Delta\theta_{-3dB}$ for different array dimensions

6.1.3 Beam Pointing Error

Considering a linear array fed with a uniform amplitude distribution and constant phase, and with a number of elements large enough to apply the central limit theorem, the variance of the beam pointing deviation may be analytically computed as [61]:

$$\sigma_{\theta}^{2} = \sigma_{\phi}^{2} \frac{\sum_{n=1}^{N_{arr}} a_n^2 \left(\frac{n}{d_{elem}}\right)^2}{\sum_{n=1}^{N_{arr}} a_n \left(\frac{n}{d_{elem}}\right)^2} \Rightarrow \sigma_{\theta}^{2} = \frac{12}{N_{arr}^{3}} \sigma_{\phi} \tag{6.4}$$

Fig. 6.5(a) illustrates the analytic beam pointing standard deviation for those cases when the elements number is 2, 4, 8 and 16. In this study, the distance between elements (d_{elem}) has been considered to be $\lambda_0/2$. Fig. 6.5(b) illustrates the beam pointing standard deviation computed using a *Monte Carlo* method (N_m=20000). In the analytical analysis it is not observed any influence from the amplitude standard variation, being then represented only the variation as a function of phase errors. The analytical error analysis is precise for all the cases when the phase standard variation is low. If the phase error increases, the concordance between the analytic- and statistical-methods remains good for those arrays with a large number of elements but is reduced for a short N_{arr}. Looking at the phase arrays theory, the pointing direction can be computed as the average slope resulting from all phases. Then, it seems logical that when the number of elements is large, the effect of a single element phase error is lower than the effect when the number of elements is short, as happens in the analysis. It also should be considered the fact that an array with large number of elements has a narrower beamwidth than an array with shorter number, being pointing errors more critical .

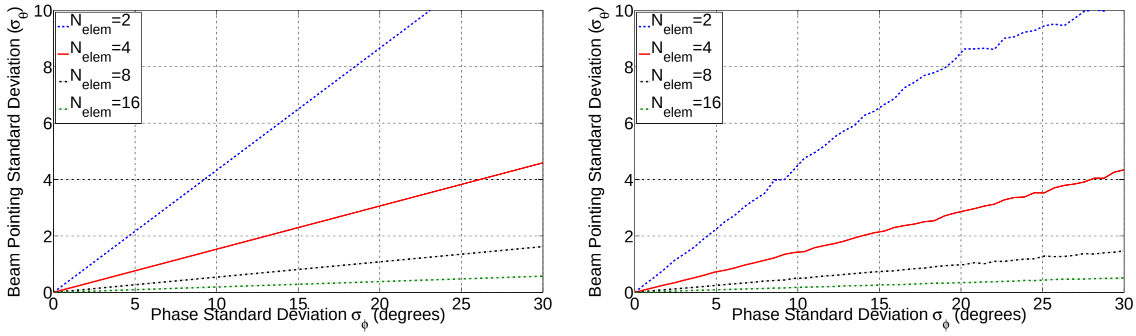

(a) Analytical Method

(b) *Monte Carlo* Method

Figure 6.5: Array Beam Pointing standard deviation

6.1.4 Peak Sidelobes Error

In a uniform distributed linear array antenna, the Sidelobe Level (SLL) is computed as:

$$SLL \approx N_{arr} \left| sin\left(\frac{3\pi}{2N_{arr}}\right)\right| \Longrightarrow \underset{\mathrm{N} \to \infty}{\mathrm{SLL}} = 13.2dB \tag{6.5}$$

being 13.2dB when the number of elements tends to infinity.

An statistical analysis of the SLL has been done for arrays with 4, 8 and 16 elements. The 2 elements array is characterized for not having Sidelobes. Fig. 6.6 shows the average SLL error in dB calculated using *Monte Carlo* method. It can be seen a strong influence of the phase error. The error is reduced when the number of elements increases.

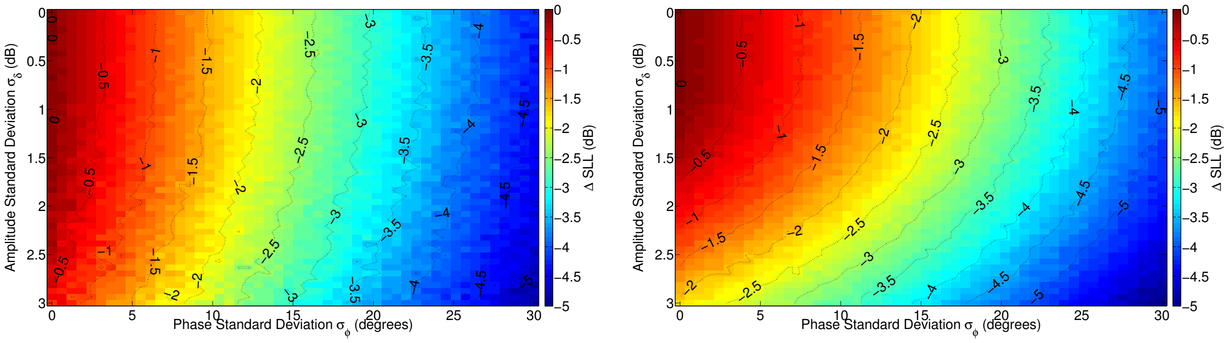

(a) Array Elements = 4

(b) Array Elements = 8

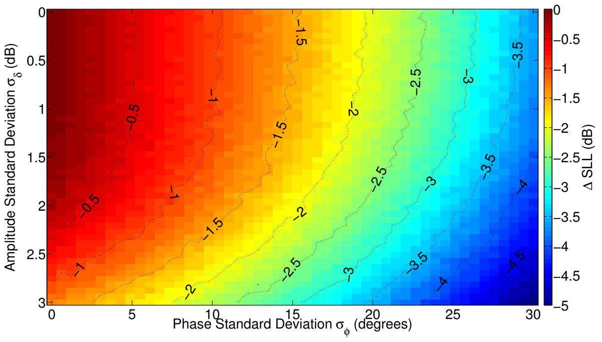

(c) Array Elements = 16

Figure 6.6: Average SLL error for different array dimensions

6.1.5 Axial Ratio Error

The axial ratio (AR) is computed as the ratio between the two principal axes of the polarization ellipse generated by the radiated field two orthogonal linear components. In optimum circular polarization case defined by an $AR = 0dB$, the amplitude of the two components have to be the same ($E_{x0} = E_{y0}$) and the two components must have a time-phase difference of odd multiples of 90° ($\Delta\phi = \phi_{E_{x0}} - \phi_{E_{y0}} = 90^o$). The appearance of errors in the modes amplitude and phase degrades the quality of the circular polarization

The Axial Ratio is computed as:

$$AR = \frac{OA}{OB} \qquad 1 \leq AR \leq \infty \tag{6.6}$$

where

$$OA = [\tfrac{1}{2}\{E_{x0}^2 + E_{y0}^2 + [E_{x0}^4 + E_{y0}^4 + 2E_{x0}^2E_{y0}^2 \cos 2\Delta\phi_{pol}]^{\frac{1}{2}}\}]^{\frac{1}{2}}$$

$$OB = [\tfrac{1}{2}\{E_{x0}^2 + E_{y0}^2 - [E_{x0}^4 + E_{y0}^4 + 2E_{x0}^2E_{y0}^2 \cos 2\Delta\phi_{pol}]^{\frac{1}{2}}\}]^{\frac{1}{2}} \tag{6.7}$$

$$\Delta\phi_{pol} = \phi_{E_{x0}} - \phi_{E_{y0}}$$

The amplitude and phase errors of the orthogonal fields E_x and E_y affect the final AR. An statistical study has been done using a *Monte Carlo* Method with $N_m = 20000$ samples. Fig. 6.7(a) shows the AR standard variation (σ_{AR}) as a function of the amplitude and phase standard variations. Fig. 6.7(b) illustrates the probability to have circular polarization (AR $<$ 3dB) depending the errors variation.

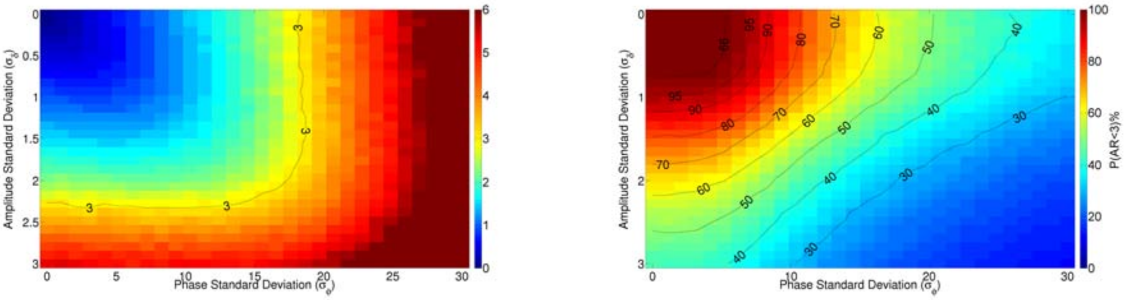

(a) AR standard variation

(b) Probability to have an $AR < 3dB$

Figure 6.7: Axial Ratio statistical study as a function of the radiated fields amplitude and phase standard variation

Fig. 6.8 shows the probability to have circular polarization when there is only amplitude errors and only phase errors. It is seen that in order to have an Axial Ratio lower than 3dB in the 99% cases, the maximum amplitude standard deviation allowed is 0.8 dB while the maximum phase standard deviation is 6 degrees. This values reflect the high sensitivity when trying to create a circularly polarized wave.

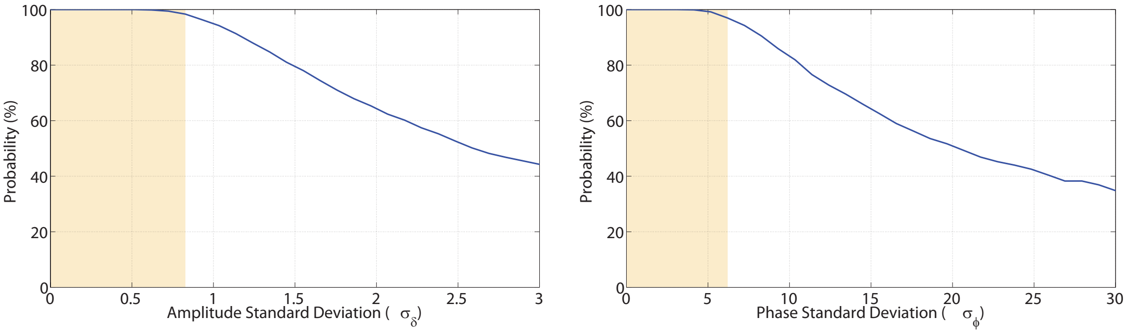

(a) Probability with only σ_δ

(b) Probability with only σ_ϕ

Figure 6.8: Probability to have Circular Polarization when only one error is present (σ_δ or σ_ϕ)

6.1.6 Prototypes Fabrication Tolerances

The different CPW Patch prototypes presented in this thesis, have been tested statistically with different fabrication tolerances in order to set the most appropriate manufacturing process. Fig. 6.9 illustrates the antenna array operating at Ka-band with RF-MEMS. This array feed network is the same than the used with the Hard-Wire (HW) antennas at the same frequency band. The feed network used in the V-band applications has the same structure but being scaled to the antenna resonant frequency.

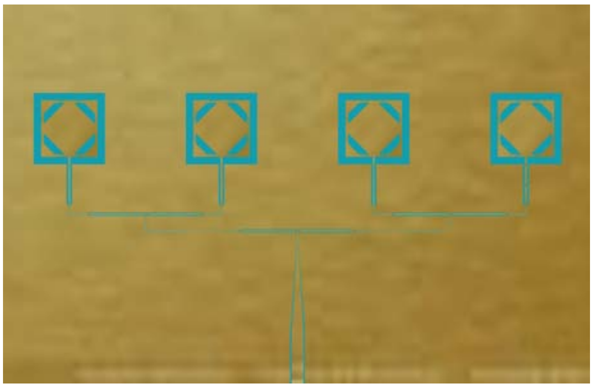

Figure 6.9: 4 × 1 CPW Patch Antenna Array

A previous step before analyzing the different fabrication antenna tolerances is to analyze the absolute dimensions of the antenna. Because the coplanar nature of this antenna, the tolerances will be divided in two groups:

- CPW strip: which references to the capability to leave metallic material on the substrate, used for example in the transmission line strip.
- CPW gap: which references to the capability to remove metallic material on the substrate, used for example in the transmission line gaps or in the patch surrounding slot

Checking the different designs, can be seen the existence of fabrication tolerances limitations given by the lowest dimensions in the prototype. These limitations will be divided between the feed network and the base element, knowing that the final decision will have to consider both of them. Table 6.1 summarizes the minimum dimensions required for both designs. It can be clearly observed that the use of CoPlanar Waveguide have a strong dimensional limitations. A laser or photoplotter fabrication precision of $25\mu m$ could be acceptable to fabricate the transmission line strip at Ka-band but not for the gap.

	Feed		Element	
	Strip	Gap	Strip	Gap
Ka-band	$50\mu m$	$10\mu m$	$50\mu m$	$300\mu m$
V-band	$15\mu m$	$5\mu m$	$10\mu m$	$5\mu m$

Table 6.1: CPW Patch Antenna minimum dimensions required

Base element: The tolerances study realized with the single element have been regarding the antenna axial ratio. An error has been added to the different parameters of the antenna and the

AR at the center frequency has been computed in 500 iterations for each error magnitude studied. Because the unknown statistical distribution type of the errors, these have been considered to be rectangular with zero mean and the studied tolerances. The analysis have been done using the finite element method Ansoft HFSS simulator.

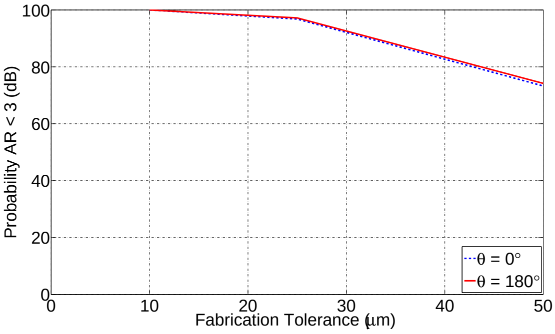

Figure 6.10: Ka-band CPW Patch antenna fabrication tolerances to have CP

Fig.6.10 shows the probability that the axial ratio remains lower than 3dB for the different fabrication tolerances in the Ka-band design. It can be seen that to have a probability higher than 99%, the fabrication tolerances in the Ka-band design are $10\mu m$. The fabrication tolerances of the V-band design are given by the design dimensions.

Array antenna: Concerning the tolerances in the feed networks, the standard deviation of each port amplitude and phases have been studied. Because the dimensional limitations, the study has been realized independently between the strip errors and the gap errors. The analysis has been done with the *Monte Carlo* method ($N_m = 10000$ iterations) at the center frequency in the Agilent ADS Simulator. Fig. 6.11 illustrates the amplitude standard deviation computed for the different fabrication tolerances at Ka- and V-band. Fig. 6.12 shows the phase standard deviation or the same fabrication tolerances.

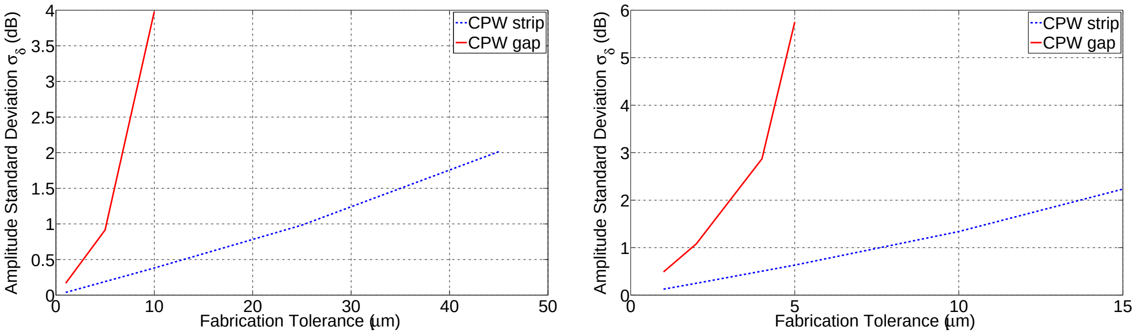

(a) Ka-band prototype

(b) V-band prototype

Figure 6.11: Amplitude standard deviation for the CPW Patch feed network

In that cases, the fabrication tolerances chosen may differ depending the amplitude and phase standard deviations allowed in the design, which are fixed by the antenna requirements and the tolerances study previously presented. As an example, in a 4 elements array were the desired gain loss should not be higher than 0.25 dB, the maximum amplitude standard deviation should be 2.5 dB which at Ka-band would be translated into a fabrication tolerances lower than $10\mu m$ and at V-band lower than $3\mu m$. In the case of the phase standard deviation, the accepted value would be 15 degrees which would be a similar fabrication tolerances values than for the amplitude case. This results lead to use high precision fabrication processes, being microfabrication a good candidate.

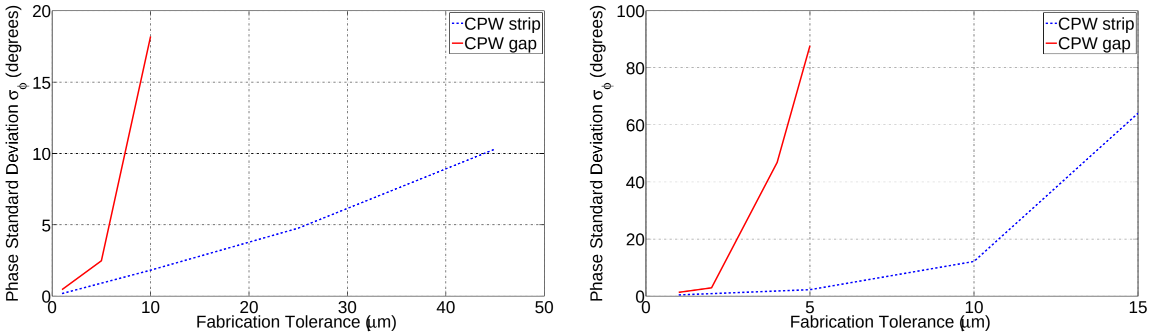

(a) Ka-band prototype

(b) V-band prototype

Figure 6.12: Phase standard deviation for the CPW Patch feed network

6.2 Fabrication Techniques

The objective of the microfabrication process is to manufacture a device with a fabrication resolution between 1 and 2 μm [62]. The manufacturing depends on three types of processes: addition of material (*deposition*), removal of material (*etching*) and modification of material. Defined areas of the substrate must be protected from or exposed to these processes. These areas make up the pattern, resulting into the so-called patterned substrate. The process to define these areas is called lithography. Many fabrication tools and techniques can be used, and they are chosen depending on the materials used and on the complete fabrication plan. The use of a certain technique in a multilayer fabrication process could affect negatively to a finished layer.

In this section, a brief introduction to the different microfabrication processes used in this thesis are presented.

6.2.1 Material Deposition

The material deposition is called to the act of applying a thin film to a substrate. The thin film concept may be relative, but in general is referred to a magnitude order of few micrometers, while the term very thin film stays for a magnitude order of hundreds of Angstrom. The deposition techniques may be classified in chemical or physical . In this thesis, the deposition techniques (Fig. 6.13) are only physical, being used under vacuum environment:

(a) Thermal/ E-gun Evaporation System (SC4500)

(b) Sputter deposition (CVC 601)

(c) Spinning Hood

(d) Electroplating Hood

Figure 6.13: Material Deposition Techniques

Thermal Evaporation: uses an electric resistance to melt the material placed into a ceramic evaporator known as "boat". The obtained vapor travels directly to the target (substrate) where it is condensed back to a solid state (Fig. 6.13(a)).

E-beam Evaporation: has the same evaporation principle than the thermal evaporation process but the material is supplied into crucibles (refractory container) and is heated by an electro gun source (Fig. 6.13(a)).

Sputter: is a deposition method that bombards ion or atoms to the material source resulting in sputtered atoms. These sputtered atoms move away from the source in straight line and impact energetically onto the substrate. The sputtering gas is often an inert gas such as Argon (Ar). The amount of different parameters that control the sputter deposition make this process very complex (Fig. 6.13(b)).

Spinning: is the deposition method for viscous materials such as resists, polymethyl methacrylate (PMMA), Benzocyclobuten polymer (BCB) or other organic dielectrics. The process consist of leaving the substrate on a spinner. A certain quantity of material is placed on the substrate and the spinner is activated. Material parameters such as viscosity or solvent evaporation rate, or process parameters such as spin acceleration, spin speed or spinning time will affect to the uniformity and thickness of the deposited material. It is common to do a *soft bake* which is used to drive the solvent from the material (Fig. 6.13(c)).

Electroplating: is a process in which metal ions in a solution are moved by an electric field to coat a conductive object with a thin layer. In this thesis, electroplating has been used to build up thickness of desired gold areas of the wafer. The amount of electrical current used indicates the amount of metal deposited in the substrate. Because the electrodes are normally connected at the edges of the wafer, this process shows some thickness non-uniformity between the center and the border (Fig. 6.13(d)).

6.2.2 Lithography

The lithography process consist of defining the pattern where the manufacturing processes will be applied. This pattern definition takes place in a thin layer of polymeric material (*resist*) that is coated on the substrate. The resist is modified so it remains in some areas and is removed in others by a two-step process:

Exposure: consists into 'illuminate' the resist with an incident radiation or particles such as light, x-ray, electrons or ions. The exposure causes physical or chemical change in the resist. The method of exposure may differ from direct write or masked exposure. Direct write consist of focusing electrons or ions into a small diameter spot which is scanned directly onto the resist (serial exposure process). The masked exposure (Fig. 6.15(a)) consist of image light or x-rays onto the resist through a patterned mask (parallel exposure process). The microfabricated devices presented in this thesis have been using masked exposure with the EV620 (Fig. 6.14(b)), that provides a fabrication tolerances of $1\mu m$.

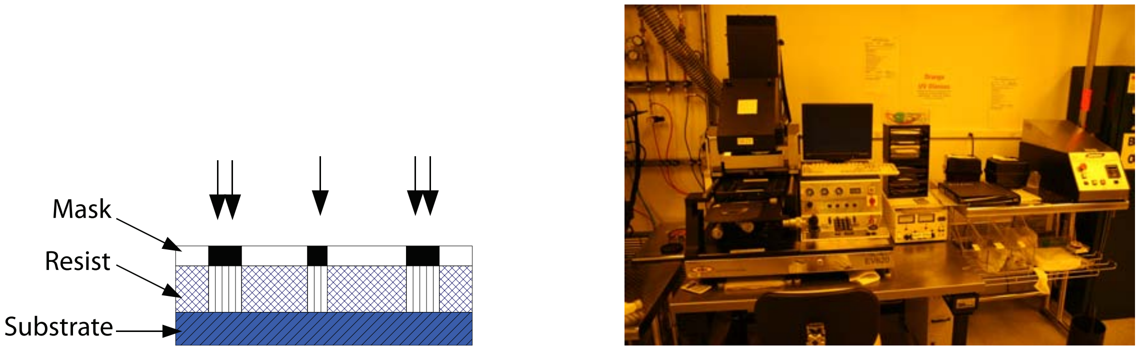

(a) Principle (b) EV620 Contact Aligner

Figure 6.14: Masked Exposure Process

Development: consists into applying a base or solvent onto the exposed resist to remove the undesired area (Fig. 6.15(a)). The developing process can be done manually or automatically with the use of the Hamatech-Steag Wafer Processor (Fig. 6.15(b)). In general, there are two types of resists:

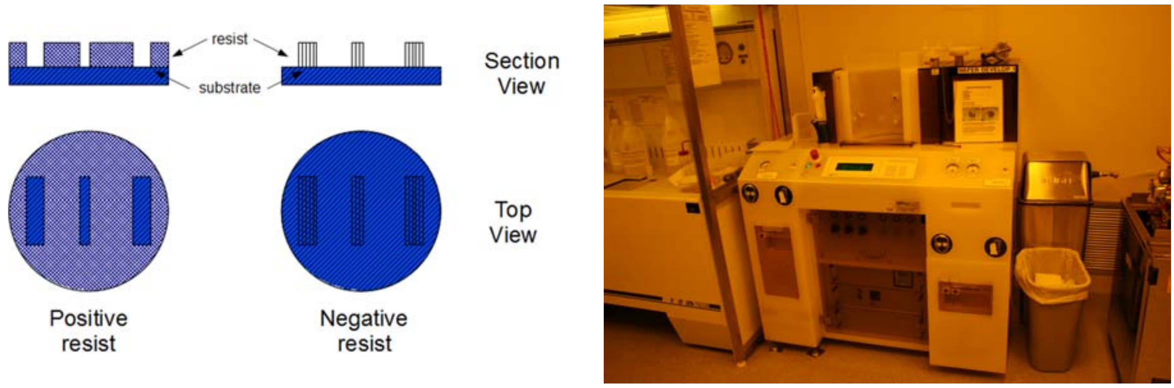

(a) Principle

(b) Hamatech-Steag Wafer Processor

Figure 6.15: Development Process

- Positive: the exposed areas become more soluble in the developer, thus they are removed by development.
- Negative: exposed areas become less soluble in the developer, thus they remain after development.

6.2.3 Etching

The etching process consist of the material removal process. By lithography, parts of the wafer are protected from the etching by a resistive material, living unprotected areas which will be etched. When the etching process is done, the remaining resist has to be removed. The etching can be divided in two main groups:

Wet-Etching: consist of the use of liquid (”wet”) etchants. The wafer is immersed in a bath of etchant, which is selected depending the material that is going to be removed. In this thesis, gold (Au) etchant, Chrome (Cr) etchant and hydrofluoric acid (HF) to remove Ti have been used. Fig. 6.16 illustrates a gold etching process in a quartz wafer. Can be seen how the gold is etched selectively living parts of the wafer with gold and parts without.

Dry-Etching: consists into use plasma (”dry”) as etchant. The plasma is produced from a process gas using a high frequency electric field. The source gas for the plasma usually contains small molecules rich in chlorine or fluorine. A plasma containing oxygen is used for stripping of photoresist and other organics. This process requires a vacuum environment with a pressure between 0.1 and 5 Torr. In this thesis, two different dry-etching tools have been used (Fig. 6.17): Fluorine based gas (Oxford 81) and Oxygen (Glen 1000).

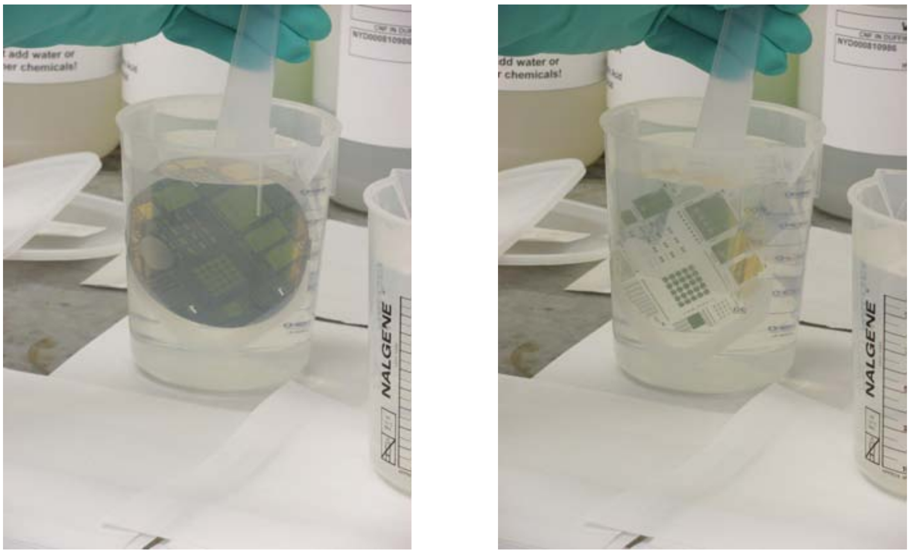

(a) Initial instant (b) Final instant

Figure 6.16: Gold Etching example in a quartz wafer

6.2.4 Auxiliar Microfabrication Processes

Besides the main fabrication processes, there are other fabrication tools that are useful in some cases:

Dicing Saw : is a tool capable of dicing silicon and all types of glasses (Fig. 6.18(a)). It is characterized to handle 6 inch substrates with a thickness of up to 1.25 mm. It is very useful for those devices that need to be separated from the others in the wafer, such as the devices manufactured under this thesis topics.

Critical Point Dryer: is a tool typically used after the release of Radio-Frequency Microelectromechanical Systems (RF-MEMS) devices in order to prevent alterations in the device structure (Fig. 6.18(b)). The critical point drying is a gentler method to dry the device without causing any damage. It consist of increasing the pressure and temperature of the substrate till the critical point is passed. Then, the density of the liquid and the density of the gas are the same and the surface tension of the liquid at the point at which it changes from liquid to gas it is eliminated.

Wire Bonder: The wire bonder is used to inter-connect at micron scale pads or metal areas. A wedge-wedge ultrasonic type wire bonder has been used with 1.25 mil aluminum wire to interconnect the parallel ground planes in CPW transmission lines in order to assure the same potential at each side of the line.

(a) Oxford 81 (b) Glen 1000

Figure 6.17: Dry-etching tools

(a) Dicing Saw (b) Critical Point Dryer

Figure 6.18: Auxiliar tools

6.2.5 Mask Generation

The lithography in masked exposure technique requires the fabrication of the mask where the pattern will be printed. In multilayer devices, a mask for each layer has to be drawn and manufactured. The mask may be drawn in any CAD program, using in this thesis L-Edit from Tanner EDA.

The use of a single layer in microfabrication is not usual, being more general the fabrication of multilayer devices. The fabrication of a single layer mask is considered as a particular case of the multilayer.

The mask consists of a glass substrate coated with a film with the pattern, which normally is formed with Chromium (Cr). The resolution of the masks maker is around $1\mu m$. The substrate choice has to take into consideration the thermal expansion of the glass and its transmission at the exposure wavelength. The types of glass more used are Soda-lime, Borosilicate and Quartz. The worst case is soda-lime which gives a $1.2\mu m$ error across a 5 inch mask for every 1^oC variation in temperature but is enough for many applications and the cost is much more lower than the others.

Chapter 7

Experimental Prototypes and results

This chapter is focused on the different designed prototypes microfabrication process and measurements. The polarization reconfigurable CPW patch antenna has been manufactured in single element version and in array version for both RF-MEMS switches integrated and HW designs. The antennas microfabrication has been done together with the Department of Electrical and Computer Engineering (ECE) from Utah State University (USU) at the Cornell NanoScale Science & Technology Facility (CNF) from the Cornell University. From the experience obtained in this fabrication process, the main ideas in the 4-Qdime antennas manufacturing processes are presented.

This chapter also includes the manufactured prototypes measurement results. The individual RF-MEMS switches have been RF characterized up to 50GHz. Then, the HW CPW Patch antenna at Ka-band and at V-band have been measured using different measurement set-ups.

7.1 Prototypes Fabrication

7.1.1 HW CPW Patch antenna

The Ka- and V- band HW prototype fabrication process consists of a single layer process, having no more difficulty than the one of the fabrication processes themselves. Fig. 7.1 show the mask used to fabricate the HW antennas at CNF. It can be seen four different single elements and four arrays operating at Ka-band, and six groups of four different configured antennas at V-band. Both antennas have been printed on the same $500\mu m$ thick quartz wafer. The fabrication process can be summarized in the following steps:

- Deposition of the seed layer, a very thin gold layer (3000Å)
- Design pattern with lithography.
- Electroplating process to grow up the seed layer to a final thickness of $4\mu m$.
- Gold wet-etching to remove the undesired metallization.
- Wafer dicing to release the different HW antennas

Fig. 7.2 illustrates as an example, two microscope images corresponding to the HW CPW Patch antennas designed to operate at V-band.

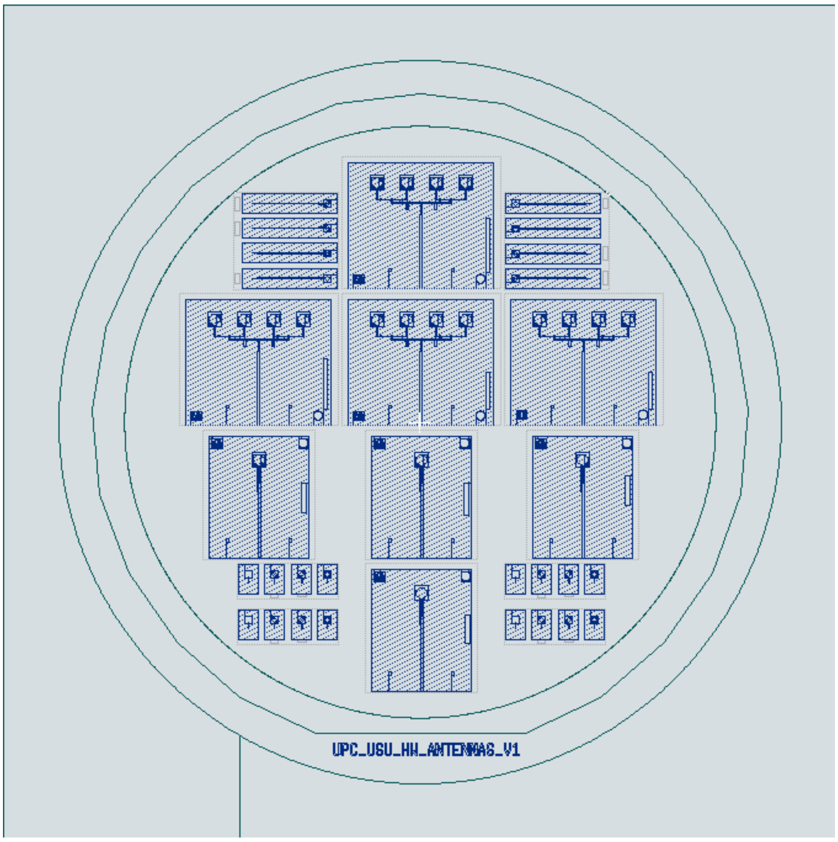

Figure 7.1: Single layer mask set for a 5 inches wafer

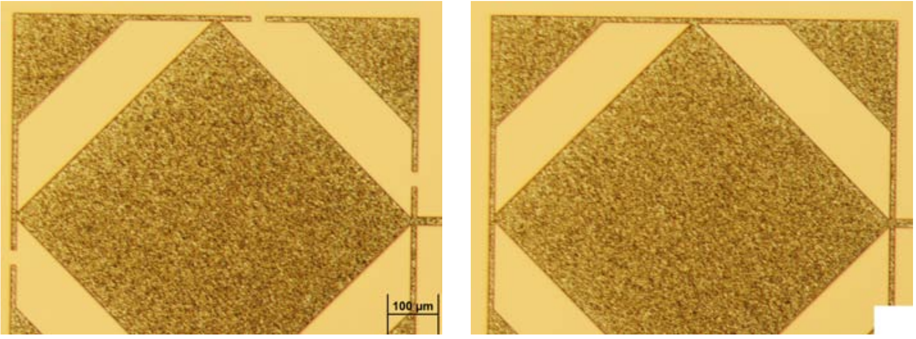

(a) CP

(b) LP

Figure 7.2: V-band HW CPW Patch microscope images

7.1.2 RF-MEMS-Integrated CPW Patch Antenna

The RF-MEMS-Integrated CPW Patch Antenna fabrication process requires a set of 6 masks and more than 170 fabrication steps. This section summarizes them.

7.1.2.1 Mask Generation

The mask set designed to fabricate the antennas is presented in Fig. 7.3. Together with the CPW Patch antennas, it can be seen other switches-integrated antennas and some groups of RF-MEMS switches to be tested separately. All of them have been fabricated together in the same wafer to optimize space and costs. The final design is in a limited area confined by the wafer dimensions. A margin should be left free of elements because they could be damaged while manipulating during the microfabrication processes. Another think to have into consideration is the dicing process. The dicing lines should follow a pattern if it is possible to make it easy, and in the case that no pattern is possible, the number of times the wafer has to be taken off from the dicing tool should be minimized.

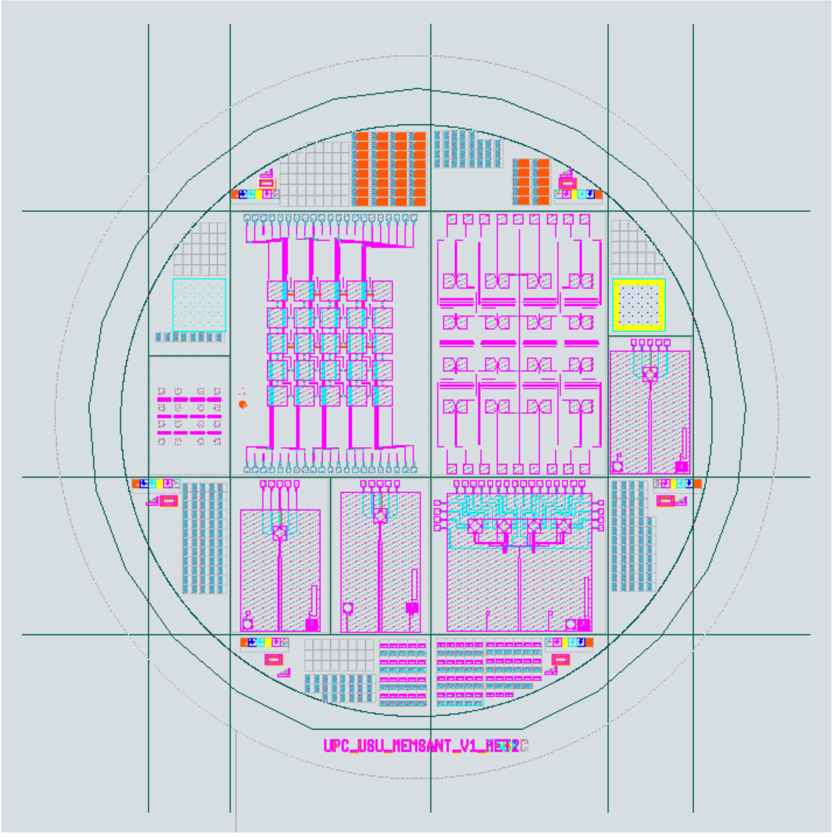

Figure 7.3: 6-Layers mask set for a 5 inches wafer

Fig. 7.4 shows in more detail four of the six masks used for the polarization reconfigurable CPW Patch antenna fabrication process. The high resistivity layer , thin film metal layer and thick film metal layer masks are printed in positive to be used with positive photo-resist, while the sacrificial layer mask is printed in negative to be used with negative photo-resist. The different fabrication processes are presented later in this thesis.

To draw the mask set, some extra devices have been added, that will help during the fabrication process:

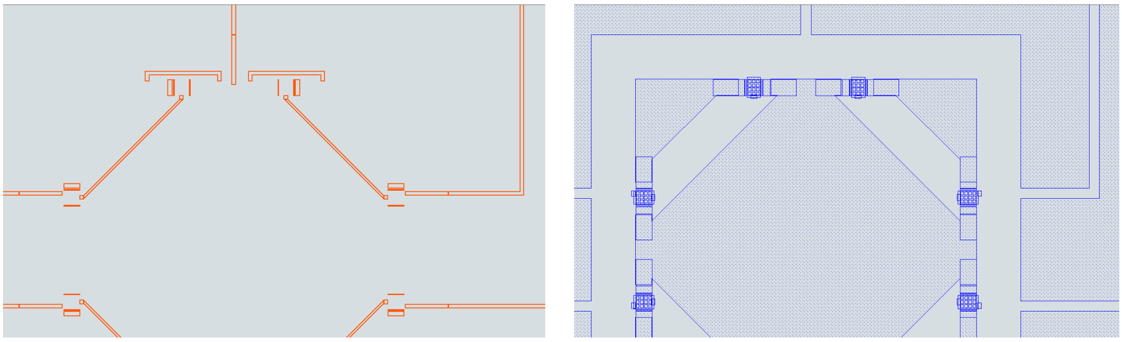

(a) High Resistivity Layer (b) Thin Film Metal Layer

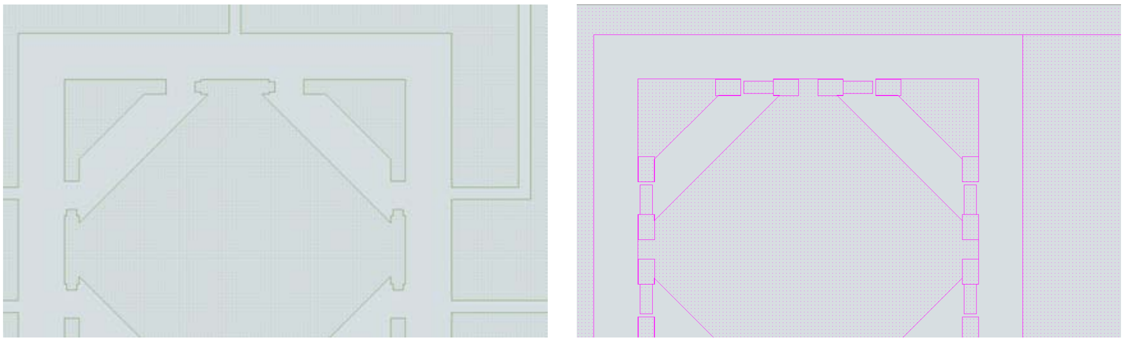

(c) Sacrificial Layer (d) Thick Film Metal Layer

Figure 7.4: RF-MEMS switches integrated polarization reconfigurable CPW Patch antenna fabrication masks details

Align marks: are used to accomplish a good alignment between layers. The marks have to be clearly visible to the next layer fabrication step. The marks are placed in different zones of the wafer and if it is possible symmetrically to facilitate the alignment in the contact aligner. Fig. 7.5 shows the 6 layer mask set alignment marks used. It can be seen how each layer has two align marks, one to align with the lower layer and one with the higher layer.

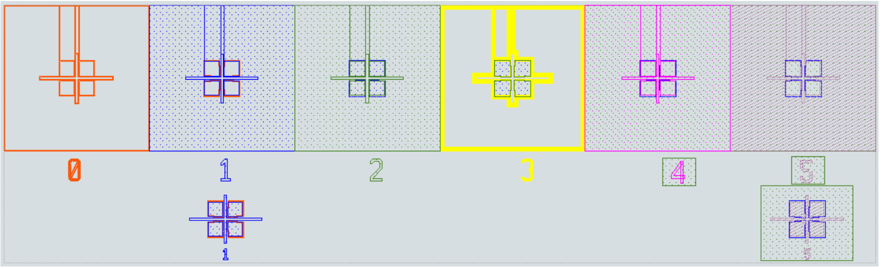

Figure 7.5: Align marks

Lithography Marks: are used to control the quality of the lithography process (exposure and development) together with a control of the wet-etching. The lithography marks used in this thesis (Fig. 7.6) consist of different width lines placed in rectangular shape and separated with different distance. These marks are checked in the microscope and it can be clearly seen if for example there is an over-exposition or two long wet-etching.

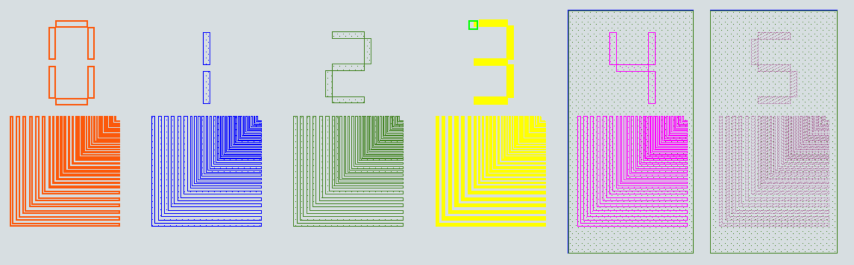

Figure 7.6: Lithography marks

Thickness Monitor: is used to monitor each layer thickness. With the use of a profilometer, the surface characteristics at micron scale can be measured. The thickness monitor (Fig. 7.7) consist of creating steps between layers so the thickness may be measured. It is recommended to place some monitors along the wafer for those deposition processes that are not so uniform.

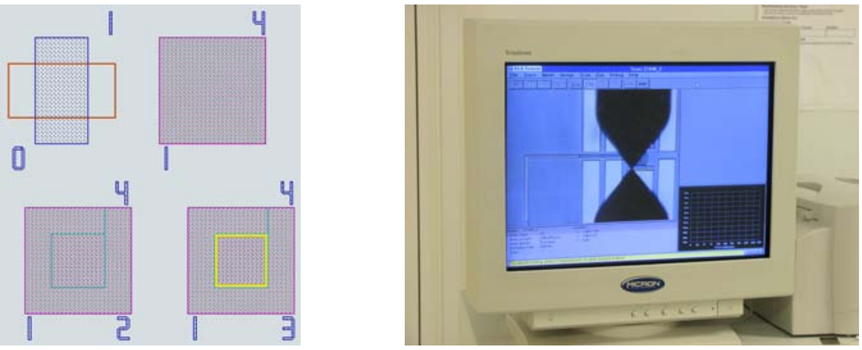

(a) Mask layout

(b) P10 Profilometer

Figure 7.7: Thickness monitor

MEMS Structural Tests : may be used when devices with RF-MEMS are fabricated. The cantilever-beam in Fig. 7.8(a) is a test to measure the residual stress gradient at cantilevers with different length [63]. The bent-beam shown in Fig. 7.8(b) is a test used to evaluate the residual strain of the switch [64].

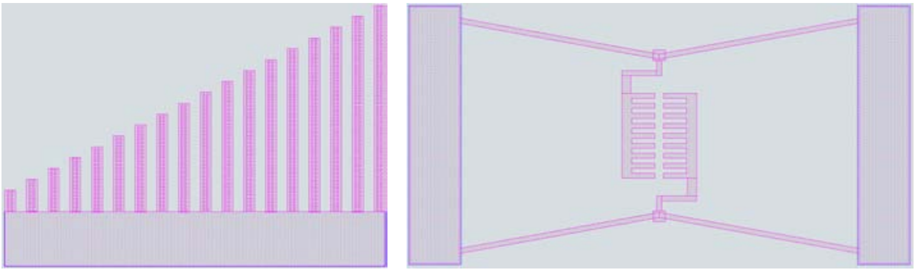

(a) Cantilever Beam Monitor

(b) Bent Beam Monitor

Figure 7.8: MEMS structural tests

7.1.2.2 Antenna Fabrication Process

The Ka-band RF-MEMS-integrated polarization- and pointing-reconfigurable CPW Patch antenna presented in the previous chapters (Fig. 7.9) have been fabricated in the same wafer, thus following the switches microfabrication process. Each RF-MEMS switches manufacturer has its own fabrication process as presented in [16] that may differ a little bit one from an other.

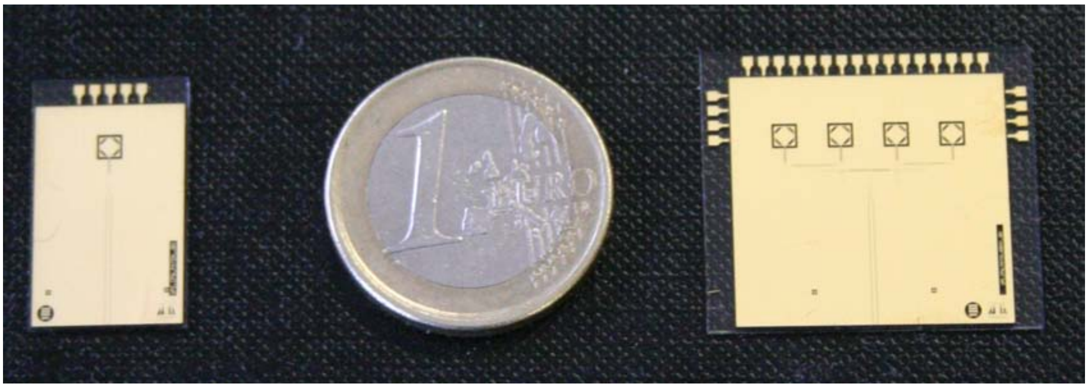

(a): Single Element Antenna (b): Array Antenna

Figure 7.9: RF-MEMS integrated CPW Patch antennas manufactured

Because the antenna and the feed network are placed in the same layer they don't have much fabrication difficulty more than the one related to the fabrication tolerances at Ka-band frequencies. Three fabrication critical points are:

- **RF-MEMS switch fabrication**. It is the most complex process of this antenna. The RF-MEMS switches fabrication require a 6-layers process and a final *Critical Point dryer* process. The fabrication yield is low and it is under developing to be improved.
- **RF-MEMS activation bias lines**. In order to activate or deactivate the RF-MEMS switches, a high resistance lines have to be placed from outside the antenna to the switches. Because the antenna architecture, this lines have to cross through the ground plane. For that reason, a set of *tunnels* have been built to contain the bias lines avoiding short-circuit with the ground plane.
- **CPW lines air-bridges**. The necessity to have equal potential at each side of a CPW ground planes to avoid the excitation of odd-modes, has been translated into the necessity to connect both sides with an air-bridge. This air-bridge can be done by air-bonding or it can be fabricated in the microfabrication process like has been done in this design

A $500\mu m$ thickness quartz wafer has been used as a substrate. The antenna fabrication consists of more than 170 steps, that can be summarized as:

High Resistivity Layer The high resistive lines required to feed the switches bias pad has been done with TaN deposited under sputtering process. The resistance desired is between $2k-10k\Omega/sqr$.

The RF-MEMS switch also requires some high resistance areas such as the square stoppers used to avoid DC short-circuit between the switch cantilever and the bias pad. Fig. 7.10 shows an example of the high resistivity layer for one of the MEMS and its bias lines. Other high resistivity lines are connecting equal DC voltage parts in order to avoid charges that can damage the switches when turned ON. Dry-etching with CF4 is used to remove the non-patterned parts.

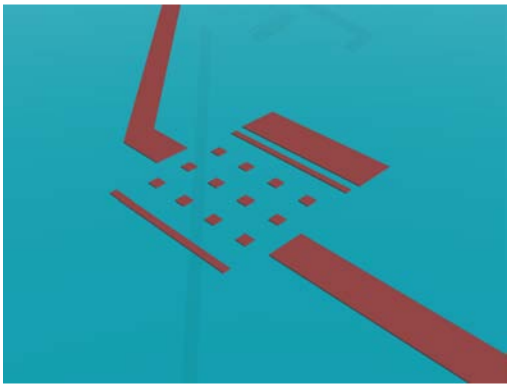

Figure 7.10: RF-MEMS high resistivity layer

Thin Film metallization layer A very thin film (3000Å) of gold is being patterned. The gold is deposited by evaporation together with an initial chromium layer (160Å) which is used to give more additivity between the quartz glass and the gold. Fig. 7.11(a) illustrates the switches activation pad. It can be seen how the pad is DC isolated from the high resistivity stoppers that are a little thicker. In Fig. 7.11(b) it is presented how the high resistive lines are isolated from the ground plane. Finally, Fig. 7.11(c) shows the bases of what will be the air-bridge used to connect both CPW ground planes. The removal process is done with wet-etching, being first etched the gold and then the chromium with the respective etchants.

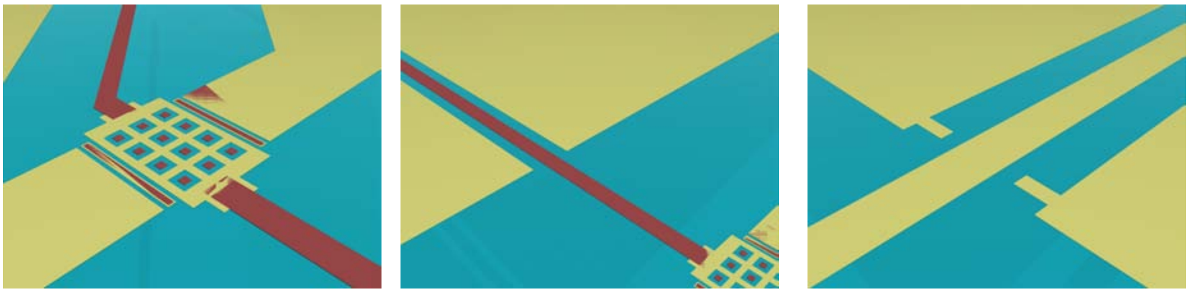

(a) RF-MEMS (b) Bias lines tunnel (c) Air-bridge

Figure 7.11: Very thin film metallization layer

Sacrificial Layer The sacrificial layer represents all the volume that will have air in a middle layer, like the zone under the switch cantilever (Fig. 7.12(a)), the resistive lines tunnels (Fig. 7.12(b)), under the air-bridge (Fig. 7.12(c)). The sacrificial layer consist of PMMA and has been deposited by spinning in two steps to achieve the desired thickness of $1\mu m$. Because PMMA organic nature, it can not follow a normal lithography process because it would be effected by the resist developer. Then, a very thin film (530Å) of titanium (Ti) is being evaporated onto the PMMA and patterned with the lithography process. The undesired titanium areas are removed by wet-etching with Hydrofluoric Acid (HF) and the undesired PMMA is removed by dry-etching with oxygen. Once the PMMA has been removed, the remain titanium is stripped with HF again, leaving the device aerial zones full of PMMA as illustrated in Fig. 7.12. The final patterned sacrificial layer will be removed at the end of the fabrication process.


(a) RF-MEMS (b) Bias lines tunnel (c) Air-bridge

Figure 7.12: Sacrificial layer

RF-MEMS dimples In the RF-MEMS switch design, a couple of dimples hang from the bottom of the cantilever. These dimples are responsible to contact the cantilever and the contact pad. The dimples are fabricated creating small holes in the sacrificial layer without breaking through the whole layer. At the next fabrication step, the holes will be filed of gold (Fig. 7.13).

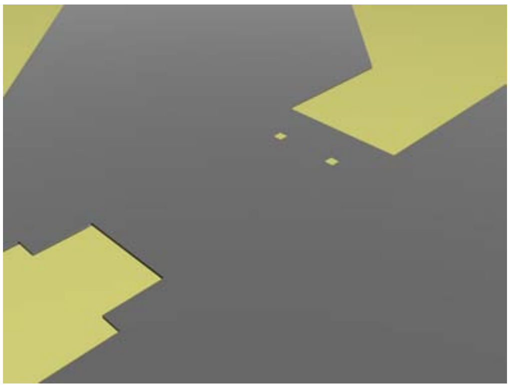

Figure 7.13: RF-MEMS dimples

Thick Metallization Once all the aerial zones have been defined and filled with PMMA, it is required to create the top metal parts. Initially there is a very thin film (2000Å) of gold deposited by evaporation which is called the *seed layer* followed by a pattern of the top metal part. Then, the seed layer is grown up to a thickness between $4-5\mu m$, with an electroplating process using a gold solution. Fig. 7.14 illustrates the antenna details with the top layer on. It can be seen how the RF-MEMS switch cantilever is created, how the tunnels have been closed on top and how the air-bridge has been connected.

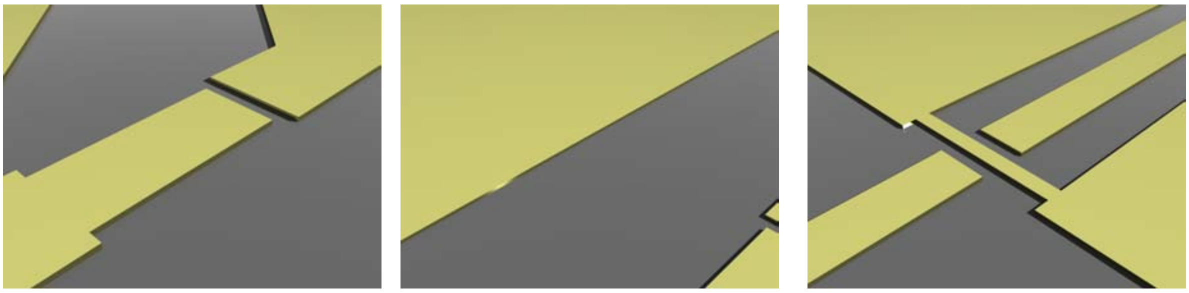

(a) RF-MEMS (b) Bias lines tunnel (c) Air-bridge

Figure 7.14: Thick metallization

RF-MEMS releasing The last step of the fabrication process is the switches releasing or what is the same, to remove the sacrificial material. This part of the process is the more delicate because the switches are very fragile. In cases where the wafer will be diced to separate different devices, the dicing process should be done before the releasing because the RF-MEMS structure remains stronger with the sacrificial layer and would not be affected by the dicing tool vibrations that could break the moving parts of the switch. Once the different antennas have been separated, the releasing process is done by wet-etching removing completely the PMMA. While the devices are in the removal liquid, there are no risks, and the possible structural damage that could cause the drying process is solved by using the critical point dryer tool. Fig. 7.15 show some pics of the antenna taken with the Scanning Electron Microscope (SEM) at CNF. In Fig. 7.15(a) it is seen the final RF-MEMS switch used for the antenna polarization reconfiguration. Fig. 7.15(b) shows the phase-shifter made with three switches and their air-bridges connecting every side of the ground plane. Fig. 7.15(c) represents the air-bridges used in the CPW. Fig. 7.15(d) shows the feed-network power-divider with the required air-bridges. In Fig. 7.15(e) it can be seen a high resistivity line crossing the ground plane through a tunnel. Finally, Fig. 7.15(f) shows the complete CPW Patch antenna at Ka-band.

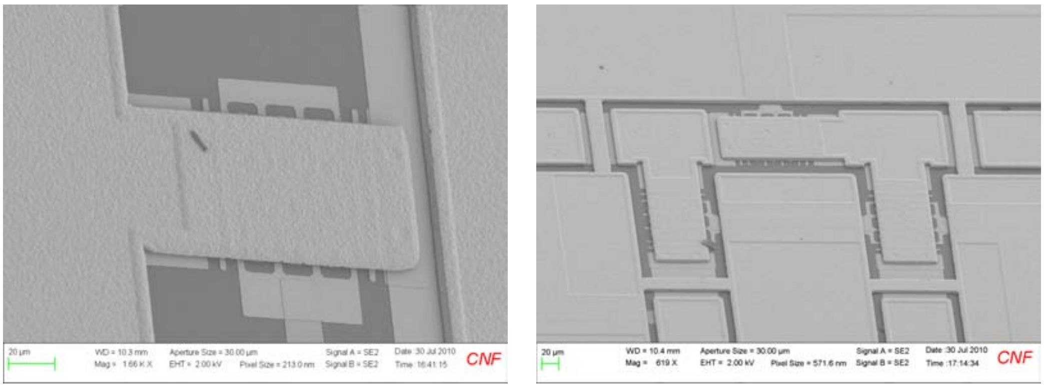

(a) RF-MEMS switch (b) Three switches phase-shifter

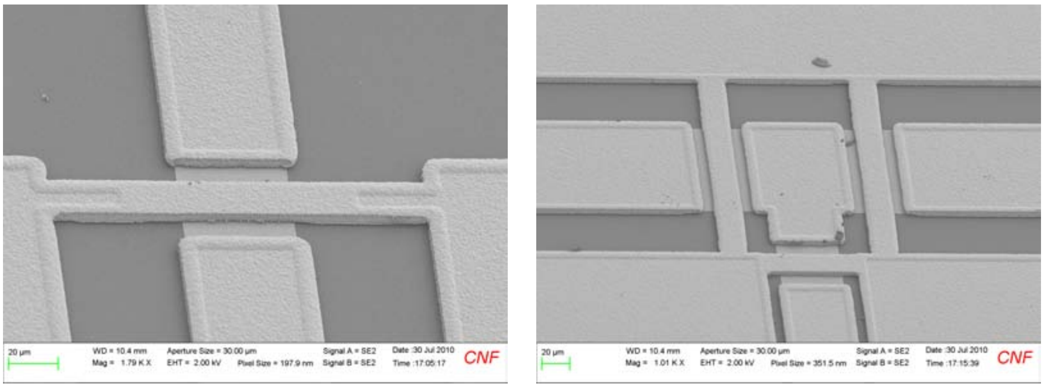

(c) CPW air-bridges (d) Feed-network power-divider

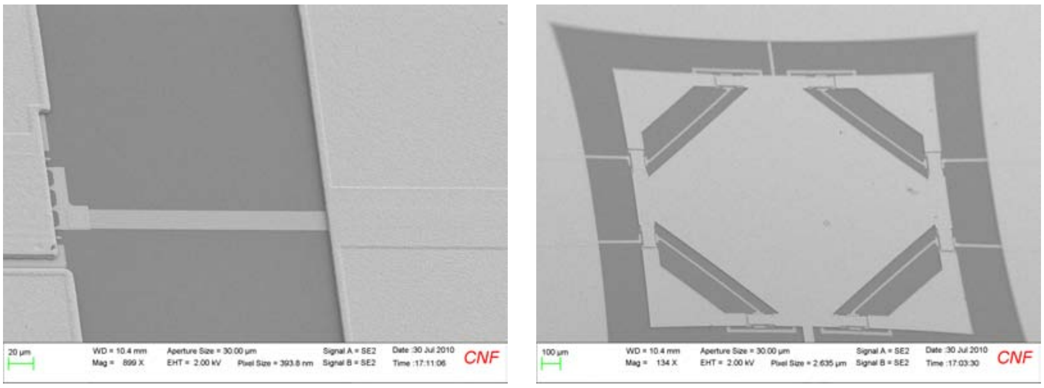

(e) High resistivity line (f) CPW Patch antenna at Ka-band

Figure 7.15: Scanning Electron Microscope (SEM) pics of the microfabricated CPW Patch

7.1.3 4-Qdime Antenna

Two different designs of the 4-Qdime antenna have been presented in this thesis, one using quartz as substrate and the other Benzocyclobuten polymer (BCB). Both designs have similar feed network, consisting of gold microstrip lines printed on BCB. The main 4-Qdime microfabrication processes are presented for the two proposed designs:

Quartz-substrate 4-Qdime The quartz-substrate 4-Qdime antenna has its more difficult fabrication step in creating the bias lines and the ground connections that pass through the glass substrate. This process requires an extra dicing tool which is not commonly found in all the microfabrication facilities. The other fabrication processes are similar to the ones used to fabricate the CPW patch antenna.

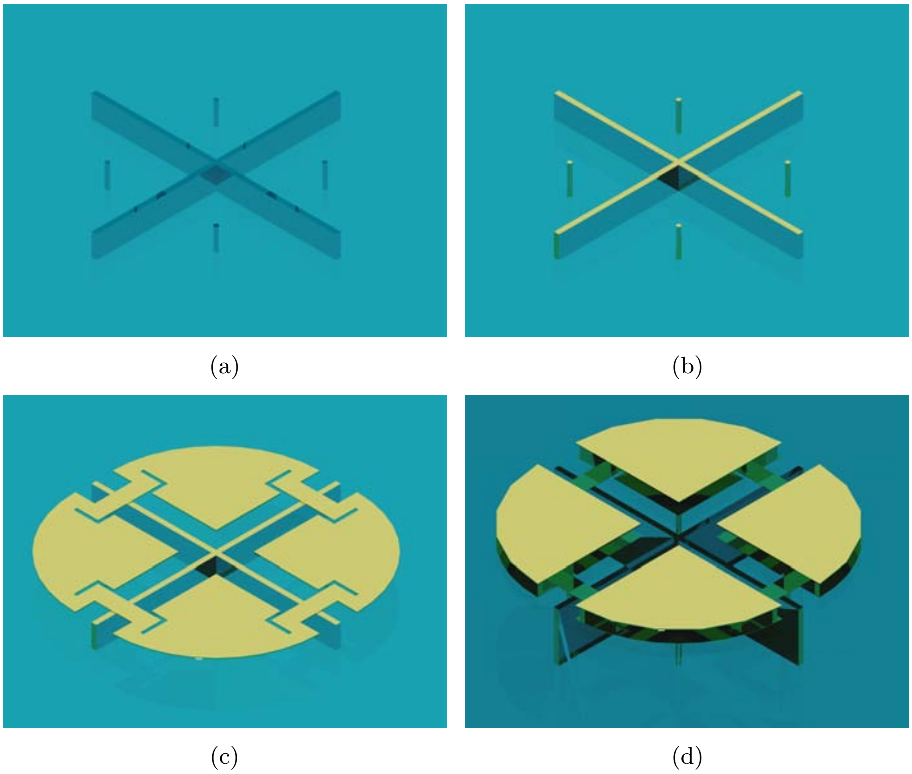
(a) (b)

(c) (d)

Figure 7.16: Quartz-substrate 4-Qdime microfabrication process

To fabricate the antenna, the two quartz substrates can be processed in parallel independently and then being stacked together at the end. The fabrication process can be summarized in the following steps:

- Quartz bias-holes and through-glass apertures realization (Fig. 7.16(a))
- Metallization of the bias-holes and ground connections (Fig. 7.16(b)).
- Gold deposition. A very thin seed layer of gold and chromium is evaporated on the top of substrate. The metal is patterned by lithography and then the seed layer is grown up to a

metallization thickness between $4-5\mu m$ by the electroplating process. Finally the undesired gold is removed by wet-etching (Fig. 7.16(c)).

- Alignment and union of the two patterned quartz substrates (Fig. 7.16(d)).

Once the radiating part of the antenna is fabricated, it has to be turned upside-down to fabricate the feed network. The difficulty to fabricate this part of the antenna relays in the RF-MEMS switches fabrication process. As an initial proof of concept design, a HW design can be microfabricated as shown in Fig. 7.17. The process consist of three steps:

- BCB deposition by spinning. A maximum of $30\mu m$ thickness can be deposited. Because its organic nature, after the deposition it is required to bake the substrate in order to extract the solvent from the material.
- Gold deposition, consisting of evaporate a very thin seed layer and grow it up by electroplating. After a lithography process, the undesired gold is removed by wet-etching.
- Because the absence of Radio-Frequency Microelectromechanical Systems, the final process of this antenna consist only into dicing the different devices.

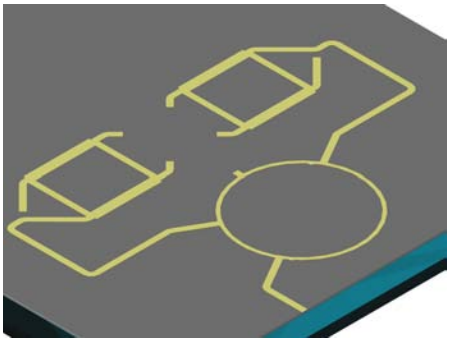

Figure 7.17: 4-Qdime dielectric feed network

BCB-substrate 4-Qdime The BCB-substrate 4-Qdime microfabrication process difficulty relays into obtaining a uniformly distributed BCB layers. Fig. 7.18 shows the measured uniformity of $1\mu m$ thick organic material deposition on Silica (Si) using spinning, where a 1.5% uniformity can be observed.

This antenna fabrication process uses the quartz top layer as the fabrication base layer, being built from top to bottom. The fabrication process can be summarized as:

- On the quartz substrate, gold is deposited by evaporation and grown up by electroplating; the antenna is patterned by lithography; and the undesired gold is removed by wet-etching.
- BCB $30\mu m$ deposition by spinning in two steps. The existence of irregularities due to the patterned gold may affect the deposition uniformity.

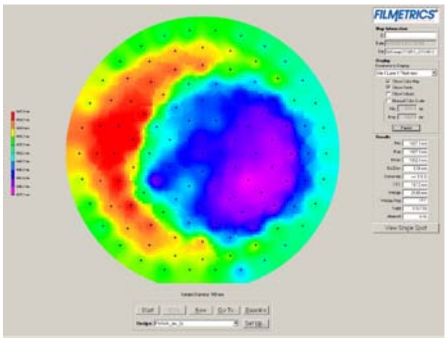

Figure 7.18: Organic material deposition on Silica uniformity

- Gold deposition and antenna low layer pattern on the BCB substrate
- BCB $30 \mu m$ deposition by spinning.
- Ground plane gold deposition and patterned.
- Feed network BCB $30 \mu m$ deposition by spinning in two steps.
- Gold deposition and microstrip lines pattern.

7.2 Measurement results

The different microfabricated RF-MEMS switches and antennas have been tested and measured in DC and RF.

7.2.1 Radio-Frequency Microelectromechanical Systems (RF-MEMS) switches

The first microfabricated device measured has been the RF-MEMS switch. Two different switches have been manufactured with different cantilever width: $30\mu m$ and $60\mu m$. To characterize the isolation level when turned off, different switches have been measured in the GSG-probe station up to 50 GHz, and compared to the finite elements method Ansoft HFSS simulator results. In Fig. 7.19 can be seen how the narrower cantilever switch has a higher isolation due to the reduced capacitance area between the cantilever and the contact pad. The RF-MEMS switch with $30\mu m$ cantilever width has an isolation of 14dB at 30GHz and an estimated isolation of 7dB at 60 GHz. The switch with $60\mu m$ cantilever width has an isolation of 8dB at 30 GHz and an estimated isolation of 2dB at 60GHz. The switch with the wider cantilever is the one that has been used in this thesis designs at Ka-band. The measured isolation is higher than the simulated, which invites to think into a good behavior when integrated to the antennas.

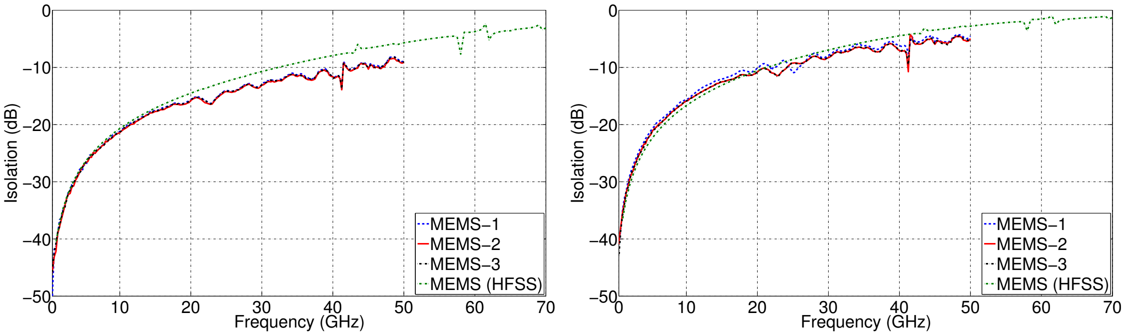

(a) $30\mu m$ cantilever length

(b) $60\mu m$ cantilever length

Figure 7.19: RF-MEMS Isolation

The fabricated RF-MEMS have an activation voltage between 40-65V, tested in DC. This voltage margin is due to the electroplating non-uniformity which differs the cantilever width. The RF-MEMS switch has also been tested in time domain to see its mechanical behavior. Fig. 7.20 shows the switch response when applying an RF signal it is being activated. The activation time is around $75\mu s$, which is quite slow for such type of switches.

7.2.2 HW CPW Patch Antenna

The microfabricated single-element HW CPW Patch antennas have been measured. The results for the Ka- and V-band prototypes are:

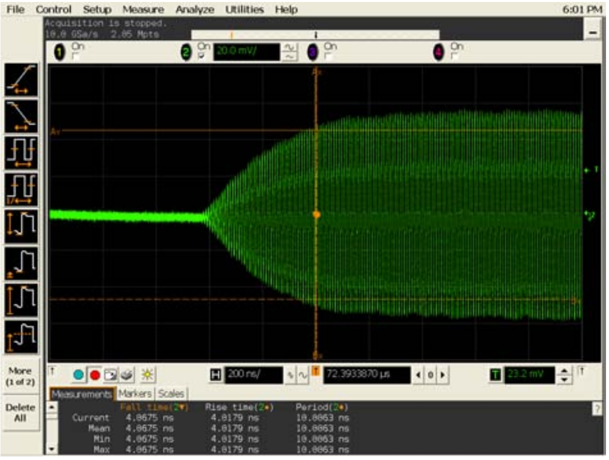

```
Acquisition is stopped.
10.0 GSa/s  2.05 Mpts
```

```
         Fall time(2▼)  Rise time(2•)  Period(2•)
Current  4.0675 ns      4.0179 ns      10.0063 ns
   Mean  4.0675 ns      4.0179 ns      10.0063 ns
    Min  4.0675 ns      4.0179 ns      10.0063 ns
    Max  4.0675 ns      4.0179 ns      10.0063 ns
```

Figure 7.20: RF-MEMS switch time domain response

Ka-band Prototype The high path attenuation together with amplitude and phase errors make very difficult to measure parameters such as Axial Ratio (AR) at MMW frequencies in the UPC anechoic chamber where the distance between the Antenna Under Test (AUT) and the probe antenna is higher than $800\lambda_0$. This situation has lead to measure the fabricated single-element Ka-band antennas in the Millimeter-wave (MMW) circuit set-up presented in Fig. 7.21(a), which only allows the radiation measurement in the main beam direction. The distance between the antenna and the probe has been reduced to $50\lambda_0$, which is still in far field. In order to be able to connect the antenna with the Network Analyzer through a 50GHz coaxial connector from Southwest Microwave Inc [65], a frame-holder have been built as shown in Fig. 7.21(b). The antenna is connected to the frame by air-bonding, which reduces the measured impedance matching.

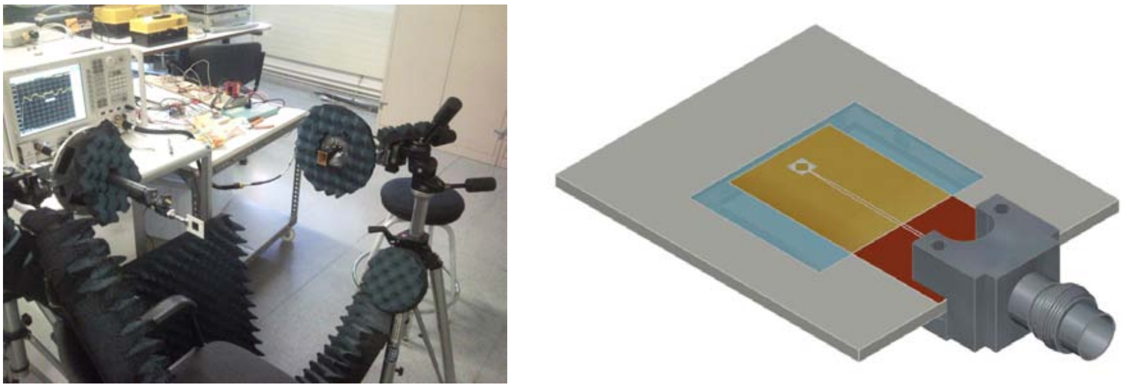
(a) Measurement Set-up (b) Antenna Frame-Holder

Figure 7.21: Ka-band measurements set-up

Using this measurement set-up, it has been possible to obtain the antenna reflection coefficient and the axial ratio. The antenna measured frequency bandwidth related to -6dB is 11% when configured in LP and 8% when configured in CP (Fig. 7.22(a)). Concerning the axial ratio (Fig. 7.22(b)), a frequency bandwidth related to 3dB axial ratio of 3% is measured.

The HW antenna array with a 90° phase-shifter activated has been measured in the UPC

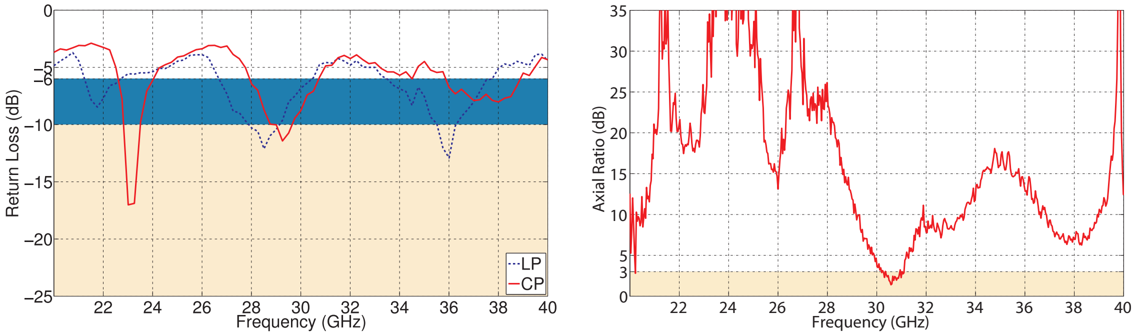

(a) S-parameters (b) Axial Ratio

Figure 7.22: HW CPW Patch Ka-band measurements

anechoic chamber as illustrated in Fig. 7.23.

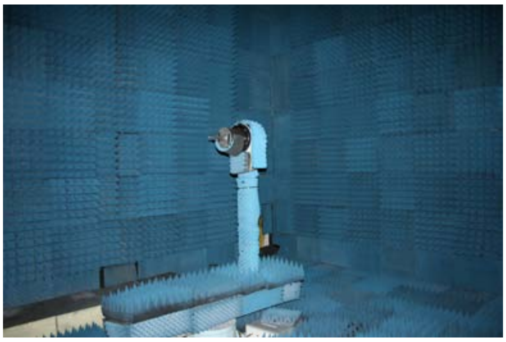

Figure 7.23: Anechoic chamber measurements set-up

Fig.7.24(a) illustrates the measured reflection coefficient. The antenna with the frame-holder presents a low matching with a -6dB return loss frequency bandwidth of 3%. Fig.7.24(b) presents the measured and simulated radiation patterns. It can be seen a good concordance between the simulated and measured diagrams, pointing both to $\theta = 15^{\circ}$. Some discordance it is observed for $\theta = 90^{\circ}$ where the measurement should present a null. This error may come from the connector or reflections with the chamber rotors. It is also observed that the ratio between the two main lobes is higher than 1dB, which can be caused by differences between the simulated and real dielectric permittivity or the substrate thickness. Besides these differences, can be said that the measurement agrees with the expected radiation pattern.

V-band Prototype The V-band HW CPW Patch antennas prototypes have been measured using the GSG-probe station as presented in Fig. 7.25.

The measured return loss for each configuration is presented in Fig. 7.26(a). It can be seen how the frequency bandwidth relative to -10 dB return loss is around 15% with the LP configuration and wider with the other configurations. To measure the axial ratio of the antennas configured in circular polarization, an scattering technique has been used [66]. This technique consists on placing a $\lambda/2$ dipole in two orthogonal positions at a far field distance ($> 2\lambda$). The two measured scattered

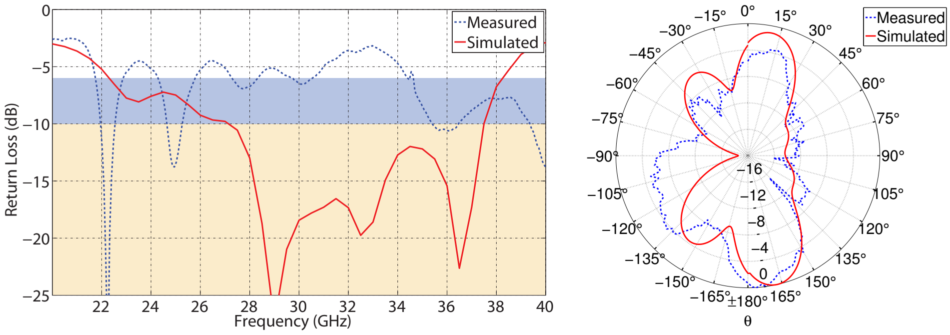

(a) Return Loss (b) Radiation Pattern at 30GHz

Figure 7.24: HW array measurements

(a) GSG Probe (b) Microscope Image

Figure 7.25: V-band measurements set-up

fields give the necessary amplitude and phase information required to compute the antenna axial ratio [34]. To reduce and extract the high number of reflections in the measurement set-up, absorber materials and temporal gating have been used. The resulting axial ratio for the circular polarization configurations is shown in Fig. 7.26(b), where it can be seen a 3dB axial ratio frequency bandwidth of 13%.

7.2.3 Summary and Conclusions

This chapter has presented the CPW patch antennas microfabrication process followed to fabricate the antenna in Hard-Wire (HW) configuration and with the integrated RF-MEMS switches, being the first one a particular case of the second one. The fabrication process initial step lies into the design and fabrication of the different lithography masks in L-Edit. Then, the fabrication process has moved into the clean-room facility at CNF where the different material depositions and patterns have been done. Finally, the different devices were diced from the wafer and the RF-MEMS released. This chapter also summarizes the main steps required to fabricate the 4-Qdime antenna designs, using quartz and BCB dielectric substrates.

The manufactured RF-MEMS switches and the CPW Patch antennas have been measured.

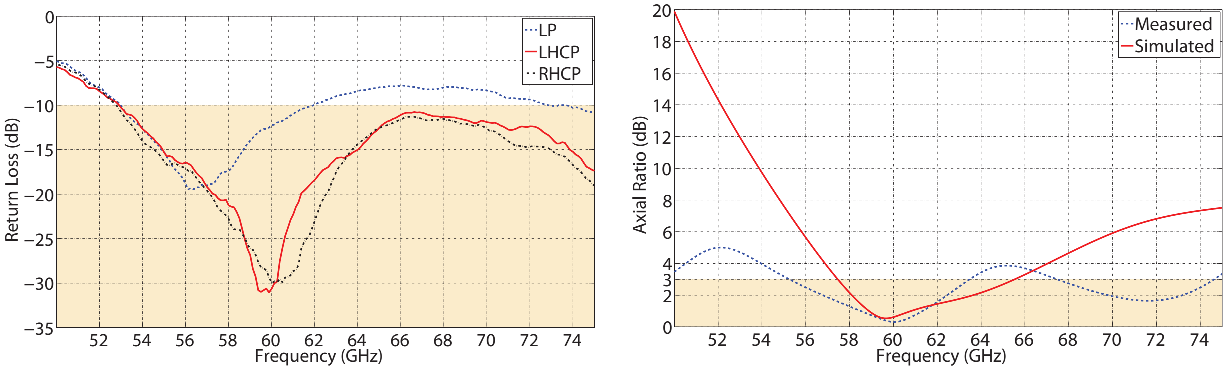

(a) S-parameters (b) Axial Ratio

Figure 7.26: HW CPW Patch V-band measurements

The fabricated switch presents a good isolation till frequencies up to 60GHz as expected. The switch activation voltage is between 40-65V, and the activation time is of the order of hundreds microseconds. Concerning CPW Patch antennas, the HW configurations have been measured at Ka- and V-band. The measurement set-up used has changed for each band. At Ka-band the antenna has been fed with a coaxial connector and the antenna has been measured in the anechoic chamber to measure the radiation pattern and in a short distance MMW circuit set-up to measure the axial ratio and return loss. Good agreement between simulation and measurements are observed except for the return loss due to the use of a frame holder where the air-bonding connections influence negatively to the antenna input impedance. The HW CPW Patch antenna at V-band has been measured using the GSG-probe station. The measured return loss and axial ratio agreed with the simulations.

Chapter 8

Conclusions

Emerging applications ranging from Wireless Personal Area Network (WPAN) to Automotive Radar passing through Satellite Communication Systems (SCS) are moving to Millimeter-wave (MMW) bands, where wide frequency bandwidths are available. Planar antennas are good candidates to be used in these applications given their reduced dimensions, light weight, low-cost and high integration level. All these applications in the range of 30 to 100GHz have in common the need for small dimensions(mm), low losses and low permittivity materials ($tan\delta \approx 0.0007$ and ε_r between 2 and 4), and high fabrication tolerances (μm).

Considerations to be taken into account when designing new MMW planar antennas are the dielectric material and transmission line geometry. Concerning the dielectric materials, while very well known substrates such as Polytetrafluoroethylene or Teflon (PTFE) and quartz, meet the low loss requirements, new materials as Benzocyclobuten polymer (BCB) or Low Temperature Co-fired Ceramic (LTCC) may be advantageous when looking for integrated designs. Quartz and PTFE are not capable to be deposited and have to be used with their commercial thicknesses. Also, quartz presents a high hardness which makes it difficult to mold and drill. On the other hand, BCB and LTCC can be easily deposited and patterned in clean-room facilities, but are subject to maximum thickness limitations. In MMW frequencies, the losses in the feed network are a critical point. The attenuation of different printed transmission lines (microstrip, stripline and CPW) does not differ much when the frequencies are low, but when moving to higher frequencies, CoPlanar Waveguide (CPW) reduces the feed network losses. A disadvantage of using CPW lays in the possibility to excite the odd-mode and affect the radiated fields. The undesired modes should be canceled with the use of air-bridges, being recommended to be placed in discontinuities such as power dividers or impedance transformers.

At MMW frequencies, antenna reconfigurability, both in polarization and beam pointing direction, is a possibility being more and more a need. Concerning the polarization reconfigurability, there are two options. One is the single reconfigurable element for which CPW Patch is a good candidate for its simplicity with a frequency bandwidth in the order of 5% limited by the axial ratio when configured in CP. The second is the composed architectures as the 4-Qdime antenna, more complex in shape but with a frequency bandwidth up to 25%. Both antenna types are compatible with microfabrication processes and RF-MEMS switches integration at Ka- (26.5 to 40GHz), V- (50 to 75GHz) and W-band (75 to 110GHz).

When fabricating antenna arrays, each element amplitude and phase error affects the antenna performance in terms of gain, beam pointing, HPBW and sidelobe level. Arrays with a low number of elements are more sensitive to amplitude and phase random errors while in large arrays the single element errors are compensated easily by the other elements. Axial Ratio (AR) and therefore the circular polarization is very sensitive to the amplitude and phase errors of the two orthogonal components of the radiated field. To have a circularly polarized radiated field, acceptable amplitude standard deviations are in the order of 0.7dB and phase standard deviation of 7^{o}.

MMW antennas dimensions and fabrication tolerances require the use of microfabrication techniques. The microfabrication of multilayer structures becomes easier when the frequency increases, because the current technology does not allow to deposit dielectric materials with the appropriate electromagnetic properties and required thicknesses for antennas operating at the low band of the MMW band. At the same time that frequency increases, integrated metal-contact RF-MEMS switches lose performance due to their poor isolation ($<$ 6dB). The use of capacitive switches is an alternative when frequencies are higher than 50GHz.

While the RF-MEMS switch microfabrication process comprises more than 170 different steps, becoming highly complex, the resulting yield is low, in the order of 30%. The nonuniformity of the metal thickness obtained with the electroplating process is considered to be one of the main reasons of this low yield. The difficulty to obtain a fabrication process with a yield near 100% leads to antenna designs with switch redundancy. The design of MMW antennas requires a good expertise in the microfabrication processes and the resulting tolerances. The designing and fabrication processes are merged in the mask generation, where align marks, lithography monitoring marks, thickness monitor and structural tests are strategically drawn.

In order to validate the properties of the MMW integrated antennas, when measuring the antenna independently, it can be fed by a coaxial connector, GSG probes or waveguide. Waveguide feed requires the design of transitions, adding more complexity to the antenna design. The use of coaxial connectors is limited by its upper operational frequency, having a good performance up to 60GHz. They are also characterized to be electrically big, interfering the antenna radiation when close to the antenna. GSG probes cover the MMW frequency band, with the only limitation to be connected to a CPW and the dimensions constrain given by the probes separation.

The measurement of MMW antennas in a common anechoic chamber presents difficulties due to the high path losses. Alternative measurement set-ups are placing the antennas closer, in the order of $50\lambda_0$, or using scattering techniques without test probe to measure parameters as axial ratio.

Looking at the future of integrated antennas design at Millimeter-wave (MMW) frequencies, three different research lines may be deepened.

A wide band design for a single element polarization reconfigurable antenna should be pursuit using multi layer techniques with a new Benzocyclobuten polymer (BCB) or Low Temperature Co-fired Ceramic (LTCC) materials. Integrated capacitive RF-MEMS switches operating at higher frequencies should also be designed using these materials.

A second research line would be related with the array design and the microfabrication process making the antenna design and circuit layer spatially compatible to avoid grating lobes, achieving full polarization and beam pointing reconfigurability capability.

Finally, a comprehensive effort has to be done to develop an integrated compatible microwave input impedance and radiation pattern measurement system, able to deal with a different connection technologies (waveguide, coaxial and CPW) and capable to measure amplitude and phase field polarization. The positioning system should have a movement mechanism compatible with RF-MEMS biasing cables.

Bibliography

[1] R. Kraemer and M. Katz, *Short-Range Wireless Communications: Emerging Technologies and Applications.* Wiley Publishing, 2009.

[2] K.-L. Wong, *Planar antennas for wireless communications.* New York, NY, USA: Wiley-Interscience, 2003.

[3] Y. Antar, "Integrated antennas for wireless applications," in *Radio Science Conference, 2000. 17th NRSC '2000. Seventeenth National*, 2000.

[4] P. Hall, J. Dahele, and J. James, "Design principles of sequentially fed, wide bandwidth, circularly polarised microstrip antennas," *Microwaves, Antennas and Propagation, IEE Proceedings H*, vol. 136, no. 5, pp. 381 – 389, Oct. 1989.

[5] A. Sabban, "Applications of mm wave microstrip antenna arrays," in *Signals, Systems and Electronics, 2007. ISSSE '07. International Symposium on*, july 2007, pp. 119 –122.

[6] ——, "A comprehensive study of losses in mm-wave microstrip antenna arrays," in *Microwave Conference, 1997. 27th European*, vol. 1, 8-12 1997, pp. 163 –167.

[7] G. Huff and J. Bernard, *Modern Antenna Handbook.* New York, NY, USA: Wiley-Interscience, 2008, ch. Reconfigurable Antennas.

[8] Z. Jiajie, W. Anguo, and W. Peng, "A survey on reconfigurable antennas," in *Microwave and Millimeter Wave Technology, 2008. ICMMT 2008. International Conference on*, vol. 3, 21-24 2008, pp. 1156 –1159.

[9] S. Yang, C. Zhang, H. Pan, A. Fathy, and V. Nair, "Frequency-reconfigurable antennas for multiradio wireless platforms," *Microwave Magazine, IEEE*, vol. 10, no. 1, pp. 66 –83, february 2009.

[10] C. Christodoulou, D. Anagnostou, and L. Feldner, "Re-configurable antennas," in *Anti-counterfeiting, Security, Identification, 2007 IEEE International Workshop on*, 16-18 2007, pp. 9 –12.

[11] J. T. Bernhard, *Reconfigurable Antennas*, ser. Synthesis Lectures on Antennas. Morgan & Claypool Publishers, 2007.

[12] E. Erdil, K. Topalli, M. Unlu, O. Civi, and T. Akin, "Frequency tunable microstrip patch antenna using rf mems technology," *Antennas and Propagation, IEEE Transactions on*, vol. 55, no. 4, pp. 1193 –1196, 2007.

[13] J.-C. Langer, J. Zou, C. Liu, and J. Bernhard, "Micromachined reconfigurable out-of-plane microstrip patch antenna using plastic deformation magnetic actuation," *Microwave and Wireless Components Letters, IEEE*, vol. 13, no. 3, pp. 120 – 122, Mar. 2003.

[14] J. Bernhard, E. Kiely, and G. Washington, “A smart mechanically actuated two-layer electromagnetically coupled microstrip antenna with variable frequency, bandwidth, and antenna gain,” *Antennas and Propagation, IEEE Transactions on*, vol. 49, no. 4, pp. 597 –601, Apr. 2001.

[15] D. Rodrigo, Y. Damgaci, M. Unlu, L. Jofre, and B. Cetiner, “Small pixelled antenna with mems-reconfigurable radiation pattern,” in *Antennas and Propagation Society International Symposium (APSURSI), 2010 IEEE*, 2010, pp. 1 –4.

[16] G. M. Rebeiz, *RF MEMS: Theory, Design, and Technology.* New York, NY, USA: John Wiley & Sons, Inc., 2003.

[17] N. Biyikli, Y. Damgaci, and B. Cetiner, “Low-voltage small-size double-arm mems actuator,” *Electronics Letters*, vol. 45, no. 7, pp. 354 –356, march 2009.

[18] Y. Rahmat-Samii and E. Michielssen, Eds., *Electromagnetic Optimization by Genetic Algorithms.* New York, NY, USA: John Wiley & Sons, Inc., 1999.

[19] J. Encinar, M. Piqueras, and J. e. a. Martí, “Beam-forming methods: Deliverable d5 - final report,” 2005.

[20] R. Baggen, S. Vaccaro, and D. del Rio, “Design considerations for compact mobile ku-band satellite terminals,” in *Antennas and Propagation, 2007. EuCAP 2007. The Second European Conference on*, 2007, pp. 1 –5.

[21] O. Feder, G. Rabinovitch, and S. Zach, “Ka-band satellite systems: current state of development,” in *Electrical and Electronic Engineers in Israel, 2000. The 21st IEEE Convention of the*, 2000, pp. 171 –174.

[22] S. Holzwarth, O. Litschke, W. Simon, K. Kuhlmann, and A. Jacob, “Far field pattern analysis and measurement of a digital beam forming 8x8 antenna array transmitting from 29.5 to 30 ghz,” in *Antennas and Propagation, 2007. EuCAP 2007. The Second European Conference on*, 11-16 2007, pp. 1 –5.

[23] “Radiation diagrams for use as design objectives for antennas of earth stations operating with geostationary satellites,” in *ITU-R Recommendation S.580-6*, Geneva, Switzerland, 2004.

[24] R. Daniels and R. Heath, “60 ghz wireless communications: emerging requirements and design recommendations,” *Vehicular Technology Magazine, IEEE*, vol. 2, no. 3, pp. 41 –50, sept. 2007.

[25] S. Franson and R. Ziolkowski, “Gigabit per second data transfer at 60ghz in high gain grid antennas,” in *Antennas and Propagation Society International Symposium, 2008. AP-S 2008. IEEE*, 2008, pp. 1 –4.

[26] “Ieee standard for information technology - telecommunications and information exchange between systems - local and metropolitan area networks - specific requirements. part 15.3: Wireless medium access control (mac) and physical layer (phy) specifications for high rate wireless personal area networks (wpans) amendment 2: Millimeter-wave-based alternative physical layer extension,” *IEEE Std 802.15.3c-2009 (Amendment to IEEE Std 802.15.3-2003)*, pp. c1 –187, oct. 2009.

[27] R. Fisher, “60 ghz wpan standardization within ieee 802.15.3c,” jul. 2007, pp. 103 –105.

[28] S. Ranvier, S. Dudorov, M. Kyro, C. Luxey, C. Icheln, R. Staraj, and P. Vainikainen, “Low-cost planar omnidirectional antenna for mm-wave applications,” *Antennas and Wireless Propagation Letters, IEEE*, vol. 7, pp. 521 –523, 2008.

[29] S. Seok, N. Rolland, and P.-A. Rolland, “A 60 ghz quarter-wave patch antenna based on bcb polymer,” in *Antennas and Propagation Society International Symposium, 2008. AP-S 2008. IEEE*, 5-11 2008, pp. 1 –4.

[30] A. Boe, M. Fryziel, N. Deparis, C. Loyez, N. Rolland, and P. Rolland, “Smart antenna based on rf mems switches and printed yagi-uda antennas for 60 ghz ad hoc wpan,” in *Microwave Conference, 2006. 36th European*, 10-15 2006, pp. 310 –313.

[31] F. Ohnimus, I. Ndip, S. Guttowski, and H. Reichl, “An efficient and broadband slot antenna for 60 ghz wireless applications,” in *Advanced Packaging and Systems Symposium, 2008. EDAPS 2008. Electrical Design of*, 10-12 2008, pp. 69 –72.

[32] A. Cardama, L. Jofre, J. Rius, J. Romeu, S. Blanch, and M. Ferrando, *Antenas.* Edicions UPC, 1998.

[33] F. Schwering, “Millimeter wave antennas,” *Proceedings of the IEEE*, vol. 80, no. 1, pp. 92 –102, jan 1992.

[34] C. A. Balanis, *Antenna Theory: Analysis and Design.* Wiley-Interscience, 2005.

[35] N. Alexopoulos, P. Katehi, and D. Rutledge, “Substrate optimization for integrated circuit antennas,” *Microwave Theory and Techniques, IEEE Transactions on*, vol. 31, no. 7, pp. 550 –557, jul. 1983.

[36] S. Costanzo, I. Venneri, G. Di Massa, and A. Borgia, “New technologies and antenna design concepts at millimeter-wave bands,” in *Antennas and Propagation, 2009. EuCAP 2009. 3rd European Conference on*, 2009.

[37] ——, “Benzocyclobutene as substrate material for planar millimeter-wave structures: Dielectric characterization and application,” *Journal of Infrared, Millimeter and Terahertz Waves*, vol. 31, pp. 66–77, 2010.

[38] M. Sun, Y. Guo, M. Karim, and L. Ong, “Linearly polarized and circularly polarized arrays in ltcc technology for 60ghz radios,” in *Antennas and Propagation Society International Symposium (APSURSI), 2010 IEEE*, 2010, pp. 1 –4.

[39] J. Gao, K. Li, and H. Harada, “Wideband stacked microstrip patch antenna on thin ptfe substrate for millimeter-wave personal area network (mmwpan),” in *Antennas and Propagation Society International Symposium (APSURSI), 2010 IEEE*, 2010, pp. 1 –4.

[40] I. Venneri, A. Borgia, L. Boccia, G. Amendola, and G. Di Massa, “Millimeter waves patch antenna design and realization on bcb polymer substrates,” in *Antennas and Propagation Society International Symposium, 2008. AP-S 2008. IEEE*, 2008, pp. 1 –4.

[41] (2011) Cyclotene advanced eletronics resins. [Online]. Available: http://www.dow.com/cyclotene/

[42] (2011) What is ltcc?: Design rules. [Online]. Available: http://www.ltcc.de

[43] (2011) Rogers corporation. [Online]. Available: http://www.rogerscorp.com/

[44] *Synthetic Quartz Glass Substrates*, Shin-Etsu Chemical Co., 6-1 Ohtemachi 2-chome, Chiyoda-ku, Tokyo, Japan. [Online]. Available: www.shinetsu.co.jp/e/product/pdf/garasu.pdf

[45] R. Barrett, “Microwave printed circuits–the early years,” *Microwave Theory and Techniques, IEEE Transactions on*, vol. 32, no. 9, pp. 983 – 990, sep. 1984.

[46] D. M. Pozar, *Microwave Engineering.* John Wiley & Sons, Inc, 1990.

[47] R. Pucel, D. Masse, and C. Hartwig, "Losses in microstrip," *Microwave Theory and Techniques, IEEE Transactions on*, vol. 16, no. 6, pp. 342 – 350, jun 1968.

[48] C. R. Gupta K.C., Garg R., *Computer Aided design of Microwave Circuits.* Artech House, 1981.

[49] R. N. Simons, *Coplanar Waveguide Circuits, Components, and Systems.* John Wiley & Sons, Inc, 2001.

[50] R.Garg, P. Bhartia, I. Bahl, and A. Ittipiboon, *Microstrip Antenna Design Handbook.* Boston, USA: Artech House Inc., 2001.

[51] K. Li, C. Cheng, T. Matsui, and M. Izutsu, "Simulation and experimental study on coplanar patch and array antennas," in *Microwave Conference, 2000 Asia-Pacific*, 2000, p. 1411.

[52] R. Garg and K. Gupta, "Expressions for wavelength and impedance of a slotline (letters)," *Microwave Theory and Techniques, IEEE Transactions on*, vol. 24, no. 8, pp. 532 – 532, aug. 1976.

[53] E. C. Jordan and K. G. Balmain, *Ondas Electromagneticas y Sistemas Radiantes*, Paraninfo, Ed., 1978.

[54] Y. Sung, T. Jang, and Y.-S. Kim, "A reconfigurable microstrip antenna for switchable polarization," *Microwave and Wireless Components Letters, IEEE*, vol. 14, no. 11, pp. 534 – 536, nov. 2004.

[55] L. Jofre, B. Cetiner, and F. De Flaviis, "Miniature multi-element antenna for wireless communications," *Antennas and Propagation, IEEE Transactions on*, vol. 50, no. 5, pp. 658 –669, May 2002.

[56] J. Huang, "A technique for an array to generate circular polarization with linearly polarized elements," *Antennas and Propagation, IEEE Transactions on*, vol. 34, no. 9, pp. 1113 – 1124, Sept. 1986.

[57] G. Tsoulos and C. C. G., *Modern Antenna Handbook.* New York, NY, USA: Wiley-Interscience, 2008, ch. Arrays and Smart Antennas.

[58] R. E. Collin and F. J. Zucker, *Antenna Theory.* McGraw-Hill, 1969, ch. Nonuniform Arrays.

[59] R. C. Hansen, *Phased Array Antennas.* New York, NY: John Wiley and Sons, Inc., 1998.

[60] R. J. Mailloux, *Phased Array Antenna Handbook.* Artech House Publishers, 2005, second ed.

[61] B. D. Steinberg, *Principles of aperture and array system design : including random and adaptive arrays / Bernard D. Steinberg.* Wiley, New York :, 1976.

[62] S. Franssila, *Introduction To Microfabrication.* John Wiley & Sons, November 2010.

[63] S. D. Senturia, *Microsystem Design.* Kluwer Academic Publishers, 2001.

[64] N. D. Masters and D. Koester, *Side-by-side comparison of passive MEMS strain test structures under residual compression.* West Conshohocken, 2001, ch. Mechanical properties of structural thin films, pp. 168–200.

[65] (2011) Southwest microwave inc. [Online]. Available: http://mpd.southwestmicrowave.com/

[66] S. Capdevila, L. Jofre, J.-C. Bolomey, and J. Romeu, "Rfid multiprobe impedance-based sensors," *Instrumentation and Measurement, IEEE Transactions on*, vol. PP, no. 99, pp. 1 –9, 2010.

Publications

- J. Balcells, D. Rodrigo, P. J. Ferrer, J. Romeu, S. Blanch, L. Jofre, "Antenes Satèl.lit Planars per a Aplicacions VSAT". Study realized for INDRA
- J. Balcells, Y. Damgaci, B. A. Cetiner, J. Romeu, L. Jofre, "60GHz MEMS-Integrated Polarization Reconfigurable CPW Antenna", MEMSWAVE 2009, July 2009.
- J. Balcells, Y. Damgaci, B. A. Cetiner, J. Romeu, L. Jofre "Polarization Reconfigurable MEMS-CPW Antenna for mm-wave Applications", European Conference on Antennas and Propagation. Barcelona, April, 2010